学位論文

Topics in the Generalized-Ensemble Algorithms: Applications to Biological Systems and Spin Systems

（拡張アンサンブル法の研究：生体系とスピン系への応用）

名古屋大学
大学院理学研究科
物質理学専攻 (物理系)
理論生物化学物理 (TB) 研究室

永井哲郎

Department of Physics
Gradate School of Science
Nagoya University

Tetsuro NAGAI

February 28, 2013

Acknowledgments

My most heartfelt thanks go to my thesis advisor, Professor Yuko Okamoto, for his patient guidance and constant long-term encouragement. I appreciate Professor Wolfhard Janke for his fruitful comments and hospitality during my stay at Leipzig University. I thank Drs. Desmond Johnston of Heriot-Watt University and Thomas Neuhaus of Forschungszentrum at Jülich for useful discussions. My heart is also filled with gratitude to Associate Professor Takahisa Yamato and Assistant Professor Akihiro Kimura for their discussions at the TB laboratory. I am also grateful to Associate Professor Tetsuro Konishi, who is responsible for supervision of network systems, including the e-mail server. I would like to show my gratitude to all the members of TB laboratory, including alumni, for stimulating discussions. I have learned much about MD from a lecture note by Dr. H. Okumura, who is currently an Associate Professor at the Institute for Molecular Science. Dr. Y. Sakae has given me a lot of advise including computational techniques. Dr. T. Mori was so helpful when I was senior and did not know how to carry out a research. Dr. Y. Mori's presentations were always interesting. I recognize Ms. A. Kuzumaki's useful discussions. I also obtained advice from Dr. D. Sindhikara. I wish to thank all faculty and staff members of Nagoya University. The traveling and living cost at Leipzig from May 2012 to August 2012 was supported by "Nagoya University Program for Leading Graduate Schools: Integrative Graduate Education and Research Program in Green Natural Sciences." Without it, I could not have visited Professor Janke's place and spent such exiting days in the new environment. Some of the computations were performed on the supercomputers at the Information Technology Center, Nagoya University, at

the Research Center for Computational Science, Institute for Molecular Science, and at the Supercomputer Center, Institute for Solid State Physics, University of Tokyo.

Contents

Chapter 1

General Introduction

Canonical fixed-temperature simulations of complex systems such as biomolecules and spin systems are greatly hampered by the multi-minima problem. Because simulations at low temperatures tend to get trapped in a few of a huge number of local-minimum-energy states which are separated by high-energy barriers, it is very difficult to obtain accurate canonical distribution at low temperatures by conventional Monte Carlo (MC) and molecular dynamics (MD) simulations. One way to overcome this multiple-minima problem is to perform a simulation in a *generalized ensemble* where each state is weighted by an artificial, non-Boltzmann probability weight factor so that a random walk in potential energy space may be realized. This random walk allows the simulation to overcome any energy barrier and to sample a much wider configurational space than by conventional methods.

Three of well-known generalized-ensemble algorithms are multicanonical algorithm (MUCA) [1, 2], simulated tempering (ST) [3, 4], and replica-exchange method (REM) [5, 6]. In MUCA, ST, and REM, random walk in potential energy (MUCA) and temperature (ST and REM) are realized. The molecular dynamics version of REM is called replica-exchange molecular dynamics (REMD) [7].

The cell is the most elementary unit of life. It was found by Hooke by observing the tissue of wood in the seventeenth century. The frontier of cells, where the cells communicate with other cells and outside environment, mainly consist of lipid bilayer.

The finding that the membrane consists of a fluid lipid bilayer system must be one of the most impressive advances in cell membranes, or even bio-science. It is known as the fluid mosaic membrane model, proposed by S. J. Singer and G. L. Nicolson in 1972 [8]. Proteins "swim" in the cell membrane which is made up of fluid sol-state lipid bilayers. This is commonly recognized as a base of the membrane model, while some exceptional situations are also suggested such as raft [9], which is believed to be a gel-like domain.

The Ueoka Group at Sojo University reported anti-tumor effects of hybrid liposomes [10, 11, 12, 13]. Liposomes are spherical lipid bilayers, which can be made artificially. The hybrid liposomes here correspond to the liposomes that consist of not only phosphate lipids but also polyethylene glycol (PEG). These substances have been studied as a candidate of drug delivery systems. What the Group found is that even without anti-tumor drug inside, the liposomes made of dimyristoylphosphatidylcholine (DMPC) themselves can work as anti-tumor drugs. What is more surprising is that the effect changes drastically even when the ingredient of liposomes is changed slightly. Dipalmitoylphosphatidylcholine (DPPC), DMPC, and dilauroylphosphocholine (DLPC) are the phosphate lipids similar to each other. They have the same head group, namely phosphatidylcholine (PC). The only difference is in the fat tails. DPPC, DMPC, and DLPC have 16, 14, and 12 carbons in each of the two tails, respectively. DPPC and DPMC exist in the human body. According to their experimental results, hybrid liposomes consisting of DPPC have no effect on neither ordinary cells nor cancer cells. It has nothing to do with drug effects. Those of DMPC cause cancer cells to perform apoptosis specifically. However, ordinary cells are not affected. Thus, the lipisomes with this lipid react as anti-tumor drugs. DLPC liposomes cause necrosis and thus are toxic.

This is of great interest. Although the difference among the lipids are rather small, their effects on the body vary much. The hypothetical mechanism is associated with the difference in fluidity of membrane. Cancer cells have usually more fluid cell membrane with more unsaturated lipids, whereas the normal cell has more stable membranes with more cholesterol.

The phase transition temperature of DPPC, DMPC, and DLPC are 40°C, 23°C,

and 0°C, respectively. Thus, at the body temperature, DPPC is in the gel phase, which must be very rigid. On the other hand, the other two lipid membranes are in the sol phase, which must be more fluid and soft. Especially, DLPC lipid membrane should be quite fluid.

The first approach to understand such phenomena *in silico* must be the understanding of phase transitions of lipid bilayer systems. Even with such great interests and importance, the reliable results seem to be still scarce. Thus, we applied replica-exchange molecular dynamics (REMD) method [5, 7], one of the generalized-ensemble algorithms, to the lipid bilayer systems [14, 15] (see Chapter 2). Note that this is the first application of generalized-ensemble algorithms to lipid systems to our knowledge. This is given at the first part of this thesis.

Although REMD has been very efficient for the simulations of the lipid systems, the crossing over phase transition point will be more and more difficult, as the system size increases. We thus want to develop more powerful generalized-ensemble algorithms.

In the second part of this thesis, we focus on the ST method, which has some similarity to REM. These two methods have not been very compatible with first-order phase transitions. We propose an extension of ST method for spin systems, which turned out to be applicable to systems with first-order phase transitions [16, 17]. In this ST method, not only temperature but also external field is treated as a dynamical variable. Thus, this method can be referred to as "Simulated Tempering and Magnetizing (STM)."

This thesis consists of the following parts. In Chapter 2, we give the results of application of REMD to coarse-grained lipid bilayer systems, which is aimed at the deeper understanding of its phase transition mechanisms. In chapter 3, we introduce the STM. We then present the results of STM simulations applied to the two-dimensional Ising model. Chapter 4 is devoted to a further application of STM to the two-dimensional three-state Potts model. In Chapter 5 we conclude this thesis. In the following appendices, we summarize some statistical techniques, which are important for analyzing errors of MC or MD simulation results that usually involve auto-correlations. We also give the relationship between the Ising model and lattice gas model.

References

[1] B. A. Berg and T. Neuhaus: *Physics Letters B* **267**, 249–253 (1991).

[2] B. A. Berg and T, Neuhaus: *Physical Review Letters* **68**, 9–12 (1992).

[3] A. P. Lyubartsev, A. A. Martsinovski, S. V. Shevkunov, and P. N. Vorontsov-Velyaminov: *The Journal of Chemical Physics* **96** 1776–1783 (1992).

[4] E. Marinari and G. Parisi: *Europhysics Letters* **19**, 451–458 (1992).

[5] K. Hukushima and K. Nemoto: *Journal of the Physics Society Japan* **65**, 1604–1608 (1996).

[6] C. J. Geyer: in *Computing Science and Statistics, Proceedings of the 23rd Symposium on the Interface*, edited by E. M. Keramidas (Interface Foundation of North America, 1991) pp. 156–163.

[7] Y. Sugita and Y. Okamoto: *Chem. Phys. Lett.* **314**, 141–151 (1999) .

[8] S. J. Singer and G. L. Nicolson: *Science* **175**, 720–731 (1972).

[9] K. Simons and E. Ikonen: *Nature* **387**, 569–572 (1997).

[10] R. Ueoka, Y. Matsumoto, K. Goto, H. Ichihara, and Y. Komizu: *Curr. Pharm. Des.* **17**, 1709–1719 (2011).

[11] K. Nakano, Y. Iwamoto, W. Takata, Y. Matsumoto and R. Ueoka: *Bioorg. Med. Chem. Lett.* **12**, 3251–3254 (2002).

[12] Y. Matsumoto, Y. Iwamoto, T. Matsushita and R. Ueoka: *Int. J. Cancer* **115**, 377–382 (2005).

[13] H. Nagami, K. Nakano, H. Ichihara, Y. Matsumoto and R. Ueoka: *Bioorg. Med. Chem. Lett.* **16**, 782–785 (2006).

[14] T. Nagai and Y. Okamoto: *Molecular Simulation* **38**, 437-441 (2012).

[15] T. Nagai, R. Ueoka, and Y. Okamoto: *Journal of Physical Society of Japan* **81**, 024002 (9 pages) (2012).

[16] T. Nagai and Y. Okamoto: *Physics Procedia* **38**, 100–104 (2012).

[17] T. Nagai and Y. Okamoto: *Phys. Rev. E* **86**, 056705 (12 pages) (2012); arXiv:1205.2523.

Chapter 2

Replica-Exchange Molecular Dynamics Simulation of Lipid Bilayer Systems with Coarse-Grained Model

T. Nagai, R. Ueoka, and Y. Okamoto: “Phase behavior of a lipid bilayer system studied by a replica-exchange molecular dynamics simulation, ” *Journal of the Physical Society of Japan* **81**, 024002 (9 pages) (2012).

T. Nagai and Y. Okamoto: “Replica-exchange molecular dynamics simulation of a lipid bilayer system with a coarse-grained model, ” *Molecular Simulation* **38**, 437-441 (2012).

2.1 Introduction

Biological membranes are mainly composed of lipids. Phosphocholine (PC) is known as a main component. A dipalmitoylphosphatidylcholine (DPPC) bilayer system has been studied as one of lipid bilayers. There have been many studies on DPPC bilayers by simulations (for reviews, see, e.g., Refs. [1] and [2]) and by experiments (for a review, see, e.g., Ref. [3]).

DPPC bilayers have many phases along temperature, pressure, and so on. Different phases have different features in lateral diffusion coefficient, thickness of bilayer area of lipids, etc.

Simulational studies of phase transitions with the change of the temperature have been challenging because of the hysteresis behavior. The system easily gets trapped in local-minimum-energy states. There have been a few all-atom simulations of the phase transitions. Vries *et al.* detected a ripple phase by annealing [4], Leekumjorn *et al.* performed annealing and heating simulations of several kinds of lipid bilayers and studied gel phases and transition states [5, 6].

Coarse-grained models have been employed by a number of groups [7, 8, 9, 10]. In coarse-grained models, several atoms make up one reaction site. By reducing the number of reaction sites, one can simulate a system in a shorter computational time and it is easier to simulate larger systems.

As for coarse-grained simulations, Stevens performed simulations of a DPPC bilayer with a coarse-grained model, and got a tilted gel phase [7]. Marrink and coworkers studied the sol-gel phase transitions [11, 12] with their own coarse-graind models, MARTINI [8] and MARTINI2.0 [8, 9]. The main simulation techniques of inducing the phase transitions was cooling or heating. With their model, they got an un-tilted gel phase of DPPC bilayer but did not get the tilted gel phase, though the tilted gel phase is also supported by experiments. They changed parameters of MARTINI temporarily to sample the tilted-gel phase. With MARTINI2.0 model, they only report tilted-gel phase with externally applied tension. In the present work, we applied the molecular dynamics (MD) version of the replica-exchange method [13], Replica-Exchange Molecular Dynamics (REMD) [14] to a DPPC bilayer system with a coarse-grained model MARTINI2.0. As far as we

know, this is the first application of a generalized-ensemble algorithm (for a review, see, e.g., Ref. [15]). to an explicit DPPC bilayer system. Using REMD lets one enhance conformational sampling efficiency and simulate a system in a wide range of temperature at once. Even though temperatures are changed during REMD simulations, the REMD method does not break the detailed balance at any temperature. Thus, we can obtain the well equilibrated states at all the temperatures investigated. That is, we can obtain more reliable results at low temperatures, and we can discuss temperature dependences more accurately than by conventional methods.

This article is organized as follows. In §2.2 we present the methods, definitions of some quantities, and simulation details. In §2.3 we present the results of our REMD simulations of the bilayer.

2.2 Materials and methods

We performed a replica-exchange molecular dynamics (REMD) [14] simulation with a coarse-grained model MARTINI2.0. In this section, we explain REMD, MARTINI, a number of definitions of physical values, and simulation details.

We first briefly review REMD. For details, see the literature [14]. In REMD simulations, M copies (or, replicas) of a system are simulated by the molecular dynamics method simultaneously at M different temperatures. Every certain number of simulation steps, one tries to exchange the temperatures without breaking equilibrium by using Metropolis criterion [16]. By exchanging the temperatures, replicas perform a random walk in the temperature space. This, in turn, induces a random walk in the energy space. The REMD was extended to *NPT* ensemble simulations, [17, 18, 19, 20] and we used this method in the *NPT* ensemble.

MARTINI is a coarse-grained model [8, 9] proposed by Marrink *et al*. They revised parameters in 2007 [9]. We used this version of MARTINI, which is referred to as MARTINI2.0. This force field has been extended to proteins [21] and carbohydrates [22].

Here, we summarize main points of MARTINI2.0. One reaction site of MAR-

TINI generally corresponds to four heavy atoms. In this model, reaction sites are classified into 18 groups, which have different parameters. The potential energy is given by

$$
\begin{aligned}
E &= E_{\text{bond}} + E_{\text{angle}} + E_{\text{vdW}} + E_{\text{Coulomb}} \,, && (2.1)\\
E_{\text{bond}} &= \sum_{\text{bond}} \frac{1}{2} K_{\text{bond}} \left(R - R_0\right)^2 \,, && (2.2)\\
E_{\text{angle}} &= \sum_{\text{angle}} \frac{1}{2} K_{\text{angle}} \left(\cos(\theta) - \cos(\theta_0)\right)^2 \,, && (2.3)\\
E_{\text{vdW}} &= \sum_{i,\,j} 4\epsilon_{ij} \left[\left(\frac{\sigma_{ij}}{r_{ij}} \right)^{12} - \left(\frac{\sigma_{ij}}{r_{ij}} \right)^{6} \right], && (2.4)\\
E_{\text{Coulomb}} &= \sum_{i,\,j} \frac{q_i q_j}{4\pi\epsilon_0\epsilon_r} \left(\frac{1}{r_{ij}} - \frac{5}{3r_c} + \frac{5r_{ij}^3}{3r_c^4} - \frac{r_{ij}^4}{r_c^4} \right), && (2.5)
\end{aligned}
$$

where R_0, K_{bond}, θ_0, and K_{angle} denote the equilibrium distance, its force coefficient, the equilibrium bond angle, and its force constant, respectively. ϵ_{ij} and σ_{ij} are the Lennard-Jones parameters, and r_{ij} is the distance between the i-th and j-th particles. q_i, ϵ_0, ϵ_r, and r_c denote the full charges, the dielectric constant of vacuum, the relative dielectric constant, and the cut-off distance (= 1.2 nm), respectively.

One of the specific characteristics of MARTINI2.0 is the employment of the anti-freeze particles. Because water particles in previous MARTINI tend to get frozen easily, the anti-freeze particles were added in order to prevent water from getting frozen. The Lennard-Jones parameters between an ordinary water particle and an anti-freeze particle are modified from that between ordinary water particles. The other parameters of anti-freeze particles are the same as those of ordinary water particles. Anti-freeze particles tend to break the long-distance order in water. See the literature [9] for details. Figure 2.1 shows the structure of a DPPC molecule and a water particle in MARTINI2.0. One DPPC molecule is represented by twelve particles. Four water molecules are represented by one particle.

The simulation details are as follows. The system contained 32 DPPC molecules

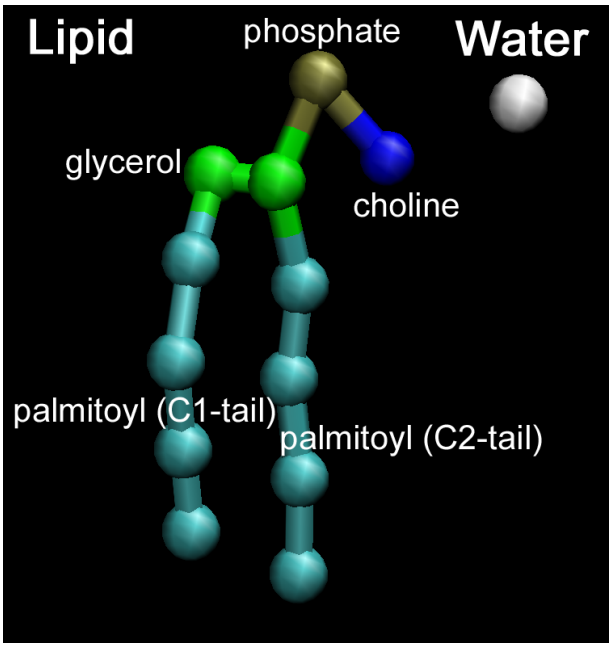

Figure 2.1: Structures of lipid and water particles in MARATINI2.0. The single spherical particle is a water particle. This corresponds to four water molecules. The other chain is a DPPC molecule. Twelve particles represent one DPPC molecule. One particle corresponds to choline, another corresponds to phosphate. Two particles are modeled as a glycerol backbone. Two sets of four particles (in light blue) stand for palmitoyl tails.

and 500 water particles. Fifty of those water particles were anti-freeze particles. The initial conformation was a DPPC bilayer in a sol phase. By heating and annealing the bilayer, we obtained a set of initial conformations for the REMD simulations. These bilayers were further equilibrated by REMD simulations. We then performed a 4.6-microsecond production REMD run per replica. The interval of replica exchanges was 100 MD steps. The interval may appear to be small. Because the REMD satsifies the detailed-balance condition, however, it is guaranteed to approach the thermal equiibrium no matter how often replica exchange is tried. We took a small interval, following the recommendation of Ref. [23]. The time step was 20 fs. In the production run, Nosé-Hoover thermostats [24, 25] and Parrinello-Rahman borostats [26] were employed. We employed semi-isotropic pressure controls, where the ratio of the x and y lengths of the simulation box was fixed, while the z length moves independently. Reference pressure of all components was 1 bar. We did not apply any surface tensions. Reference temperatures were distributed at 127 points between 283 and 390 K ($M = 127$): 283.00, 283.70, 284.40, 285.11, 285.81, 286.52, 287.23, 287.94, 288.66, 289.38, 290.10, 290.82, 291.54, 292.26, 292.99, 293.72, 294.45, 295.00, 295.25, 295.51, 295.76, 296.01, 296.27, 296.52, 296.77, 297.03, 297.28, 297.53, 297.78, 298.04, 298.29, 298.54, 298.78, 299.05, 299.30, 299.56, 299.81, 300.06, 300.32, 300.57, 300.82, 301.08, 301.33, 301.58, 301.84, 302.09, 302.34, 302.59, 302.85, 303.10, 303.35, 303.61, 303.86, 304.11, 304.37, 304.62, 304.87, 305.13, 305.38, 305.63, 305.89, 306.14, 306.39, 306.65, 306.90, 307.15, 307.41, 307.66, 307.91, 308.16, 308.42, 308.67, 308.92, 309.18, 309.43, 309.68, 309.94, 310.19, 310.44, 310.70, 310.95, 311.20, 311.46, 311.71, 311.96, 312.22, 312.47, 312.72, 312.97, 313.23, 313.48, 313.73, 313.99, 314.24, 314.49, 314.75, 315.00, 317.21, 319.44, 321.69, 323.95, 326.24, 328.54, 330.87, 333.21, 335.57, 337.95, 340.36, 342.78, 345.22, 347.68, 350.17, 352.67, 355.20, 357.74, 360.31, 362.90, 365.51, 368.14, 370.79, 373.47, 376.17, 378.89, 381.63, 384.40, 387.19, and 390.00 K. Figure 2.2 shows the temperature distribution. A smaller index is assigned to a lower temperature. We assigned a high density distribution of temperatures around sol-gel phase transition point because one needs a lot of replicas around critical temperatures. The highest temperature was chosen so that the bilayer does not break. The lowest temperature

was chosen so that it was lower than the sol-gel phase transition temperature. We used a package software, GROMACS-4.0.5 [27, 28, 29, 30], for all the simulations.

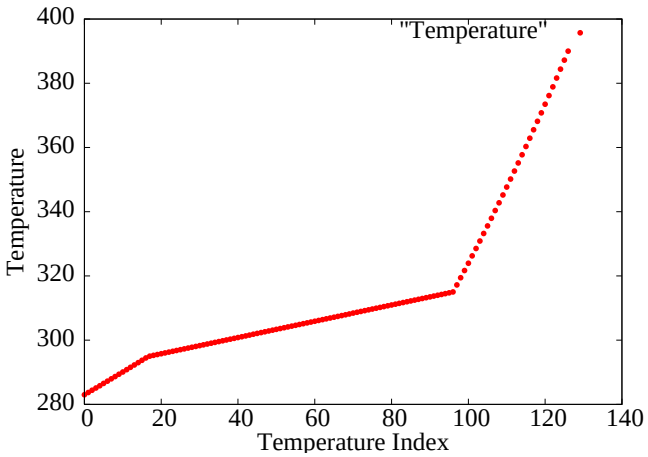

Figure 2.2: Temperature distribution for the REMD simulation. Each point corresponds to a replica.

We now describe the way of calculation of the thickness of a bilayer and the area of a bilayer, etc. The thickness of a bilayer is defined to be the distance between the center of mass of phosphate particles in the upper layer and that in the lower layer. The area of a bilayer is considered to be the area of base of the simulation box. By dividing this area by the number of lipids in a leaflet, we calculate the area per lipid. The tilt angle was defined as follows. In MARTINI, a C2 tail of DPPC has four particles. The angle of the line which passes through both the first particle and the last particle in a C2 tail to the unit vector parallel to the z axis from the last particle is defined as the tilt angle.

2.3 Results and discussion

Figure 2.3 shows the time series of the temperature index of one of the replicas during the REMD simulation of the DPPC bilayer. Figure 2.3 shows that this replica made a random walk in the temperature space between the highest tem-

perature and approximately the tenth lowest temperature. This suggests that the REMD simulation was performed properly. Around the tenth lowest temperature, there is a phase transition point of water as we discuss below. The existence of the water phase transition prevents replicas from going down below the tenth lowest temperature around 290 K. Our results are quite reliable in the range above this temperature, above which the sol-gel phase transitions exist as is discussed below.

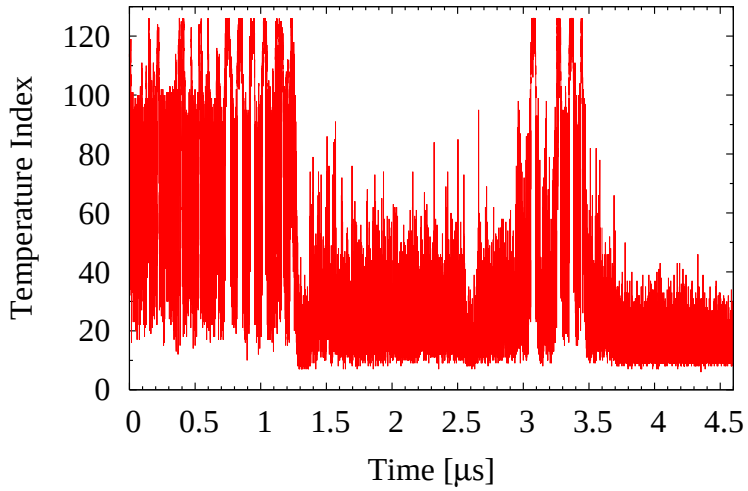

Figure 2.3: The history of temperature index in one of the replicas (Replica 113) during the REMD simulation of the DPPC bilayer with 32 lipids.

Figures 2.4 and 2.5 show the time series of the potential energy and the thickness of the bilayer, respectively, of the replica in Fig. 2.3. From Fig. 2.4, we see that the energy also made a random walk. Note that there is a strong and expected correlation between the behaviors in Figs. 2.3 and 2.4. According to Figs. 2.3 and 2.5, the bilayer is thick at low temperatures and thin at high temperatures. The thickness is a good parameter characterizing the phase. These results suggest that at high temperatures the bilayer is in the sol phase, where the bilayer is thin, and at low temperatures the bilayer is in the gel phase, where the bilayer is thick. This implies that the replica underwent several phase transitions during the simulation.

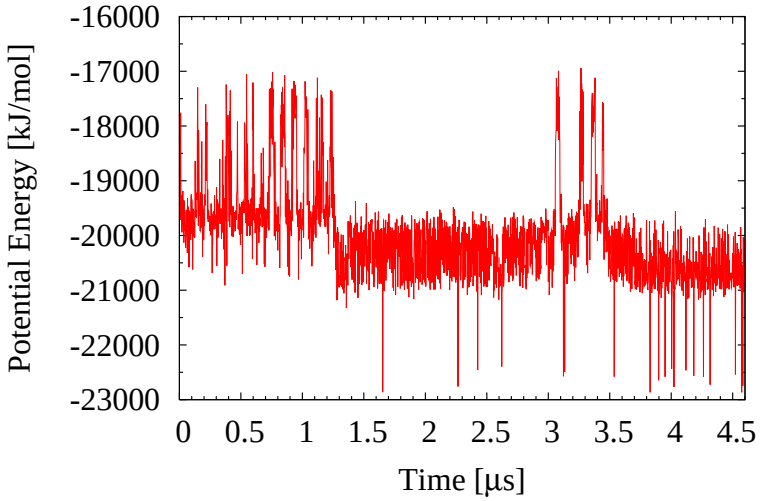

Figure 2.4: Potential energy of one of the replicas (Replica 113) as a function of time. The energy followed the movement of the temperature (see Fig. 2.3).

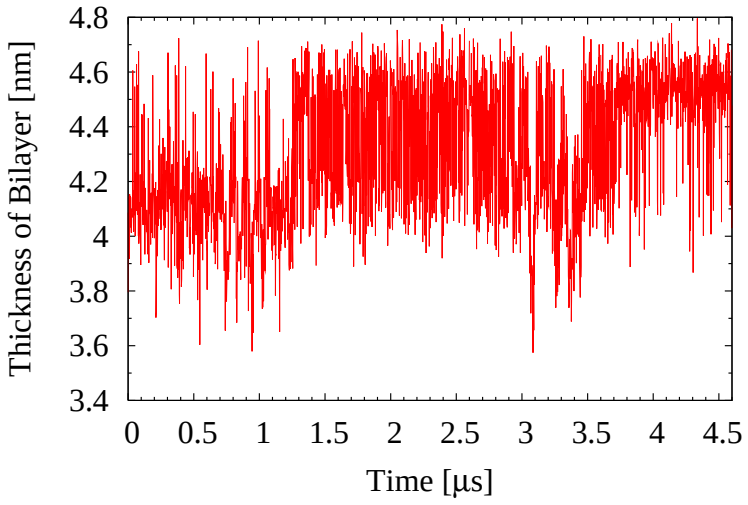

Figure 2.5: Thickness of the bilayer of one of the replicas (Replica 113) as a function of time.

In order to show the phase transition behavior clearly, we examine the temperature dependence of the enthalpy, etc. Figures 2.6, 2.7, 2.8, and 2.9 show the temperature dependence of the enthalpy, thickness of the bilayer, area per lipid, and heat capacity. respectively. Here, the heat capacity C is defined by

$$C = \frac{\left\langle (H + PV)^2 \right\rangle - \langle H + PV \rangle^2}{k_{\mathrm{B}} T^2} , \tag{2.6}$$

where H, P, V, k_{B}, and T are the sum of kinetic energy and potential energy, pressure, volume, Boltzmann constant, and temperature, respectively. Sudden changes of behaviors exist around 296 K in Figs. 2.6, 2.7, and 2.8. Other sudden changes of behaviors also exist around 288 K in Figs. 2.6 and 2.7. The heat capacity in Fig. 2.9 has two peaks around 288 K and 296 K, corresponding to the two sudden changes in the enthalpy in Fig. 2.6. According to these results, two phase transitions were found.

The phase transition around 288 K is the phase transition of water. The sudden changes of enthalpy around this temperature in Fig. 2.6 mainly consist of the sudden changes of LJ potential energy between water particles (see Fig. 2.15 below). Note that the enthalpy changes in Fig. 2.6 around 288 K are large. These are correlated to large changes in energy around this temperature. The large differences in the energy are the reason why the replica exchanges were not successful around this point.

The other phase transition around 296 K corresponds to the sol-gel phase transition of the DPPC bilayer. This is supported by the sudden changes of thickness and area around 296 K in Figs. 2.7 and 2.8. The phase characteristics were reproduced that the bilayer is thin and wide above the temperature and thick and narrow under the temperature. The sol-gel phase transition is also suggested by the temperature dependence of the LJ potential energy between DPPC molecules (see Fig. 2.13 below). The sol-gol phase transition temperature is consistent with the previous work [11] by Marrink *et al.* They reported that the transition temperature is 295 ±5 K.

The area per lipid in different phases was discussed in Ref. [3]. Their estimates

of the area per lipid for the gel phase (20°C) and for sol phase (50°C) are 0.479 and 0.64 nm^2, respectively. Our results are in accord with these values.

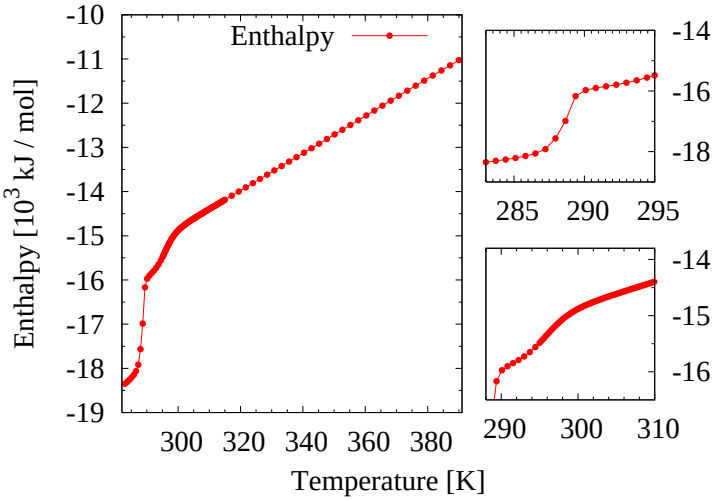

Figure 2.6: Enthalpy as a function of temperature. The graphs on the right are the same with different ranges of the ordinate and abscissa. The enthalpy has two large changes around 288 K and 296 K.

We now examine some component energy terms as functions of the temperature to further analyze the phase behaviors.

Figure 2.10 shows the average bond-length energy, $\langle E_{\text{bond}} \rangle$, as a function of temperature. This term has two sudden changes around 296 K and 288 K. Its manner of change around 296 K differs from that of the enthalpy in Fig. 2.6.

Figure 2.11 shows the average angle energy, $\left\langle E_{\text{angle}} \right\rangle$, as a function of temperature. This term also has two sudden changes around 296 K and 288 K. Its manner of change around 296 K is the same as that of the enthalpy in Fig. 2.6.

Figure 2.12 shows the average Coulombic energy as a function of temperature. Note that partial charges exist only in the head groups of lipids. This term also has two sudden changes around 296 K and 288 K. Its manner of change around 296 K is the same as that of the enthalpy in Fig. 2.6.

Figure 2.13 shows the temperature dependence of the average LJ potential energy between DPPC particles. This term changes largely around 296 K. This

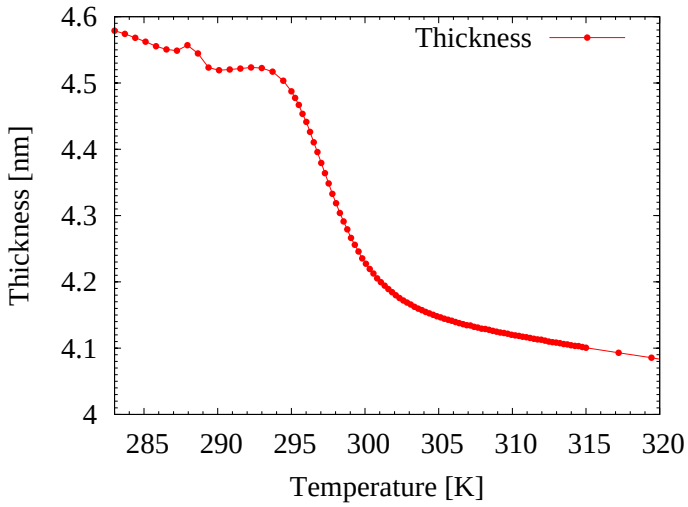

Figure 2.7: Average thickness of the bilayer as a function of temperature. Large changes exist around 296 K.

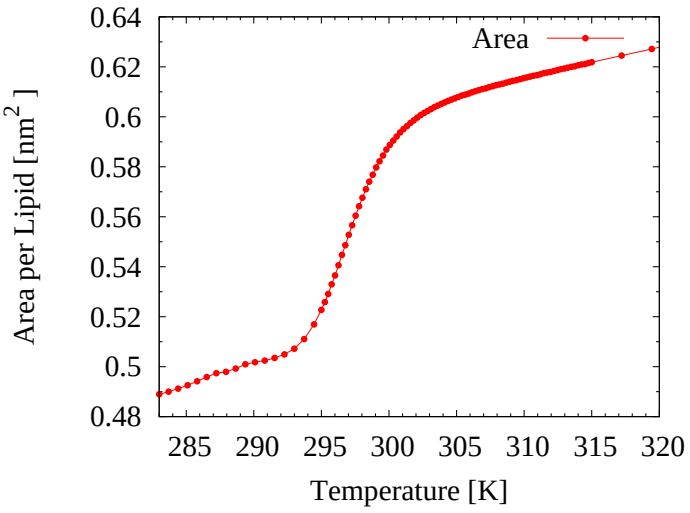

Figure 2.8: Average area per lipid as a function of temperature. There are huge changes around 296 K.

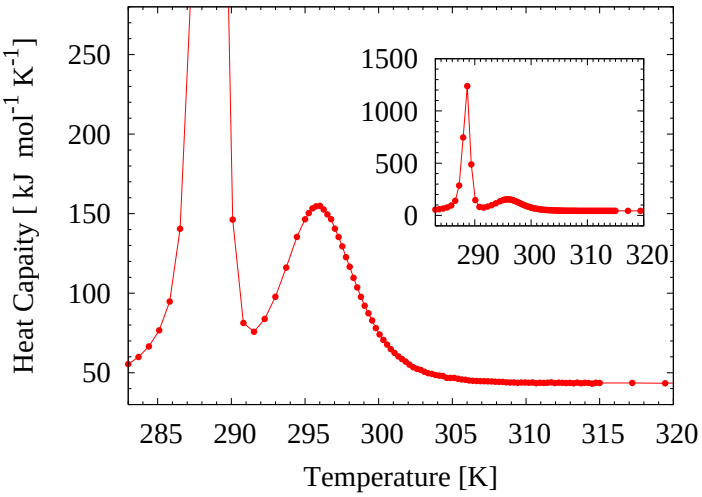

Figure 2.9: Heat capacity as a function of temperature. Two peaks exist around 288 K and 296 K. The graph in the inset is the same one with a different range of the ordinate.

large change corresponds to the sol-gel phase transition. The manner of the large change around this temperature is the same as that of the enthalpy, and this sudden change is the main cause of the sudden change of enthalpy around 296 K in Fig. 2.6. Hence, this term can be considered to be a driving force of the phase transition to the gel phase.

Figure 2.14 shows the temperature dependence of the average LJ potential energy between DPPC particles and water particles. This is the only interaction between a DPPC molecule and a water molecule. This has sudden changes around 296 K and 288 K. The manner of change around 296 K is opposite to the change of the enthalpy around 296 K in Fig. 2.6.

Figure 2.15 shows the temperature dependence of the average LJ potential energy between water particles. This has sudden changes around 296 K and 288 K. The latter one is quite huge, and this composes most of the sudden change of enthalpy around 288 K in Fig. 2.6. This sudden and huge change suggests that water got frozen around 288 K in our simulation.

We remark that two of the energy terms in Figs. 2.10 and 2.14 increase around

296 K as the temperature decreases. One term is the bond-length energy. The other one is the LJ potential energy between DPPC molecules and water molecules. These two terms favor the sol phase around the phase transition temperature, while the other terms favor the gel phase.

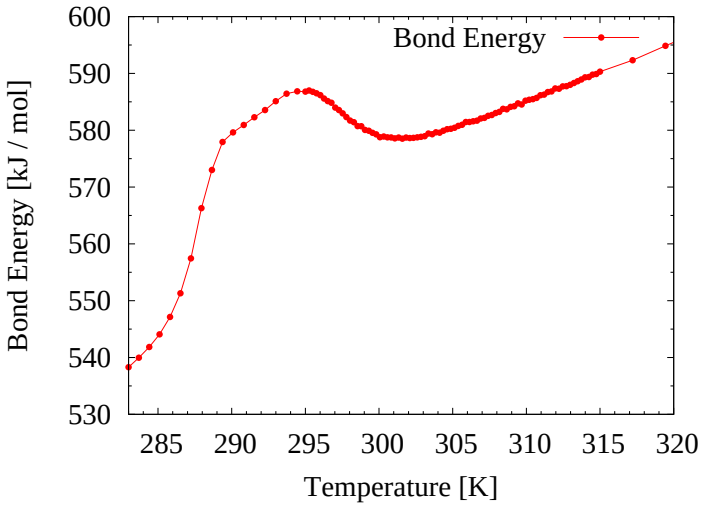

Figure 2.10: Average bond-length energy, $\langle E_{\mathrm{bond}} \rangle$, as a function of temperature.

In order to investigate the conformational features, we analyzed the potential of mean force (PMF) maps. PMF is defined by

$$W(\xi_1, \xi_2) = -k_{\mathrm{B}} T \log \rho(\xi_1, \xi_2) \,, \tag{2.7}$$

where $\rho(\xi_1, \xi_2)$ is the probability distribution of a point (ξ_1, ξ_2) and is given by

$$\rho(\xi_1, \xi_2) = \frac{\int \delta(\xi_1(q) - \xi_1)\delta(\xi_2(q) - \xi_2) e^{-\beta(H+PV)} \, d\boldsymbol{p} \, d\boldsymbol{q} \, dV}{\int e^{-\beta(H+PV)} \, d\boldsymbol{p} \, d\boldsymbol{q} \, dV} \,, \tag{2.8}$$

where H, P, V, $\boldsymbol{p}$, and $\boldsymbol{q}$ are the sum of kinetic energy and potential energy, pressure, volume, momenta, and coordinates, respectively.

Figure 2.16 shows PMF maps at four temperatures. One axis is the thickness of the bilayer, the other one is the area of the bilayer, and the height shows the

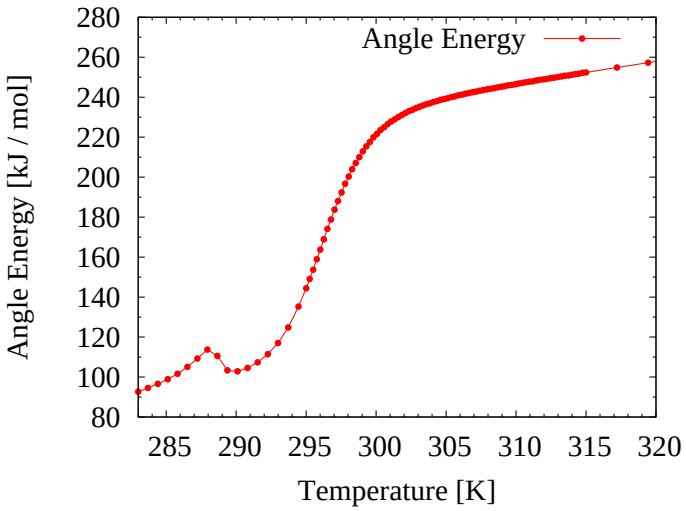

Figure 2.11: Average angle energy, $\langle E_{\text{angle}} \rangle$, as a function of temperature.

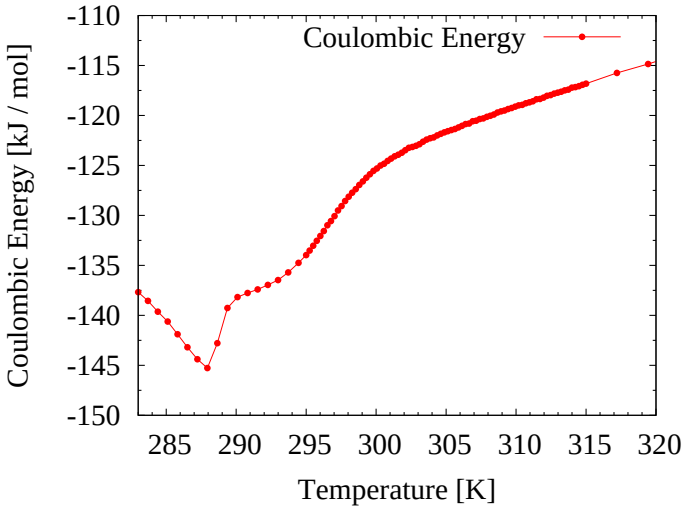

Figure 2.12: Average Coulombic energy, as a function of temperature.

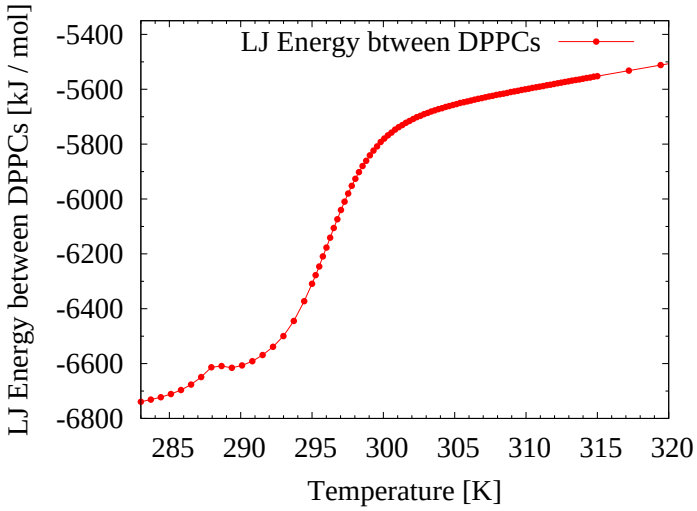

Figure 2.13: Average LJ potential energy between DPPC particles as a function of temperature.

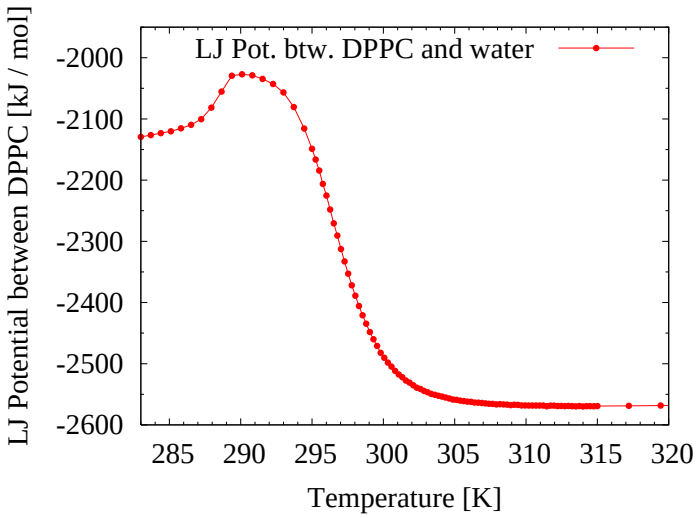

Figure 2.14: Average LJ potential energy between DPPC particles and water particles as a function of temperature.

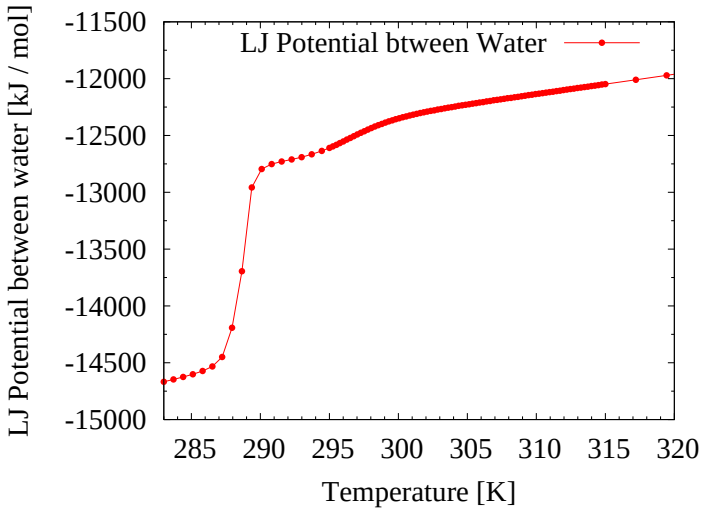

Figure 2.15: Average LJ potential energy between water particles as a function of temperature.

PMF. The curves on the *xy*-plane are the contours of the PMF. At the temperature of 305.9 K, there is one local minimum (see Fig. 2.16(a)). The temperature is high enough for the bilayer to be in the sol phase. This minimum corresponds to the sol phase. In the sol phase, the bilayer is thin and wide. At the temperature of 297.8 K, there are two local minima (see Fig. 2.16(b)). The new local minimum corresponds to the gel phase. In the gel phase, the bilayer is thick and narrow. At the temperature of 295.5 K, there are three local minima (see Fig. 2.16(c)). This temperature is slightly lower than the previous one. This result suggests that two gel phases exist. The newest one is thinner than the second newest minimum. These two minima correspond to the un-tilted gel phase and the tilted-gel phase, respectively. At the temperature of 293.0 K there are two local minima (see Fig. 2.16(d)). One of the local minima seen in 295.5 K and 297.8 K disappeared. In this temperature, the bilayer is mainly in the tilted-gel phase. These results suggest that the sol-gel phase transitions are composed of two phase transitions. Figure 2.17 shows the PMF map at 295.76 K, which also shows three local minima of free energy.

In order to check the significance of the difference between the tilted gel

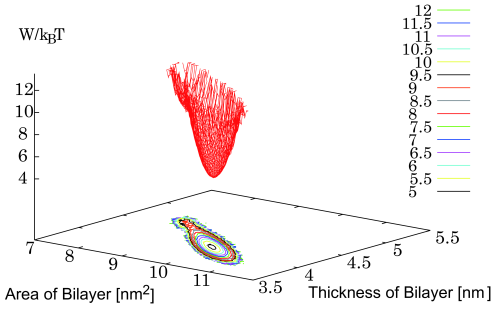

(a) PMF map at 305.9 K.

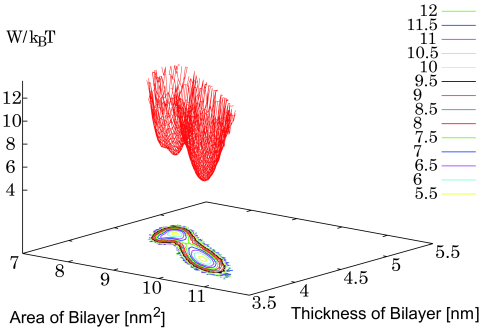

(b) PMF map at 297.8 K.

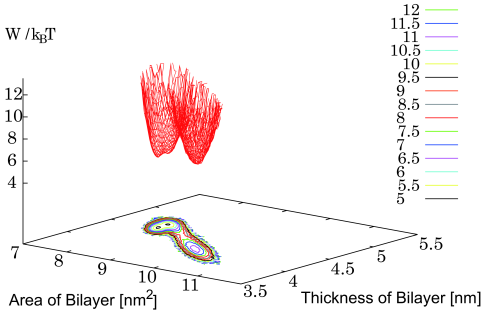

(c) PMF map at 295.5 K.

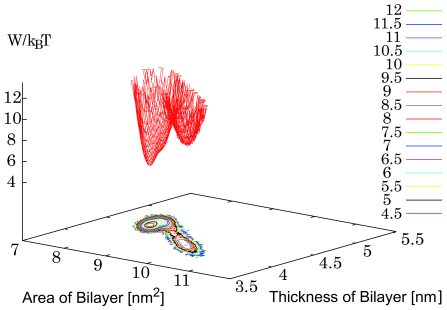

(d) PMF map at 293.0 K.

Figure 2.16: Two-dimensional PMF maps.

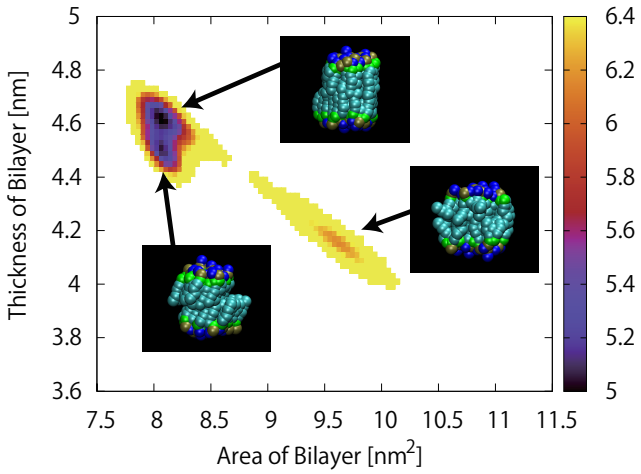

Figure 2.17: PMF map at 295.76 K. The color is assigned according to the PMF values divided by $k_{\mathrm{B}}T$

phase and un-tilted gel phase, we evaluated errors of histograms by following calculations [31]. Firstly we divided the obtained trajectory into sixteen parts. Each data was converted into a histogram and we obtained sixteen histograms. These histograms are denoted as $h_1(x,y),\ldots,h_{16}(x,y)$, where x and y stands for the bilayer thickness and area. The error bars of the histograms, $\sigma(x,y)$ are calculated by $\sigma^2(x,y) = \left(\sum_{i=1}^{16}(h_i - \langle h(x,y)\rangle)^2\right)/16(16-1)$, where $\langle h(x,y)\rangle$ is the average of sixteen histograms, or the histogram with all data. Finally, the obtained σ was converted into the error of PMF by $\sigma(x,y)/\langle h(x,y)\rangle$. Note that $\log(x+\delta x) \approx \log x + \delta x/x$. Figure 2.18 shows the PMF with error bars at 295.5 K. Note that data are shown only where the bilayer thickness is 8.04 nm^2. The statistically significant barrier exists between two local minima, which correspond to the un-tilted gel phase and tilted gel phase.

To roughly estimate the phase transition temperature, we looked for the temperature where each minimum has the same depth as each other. For this purpose, we checked the PMFs at all temperatures. At 297.8 K (Fig. 2.16(b)) or 297.5 K the depth of the un-tilted gel becomes the same as that of the sol phase. At 295.5 K the depth of tilted-gel becomes that of the un-tilted gel phase. Note that at this tem-

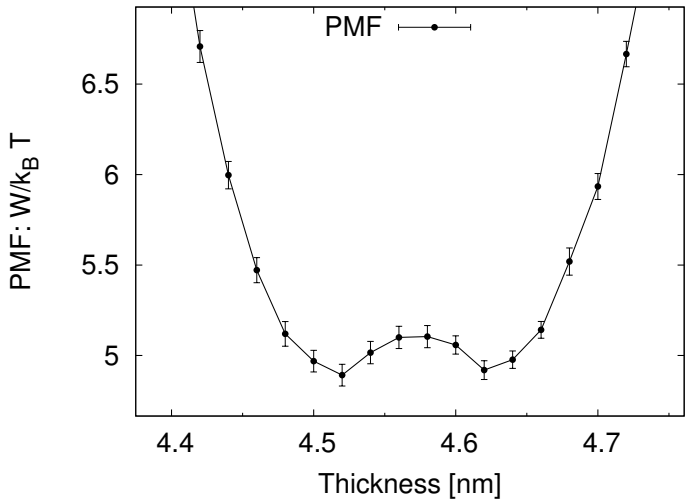

Figure 2.18: PMF with error bars where bilayer area is 8.04 nm^2 at 295.5 K. The solid curve is just a guide.

perature the depth of the sol is still large as can been seen in Fig. 2.16(c). These two temperatures are not so far from the phase transition temperature deduced by the enthalpy or the heat capacity in Fig. 2.6 or Fig. 2.9, respectively.

It might be a natural question why we could not get another peak in the heat capacity in Fig. 2.9 so that the two peaks correspond to the two phase transitions discussed with PMF maps. There are several possible reasons. One is the error of simulation is still not small enough to distinguish the peaks. Another is that the system is too small to distinguish the two peaks. The third is that the heat capacity has really one peak. One of the phase transitions discussed by the PMF maps belongs to the other.

To investigate conformational features further, we analyzed the tilt angle distributions. This helps understanding of the correspondence between PMF maps and conformational characteristics. Figure 2.19 shows distributions of the tilt angle of C2 tails at the four temperatures. The same temperatures are chosen as in the PMF maps. At the temperature of 305.9 K, the tilt angles of C2 tails have a broad distribution. This means that the lipids are in the sol phase, in which the C2 tails are not ordered. At the temperature of 297.8 K, the tilt angles of C2 tails are

located between 10° and 30°. At the temperature of 295.5 K, the tilt angles are located beween 10° and 30°. At 10° their distribution has a small peak, and at 30° it has a large peak. This suggests that there are two state. One is an un-tilted phase and the other one is a tilted phase. At the temperature of 293.0 K the tilt angles of C2 tails are located around 30°. These results also suggest that three states exist. One is the sol phase, another one is the un-tilted gel phase, and the third one is the tilted gel phase. The tilt angle in the tilted gel phase is around 30°.

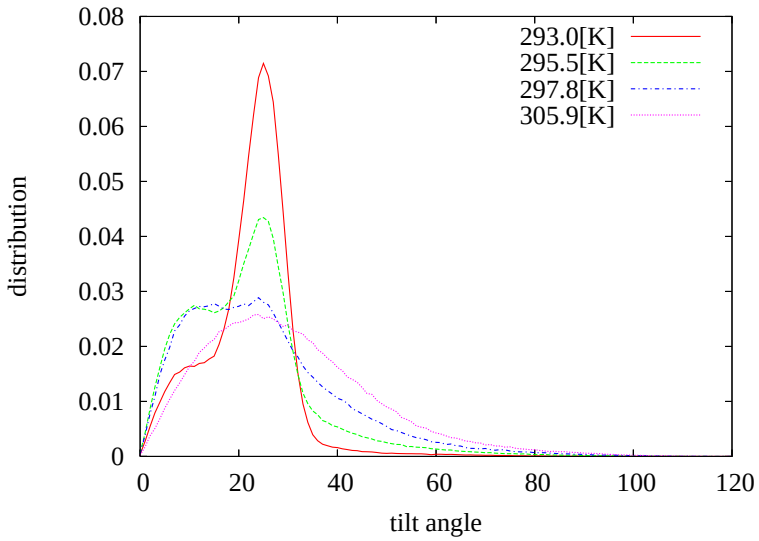

Figure 2.19: The tilt angle distributions. The solid red line shows one at 293.0 K, the green dash line shows one at 295.5 K, the blue dash-dot line shows one at 297.8 K, and the purple dot line shows one at 305.9 K.

Figure 2.20 shows snapshots of the bilayer obtained during the REMD simulation. Figures 2.20(a), 2.20(b), and 2.20(c) correspond to the sol phase, the un-tilted gel phase, and the tilted-gel phase, respectively. The values of the area and the thickness of the bilayer are 9.91 nm^2 and 4.09 nm, 7.91 nm^2 and 4.65 nm, and 8.10 nm^2 and 4.37 nm, respectively.

In order to ensure the validity of the results presented so far, we also performed simulations of larger systems, which consists of 72 and 128 lipids. The simulation

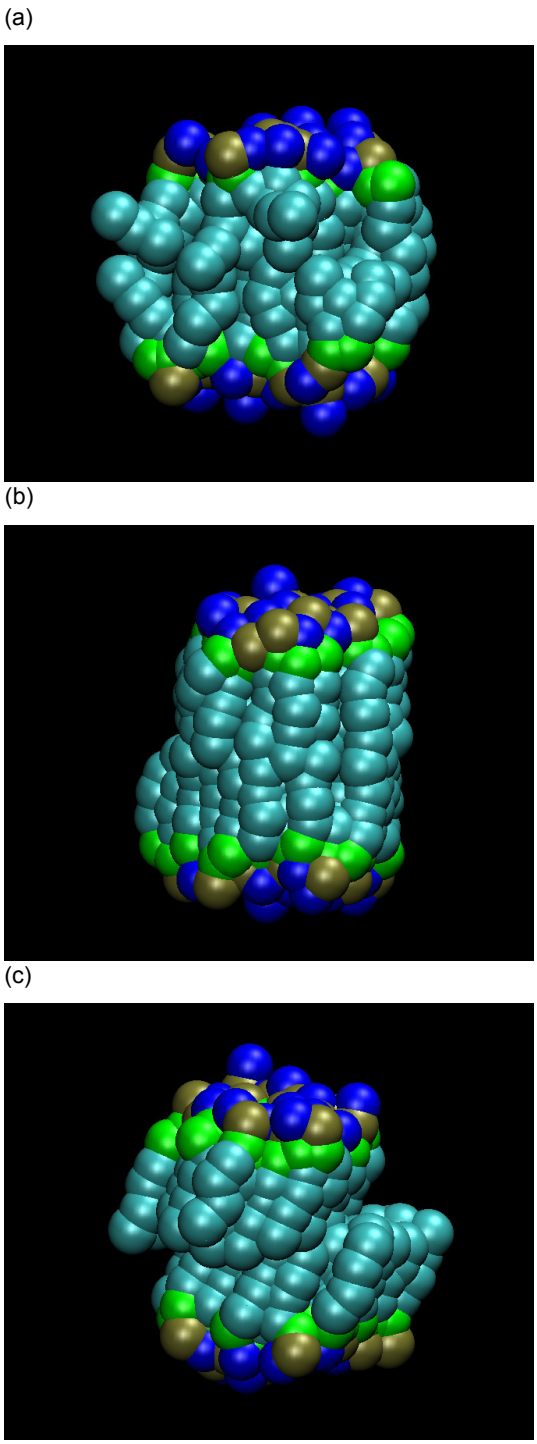

Figure 2.20: Snapshots of three states of the DPPC bilayer with 32 lipids during the REMD simulation. Water particles are suppressed for clarity.

conditions such as thermostats and barostats, are almost the same as the those of the smallest system. Although the results are still preliminary, they already show consistency with those of the smallest-system simulation. For instance, Figures 2.21 and 2.22 shows three snapshots obtained in the 72-lipid simulation and in the 128-lipid simulation, respectively, which correspond to the three states found in the 32-lipid simulations.

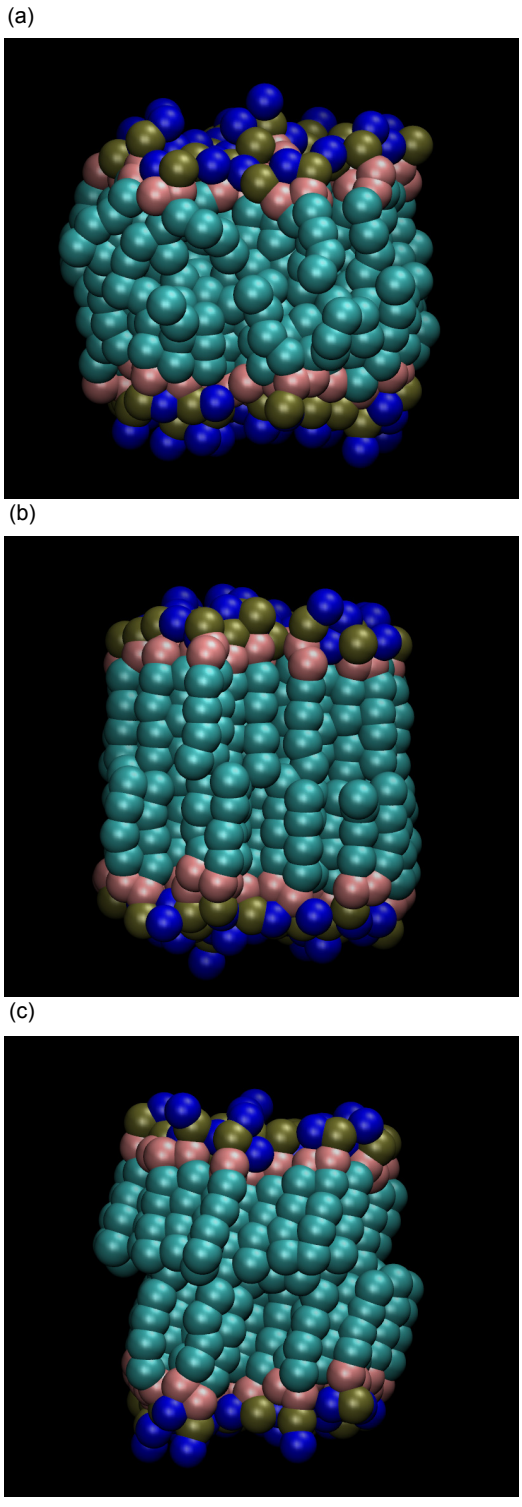

Figure 2.21: Snapshots of three states of the DPPC bilayer with 72 lipids obtained by the REMD simulation. Water particles are suppressed for clarity.

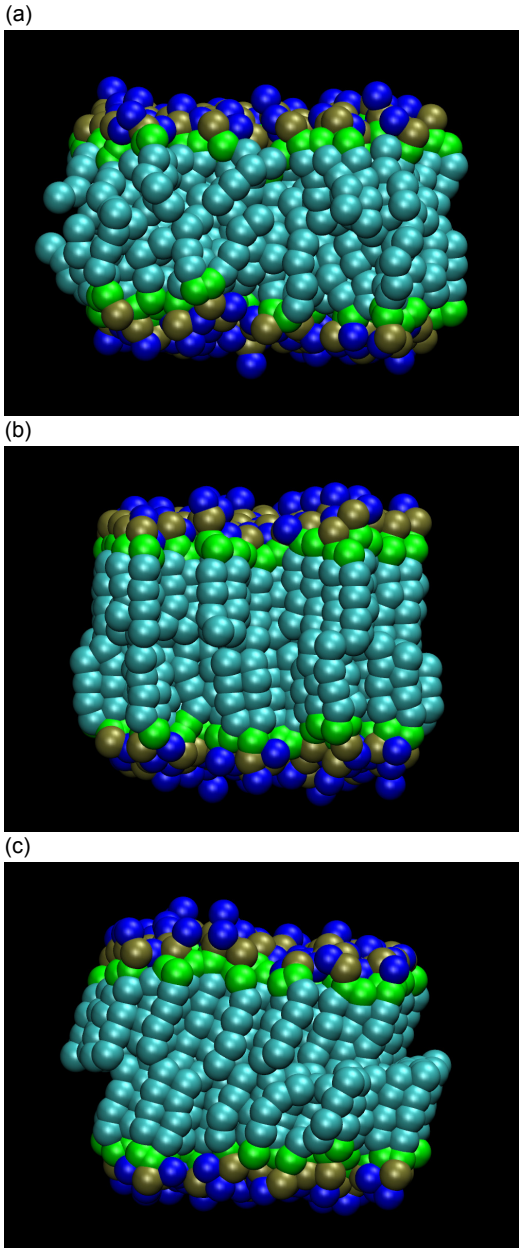

Figure 2.22: Snapshots of three states of the DPPC bilayer with 128 lipids obtained by the REMD simulation. Water particles are suppressed for clarity.

References

[1] D. Tieleman, S. Marrink, and H. Berendsen: *Biochimica et Biophysica Acta-Reviews on Biomembranes* **1331**, 235–270 (1997) .

[2] L. Saiz and M. L. Klein: *Acc. Chem. Res.* **35**, 482–489 (2002).

[3] J. Nagle and S. Tristram-Nagle: *Biochimica et Biophysica Acta-Reviews on Biomembranes* **1469**, 159–195 (2000).

[4] A. de Vries, S. Yefimov, A. Mark, and S. Marrink: *Proc. Natl. Acad. Sci. U.S.A.* **102**, 5392–5396 (2005).

[5] S. Leekumjorn and A. Sum: *Biochim. Biophys. Acta -Biomembranes* **1768**, 354–365 (2007).

[6] S. Leekumjorn and A. Sum: *J. Phys. Chem. B* **111**, 6026–6033 (2007).

[7] M. Stevens: *J. Chem. Phys.* **121**, 11942 (7 pages) (2004).

[8] S. J. Marrink, A. H. de Vries, and A. E. Mark: *J. Phys. Chem. B* **108**, 750–760 (2004).

[9] S. J. Marrink, H. J. Risselada, S. Yefimov, D. P. Tieleman, and A. H. de Vries: *J. Phys. Chem. B* **111**, 7812–7824 (2007).

[10] W. Shinoda, R. DeVane, and M. L. Klein: *Mol. Simul.* **33**, 27–36 (2007).

[11] S. J. Marrink, H. J. Risselada, and A. E. Mark: *Chem. Phys. Lipids* **135**, 223–244 (2005) .

[12] J. Risselada and S. Marrink: *Soft Matter* **5**, 4531–4541 (2009) .

[13] K. Hukushima and K. Nemoto: *J. Phys. Soc. Jpn.* **65**, 1604–1608 (1996).

[14] Y. Sugita and Y. Okamoto: *Chem. Phys. Lett.* **314**, 141–151 (1999) .

[15] A. Mitsutake, Y. Sugita, and Y. Okamoto: *Biopolymers* **60**, 96–123 (2001).

[16] N. Metropolis, A. Rosenbluth, M. Rosenbluth, A. Teller, and E. Teller: *J. Chem. Phys.* **21**, 1087 (6 pages) (1953) .

[17] T. Nishikawa, H. Ohtsuka, Y. Sugita, M. Mikami, and Y. Okamoto: *Progress of Theoretical Physics supplement* **138**, 270–271 (2000).

[18] T. Okabe, M. Kawata, Y. Okamoto, and M. Mikami: *Chem. Phys. Lett.* **335**, 435–439 (2001) .

[19] Y. Sugita and Y. Okamoto: in *Lecture Notes in Computational Science and Engineering*, edited by T. Schlick and H. H. Gan (Springer, Berlin, 2002) pp. 304–332; e-print: cond-mat/0102296.

[20] D. Paschek and A. E. Garcia: *Phys. Rev. Lett.* **93**, 238105 (4 pages) (2004).

[21] L. Monticelli, S. K. Kandasamy, X. Periole, R. G. Larson, D. P. Tieleman, and S. J. Marrink: *J. Chem. Theory Comput.* **4**, 819–834 (2008).

[22] C. A. López, A. J. Rzepiela, A. H. de Vries, L. Dijkhuizen, P. H. Hünenberger, and S. J. Marrink: *J. Chem. Theory Comput.* **5**, 3195–3210 (2009).

[23] D. Sindhikara, Y. Meng, and A. E. Roitberg: *J. Chem. Phys.* **128**, 024103 (10 pages) (2008).

[24] S. Nosé: *Mol. Phys.* **52**, 255–268 (1984).

[25] W. Hoover: *Phys. Rev., A* **31**, 1695–1697 (1985).

[26] M. Parrinello and A. Rahman: *J. Appl. Phys.* **52**, 7182 (9 pages) (1981) .

[27] H. Berendsen, D. Van der Spoel, and R. Van Drunen: *Comput. Phys. Commun.* **91**, 43–56 (1995).

[28] E. Lindahl, B. Hess, and D. van der Spoel: *J. Mol. Model* **7**, 306–317 (2001) .

[29] D. Van Der Spoel, E. Lindahl, B. Hess, G. Groenhof, A. Mark, and H. Berendsen: *J. Comput. Chem.* **26**, 1701–1718 (2005).

[30] B. Hess, C. Kutzner, D. van der Spoel, and E. Lindahl: *J. Chem. Theory Comput.* **4**, 435–447 (2008).

[31] H. Flyvbjerg and H. G. Petersen: *J. Chem. Phys.* **91**, 461 (6 pages) (1989) .

[32] K. Nakano, Y. Iwamoto, W. Takata, Y. Matsumoto, and R. Ueoka: *Bioorg. Med. Chem. Lett.* **12**, 3251–3254 (2002) .

[33] Y. Matsumoto, Y. Iwamoto, T. Matsushita, and R. Ueoka: *Int. J. Cancer* **115**, 377–382 (2005) .

[34] H. Nagami, K. Nakano, H. Ichihara, Y. Matsumoto, and R. Ueoka: *Bioorg. Med. Chem. Lett.* **16**, 782–785 (2006).

[35] R. Ueoka, Y. Matsumoto, K. Goto, H. Ichihara, and Y. Komizu: *Curr. Pharm. Des.* **17**, 1709–1719 (2011) .

Chapter 3

Simulated Tempering and Magnetizing: Application of Two-Dimensional ST Method to an Ising Model

T. Nagai and Y. Okamoto: "Simulated tempering and magnetizing: application of two-dimensional simulated tempering to two-dimensional Ising model and its crossover," *Physical Review E* **86**, 056705 (12 pages) (2012); arXiv:1205.2523.

T. Nagai and Y. Okamoto: "Simulated tempering and magnetizing of the Ising model," *Physics Procedia* **38**, 100–104 (2012).

3.1 Introduction

In the computational statistical physics field, Monte Carlo (MC) and molecular dynamics (MD) simulations have been commonly used. However, the quasi-ergodicity problem, where simulations tend to get trapped in states of energy local-minimum, has often posed a great difficulty. In order to overcome this difficulty, generalized-ensemble algorithms have been developed and applied to many systems including spin systems and biomolecular systems (for reviews, see, e.g., Refs. [1, 2, 3]).

Commonly used examples of generalized-ensemble algorithms are the multicanonical algorithm (MUCA) [4, 5], simulated tempering (ST) method [6, 7], and replica-exchange method (REM) [8, 9] (it is also referred to as parallel tempering). Closely related to MUCA are the Wang-Landau method [10, 11] and metadynamics [12]. Also closely related to REM is the method in Ref. [13].

In the ST method, temperature is regarded as a dynamical variable, which is updated by the Metropolis criteria during the simulation, and consequently a random walk is realized in the temperature space. This random walk, in turn, causes a random walk of the energy, which enables the system in question to overcome free-energy barriers. However, it is well-known that the ST method is not very compatible with first-order phase transitions (for a review, see, e.g., Ref. [14]). When there is a first-order phase transition, the random walk of temperature across the phase-transition point hardly occurs. We remark that there is a recent attempt to deal with this difficulty by an extension of ST [15].

Recently, the multi-dimensional generalizations of the generalized-ensemble algorithms, including the MUCA, ST, and REM, were discussed and general formalisms were given [16, 17, 18]. In these methods, the energy of the system is generalized by adding other energy term(s) with some coupling constants. In the multi-dimensional ST method, not only the temperature but also the coupling constants are considered as dynamical variables.

In this work, we study a special case of the above general multi-dimensional ST methods. Namely, the additional term is $-hM$ where h and M are the external field and the magnetization, respectively. The external field h corresponds to the

couping constant which is updated during MC simulations. Therefore, not only temperature but also external field becomes a dynamical variable and is expected to realize a random walk during the simulations. Thus, this simulation can be referred to as the "Simulated Tempering and Magnetizing" (STM). In order to test the effectiveness of the present method, we applied it to the two-dimensional Ising model.

The Ising model has two kinds of phase transitions. One occurs along the change of temperature when the external field is zero. The other occurs along the change of external field when the temperature is under the critical temperature ($T_{\rm c}$). The former is classified as a second-order phase transition. The latter is categorized as a first-order phase transition unless the temperature is exactly equal to $T_{\rm c}$. When $T = T_{\rm c}$, the transitions are classified into a second-order phase transition. This system allows us to confirm applicability of the two-dimensional ST to the first-order phase transitions along the external field changes.

We also investigate the crossover phenomena in the phase transitions, in which critical exponents are changed. We study the behavior of magnetization per spin m, which follows $m \sim |T - T_{\rm c}|^{\beta}$ and $m \sim |h|^{1/\delta}$ near the critical point, where β and δ are critical exponents [19]. Our simulation method, with a combination of histogram reweighting techniques, enables us to calculate physical values such as the energy and magnetization at various values of T and h from a single production run.

This article is organized as follows. In §3.2 we present the STM method. In §3.3 we present the results.

3.2 Materials and methods

3.2.1 System

We study the two-dimensional Ising model in external field. The total energy is given by

$$H = E - hM\,, \tag{3.1}$$

$$E = -\sum_{\langle i,j\rangle} \sigma_i \sigma_j\,, \tag{3.2}$$

$$M = \sum_{i=1}^{N} \sigma_i\,, \tag{3.3}$$

where i, N, σ_i, and h are the index of spin, total number of spins, spin at the i-th site, and external field, respectively. The spin σ_i takes on the values ± 1. The sum in Eq. (3.2) goes over the nearest-neighbor pairs. The spins are arranged on the square $L \times L$ lattice. We imposed the periodic boundary conditions. Data were obtained for lattice sizes from 2×2 to 160×160.

3.2.2 Simulation methods

Whereas the conventional ST method considers temperature as a dynamical variable, the STM method considers not only temperature but also external field as a dynamical variable. Here, before explaining the STM method, we shortly review the conventional ST method [6, 7].

In the conventional ST method, temperature is a dynamical variable which takes on one of N_T values (here, temperature is discretized into N_T values). In other words, denoting X and x as a sampling space and its microscopic state, respectively, the Boltzmann factor

$$e^{-E(x)/T + a(T)} \tag{3.4}$$

is regarded as a joint probability for the state (x, T) $(\in X \otimes \{T_1, T_2, \ldots, T_{N_T}\})$. Here,

$a(T)$ (or $a(T_i)$) is a parameter for obtaining uniform distributions of temperature values. Here and hereafter, we set Boltzmann's constant to unity. Now that the temperature is a dynamical variable, the simulated system is allowed to realize a random walk in the temperature space. This random walk, in turn, causes a random walk of energy. Consequently, the simulated system has more chance to overcome energy barriers.

Even though the temperature changes during ST simulations, any thermodynamic quantity at temperature T_i, $\langle A \rangle_{T_i}$, can be reconstructed with the conditional expectation of a physical quantity A given at T_i, or $\langle A|T_i \rangle$. Note that

$$\langle A|T_i \rangle_{ST} = \frac{\sum_{j=1}^{N_T} \int dx A(x)\, \delta_{ij}\, e^{-\frac{E(x)}{T_j}+a(T_j)}}{\sum_{j=1}^{N_T} \int dx\, \delta_{ij}\, e^{-\frac{E(x)}{T_j}+a(T_j)}} \tag{3.5}$$

$$= \frac{\int dx\, A(x)\, e^{-\frac{E(x)}{T_i}+a(T_i)}}{\int dx\, e^{-\frac{E(x)}{T_i}+a(T_i)}} \tag{3.6}$$

$$= \langle A \rangle_{T_i} \ , \tag{3.7}$$

where δ_{ij} is the Kronecker delta. Namely, we have

$$\langle A \rangle_{T_i} = \frac{1}{N_{T_i}} \sum_{j=1}^{N_{T_i}} A^j_{T_i} \, , \tag{3.8}$$

where N_{T_i} and $A^j_{T_i}$ stand for the total number of samples and j-th sample at T_i.

To find a candidate for $a(T_i)$, let us look at the probability of visiting T_i. By

summing over the delta function, the probability of occupying T_i is given by

$$P(T_i) = \frac{\sum_{j=1}^{N_T} \int dx\, \delta_{ij}\, e^{-\frac{E(x)}{T_j}+a(T_j)}}{\sum_{j=1}^{N_T} \int dx\, e^{-\frac{E(x)}{T_j}+a(T_j)}} \tag{3.9}$$

$$= \frac{e^{-f(T_i)+a(T_i)}}{\sum_{j=1}^{N_T} e^{-f(T_j)+a(T_j)}} \tag{3.10}$$

$$\propto e^{-f(T_i)+a(T_i)}\,, \tag{3.11}$$

where f is the dimensionless (Helmholtz) free energy and

$$e^{-f(T)} \equiv \int dx\, e^{-E(x)/T}. \tag{3.12}$$

Substituting $f(T_i)$ into $a(T_i)$ gives constant probability regardless of T_i. Thus, the dimensionless free energy $f(T_i)$ is a good choice for $a(T_i)$ in order to obtain uniform temperature distribution and to realize a random walk in the temperature space. Although the free energy is not known *a priori*, unless the system is exactly solvable, the free energy calculation methods (the details will be provided below) enable us to get its good estimate from preliminary simulation runs.

In the two-dimensional ST algorithm, on the other hand, we consider that another parameter is also a dynamical variable [16, 17, 18]. Especially in the STM method, the external field h is a second dynamical variable. In other words, we consider

$$e^{-(E-hM)/T+a(T,h)} \tag{3.13}$$

as a joint probability for (x, T, h) $(\in X \otimes \{T_1, T_2, \ldots, T_{N_T}\} \otimes \{h_1, h_2, \ldots h_{N_h}\})$, where $a(T, h)$ is a parameter.

To find a candidate for $a(T_i, h_j)$, we again look at the probability of staying at

each set of parameter values. It is given by

$$P(T_i, h_j) = \frac{\sum_{k=1}^{N_T}\sum_{l=1}^{N_h}\int dx\,\delta_{ik}\,\delta_{jl}\,e^{-\frac{E(x)-h_l M(x)}{T_k}+a(T_k,h_l)}}{\sum_{k=1}^{N_T}\sum_{l=1}^{N_h}\int dx\,e^{-\frac{E(x)-h_l M(x)}{T_k}+a(T_k,h_l)}} \tag{3.14}$$

$$= \frac{e^{-f(T_i,h_j)+a(T_i,h_j)}}{\sum_{k=1}^{N_T}\sum_{l=1}^{N_h} e^{-f(T_k,h_l)+a(T_k,h_l)}} \tag{3.15}$$

$$\propto e^{-f(T_i,h_j)+a(T_i,h_j)}, \tag{3.16}$$

where

$$e^{-f(T_i,h_j)} = \int dx\, e^{-(E-h_j M)/T_i}. \tag{3.17}$$

The dimensionless free energy $f(T_i, h_j)$ is again a good choice for $a(T_i, h_j)$ in order to acquire a uniform distribution of T and h. These values can be estimated from preliminary simulation runs and reweighting techniques.

As in conventional ST method, any thermal average $\langle A\rangle_{T_i,h_j}$ at given T_i ($\in \{T_1, T_2, \ldots, T_{N_T}\}$) and h_j ($\in \{h_1, h_2, \ldots, h_{N_h}\}$) can be obtained by calculating the conditional expectation: $\langle A\rangle_{T_i,h_j} = \left\langle A|T_i, h_j\right\rangle_{ST}$. Namely, we have

$$\langle A\rangle_{T_i,h_j} = \frac{1}{N_{T_i,h_j}}\sum_{k=1}^{N_{T_i,h_j}} A^k_{T_i,h_j}, \tag{3.18}$$

where N_{T_i,h_j} is the total number of samples at T_i and h_j, and $A^k_{T_i,h_j}$ stands for the k-th sample at T_i and h_j.

The method of updating T or h is similar to that of updating spins because T and h are considered as dynamical variables. The Metropolis criterion for updat-

ing T or h is given by the following transition probability:

$$w(T_i, h_j \to T_{i'}, h_{j'}) = \min\left(1, \frac{P(T_{i'}, h_{j'})}{P(T_i, h_j)}\right) \tag{3.19}$$

$$= \min\left(1, \exp\left(-\left(\frac{1}{T_{i'}} - \frac{1}{T_i}\right)E + \left(\frac{h_{j'}}{T_{i'}} - \frac{h_j}{T_i}\right)M + a(T_{i'}, h_{j'}) - a(T_i, h_j)\right)\right). \tag{3.20}$$

Once an initial state is given, the STM simulations can be performed by repeating the following two steps. 1. We perform a conventional canonical simulation at T_i and h_j for certain MC sweeps. 2. We update the temperature or external field by Eq. (3.20) with $a(T, h) = f(T, h)$.

In our implementation every certain MC sweeps either T or h was updated (the choice between T and h was made at random) by Eq. (3.20) to a neighboring value (the choice of two neighbors was also made at random). Here, one MC sweep stands for $L \times L$ single spin updates. The number of MC sweeps performed between parameter updates is here referred to as the parameter-updating period.

Whereas updating the parameter to a neighboring value with the Metropolis algorithm should be considered the easiest to implement, we remark that, as spins can be updated by a number of methods such as the heat bath method, other schemes of updating the parameters can be employed [20]. There also exists a temperature updating scheme for ST by Langevin algorithm [21].

Table 3.1 summarizes the conditions of the present simulations. For $L = 80$, instead of a single 4000000000 MC sweep production run, four 1000000000 MC sweep runs were performed. This was just to make one trajectory shorter and easier to deal with numerically. Similarly, two production runs (instead of a single run) were made for $L = 30$ and 160.

As for spin-updates, we employed the single spin update algorithm; we updated spins one by one with the Metropolis criteria. As for quasi-random-number generator, we used the Mersenne Twister [22].

Table 3.1: Conditions of the two-dimensional ST simulations.

Lattice size L	2, 4, 8, 10, 20	30	80	160
Number of production runs	1	2	4	2
Total MC sweeps per run	42000000	42000000	1000000000	321300000
Parameter-updating period	50	20	10	5
T_1–T_{N_T}	1.0–5.0	1.0–5.0	1.0–5.0	1.0–3.6
h_1–h_{N_h}	-1.5–1.5	-1.5–1.5	-1.5–1.5	-0.5–0.5
N_T	20	20	70	63
N_h	21	21	51	51
N_{data}[a]	10	10	100	50

[a]The data were stored every N_{data} MC sweeps.

3.2.3 Free energy calculations

The simulated tempering parameters, or free energy in Eqs. (3.13) and (3.17) can be simply obtained by the reweighting techniques applied to the results of preliminary simulation runs [23, 18, 17, 16]. We employed two reweighting methods for this free energy calculation. One method is the multiple-histogram reweighting method, or Weighted Histogram Analysis Method (WHAM) [24, 25] and the other is Multistate Bennett Acceptance Ratio estimator (MBAR) [26], which is based on WHAM.

The equations of WHAM algorithm that were applied to the simulation results are as follows. For details, the reader is referred to Refs. [25, 17]. The density of states (DOS) $n(E, M)$ and free energy values $f(T_i, h_j)$ can be obtained by

$$n(E,M) = \frac{\sum_{T_i,h_j} n_{T_i,h_j}(E,M)}{\sum_{T_i,h_j} N_{T_i,h_j} \exp(f(T_i,h_j) - (E - h_j M)/T_i)}, \tag{3.21}$$

$$f(T_i,h_j) = -\log \sum_{E,M} n(E,M) \exp(-(E - h_j M)/T_i), \tag{3.22}$$

where $n_{T_i,h_j}(E, M)$ is the histogram of E and M at T_i and h_j, and N_{T_i,h_j} is the total number of samples obtained at T_i and h_j. By solving these two equations

self-consistently by iterations, we can obtain $n(E, M)$ and $f(T_i, h_j)$. The obtained $n(E, M)$ allows one to calculate any thermal average at arbitrary temperature and external field values. Note that $f(T_i, h_j)$ is determined up to a constant, which sets the zero point of free energy. Accordingly, $n(E, M)$ is determined up to a normalization constant.

The MBAR is based on the following equations. Namely, by combing Eqs. (3.21) and (3.22), the free energy can be written as

$$f(T_i, h_j) = -\log \sum_{n=1}^{N} \frac{\exp(-(E_n - h_j M_n)/T_i)}{\sum_{k=1}^{N_T} \sum_{l=1}^{N_h} N_{T_k,h_l} \exp(f(T_k, h_l) - (E_n - h_l M_n)/T_k)}, \tag{3.23}$$

where N, N_{T_k,h_l}, E_n, and M_n is the total number of data, the number of samples associated with T_k and h_l, energy of the n-th data, and magnetization of the n-th data, respectively. This equation should be solved self-consistently for $f(T_i, h_j)$. Note that, as in WHAM, $f(T_i, h_j)$ is determined up to a constant.

We repeat the preliminary STM simulations and free energy calculations until we finally obtain sufficiently accurate free energy values which let the system perform a random walk in the temperature and external field space during the STM simulation. We then perform a single, final production run.

Note that these two reweighting methods enable us to obtain not only dimensionless free energy values but also physical values at any temperature and at any external field. It is given by

$$\langle A \rangle_{T,h} = \sum_{n=1}^{N} W_{na} A(x_n), \tag{3.24}$$

$$W_{na} = \frac{1}{\langle c_a \rangle} \frac{\exp(-(E_n - hM_n)/T)}{\sum_{k=1}^{N_T} \sum_{l=1}^{N_h} N_{T_k,h_l} \exp(f(T_k, h_l) - (E_n - h_l M_n)/T_k)}, \tag{3.25}$$

$$\langle c_a \rangle = \sum_{n=1}^{N} \frac{\exp(-(E_n - hM_n)/T)}{\sum_{k=1}^{N_T} \sum_{l=1}^{N_h} N_{T_k,h_l} \exp(f(T_k, h_l) - (E_n - h_l M_n)/T_k)}. \tag{3.26}$$

For details, the reader is referred to Refs. [26, 27].

We also used another method of calculating free energy. By substituting $a(T,h)$ in Eq. (3.16) by the estimates for free energy $\tilde{f}(T,h)$, we obtain

$$P(T,h) \propto e^{-f(T,h)+\tilde{f}(T,h)}. \tag{3.27}$$

From this we can write

$$f(T,h) = \tilde{f}(T,h) - \log P(T,h) + \text{const.} \tag{3.28}$$

Here, $P(T,h)$ can be obtained as the number of samples at each set of parameter values in a preliminary STM simulation. Thus, this equation enables one to refine the free energy much more easily than the reweighting methods, because the method does not require any iterations. This method does not work well, however, when $P(T_i,h_j)$ is too small (or $\tilde{f}(T_i,h_j)$ is too far away from true values) to obtain samples at (T_i,h_j), while the reweighting techniques are still able to work. In the present work, we first used the reweighting methods to obtain rough estimates of the free energy for the entire parameter space. We then used the combination of the reweighting methods and Eq. (3.28) for further refinements of the free energy.

Note that the WHAM gives another piece of information, namely DOS, which MBAR cannot directly calculate. However, the WHAM requires to make histograms before iterations and two kinds of calculations in an iteration step. As the system size grows, the number of possible states increases. Thus, the calculation of DOS can be quite time-consuming. On the other hand, MBAR can be used without making histograms and one MBAR iteration step needs one equation. The length of one iteration, which is approximately proportional to the number of samples and parameter values, increases and can be time-consuming, as the system size is enlarged. However, we have an impression that the MBAR is less time-consuming and more easily implemented than the WHAM. The parallelization of MBAR is slightly easier than that of WHAM and we actually did it with OpenMP.

3.2.4 Temperature and external field distributions

As is mentioned in the previous subsections, we have to give the set of temperature and external field values before ST or STM simulations. Actually the determination involves trial and error. However, still the reweighting methods help one to do this to a certain extent.

Firstly the maximum and minimum values of temperature and external field were chosen so that the area of temperature and external field were wide enough to investigate the critical behaviors. This should be done separately for each system and what is to be investigated.

The distribution of temperature was chosen to be proportional to an exponential to the index number in small lattice sizes, as is common in simulated tempering and replica-exchange methods. However, in large lattice size systems, we assigned more number of values around T_c by hand. A denser distribution is required where the heat capacity is large or the phase transition occurs. The distribution of external field was similarly assigned. In small lattice size it was proportional to the index of external field. However, in the larger lattice size, we assigned more points around $h = 0$, in which the phase transition occurs. We assigned them in such a manner that the acceptance rate of ST parameter updates are preferably between 10% and 50%. This fuzzy criterion is partly due to the two-dimensional distributions. A temperature distribution at a certain external field does not always give the same acceptance rates under another external field.

When the distributions of T_i and h_j turned out to be improper, we reassigned the distributions. In this case, we already had the samples and free energy estimates at a previous distribution, with which the reweighting method lets one to estimate the free energy at the newly distributed values. Consequently, we did not have to start over the free energy calculations from the beginning. We actually repeated this parameter redistribution procedures several times, especially in large lattice size simulations.

3.3 Results and discussion

3.3.1 Simulated Tempering and Magnetizing simulations

Firstly we shall show that the two-dimensional ST simulations were carried out properly. Figures 3.1 and 3.2 show temperature and external field, respectively, as functions of MC sweep. Both were obtained from the simulations in which the linear lattice size was 80. The temperature and external field indeed realized random walks.

Figures 3.3 and 3.4 show energy and magnetization per spin, respectively, as functions of MC sweep. They also realized random walks. Note that there are expected correlations between the temperature and energy (see Figs. 3.1 and 3.3) and between the external field and magnetization (see Figs. 3.2 and 3.4). The same behavior was observed in other lattice size simulations (data not shown).

Figure 3.5 shows the dimensionless free energy per spin as a function of temperature and external field, which was obtained by applying MBAR to the results of the production runs. Note that the partial differential of this free energy by h gives $\frac{\langle m \rangle}{T}$. The shape at $h = 0$ suggests a jump of m below T_{c}, indicating existence of the first-order phase transitions.

Figure 3.6 shows the distribution of magnetization as a function of temperature. Below T_{c} the distribution is separated into two parts. As temperature increases, the distribution becomes broader. Near T_{c} the distribution is the broadest and two peaks merge. It then becomes narrower. Note that this figure was obtained by only four production runs (see Table 3.1), and can be obtained even by only one production run, though the error is expected to become larger. Figures 3.7(a), 3.7(b), and 3.7(c) show the distribution of magnetization as a function of external field above, around, and below T_{c}, respectively. Above T_{c}, the change is smooth and continuous (see Fig. 3.7(a)). Around T_{c}, the distribution becomes very wide around $h = 0$ (see Fig. 3.7(b)). This is one of the properties of the second-order phase transitions. Below T_{c}, the distribution jumps from one side to the other side at $h = 0$ (see Fig. 3.7(c)). This abrupt jump of distribution is one of the properties of the first-order phase transitions.

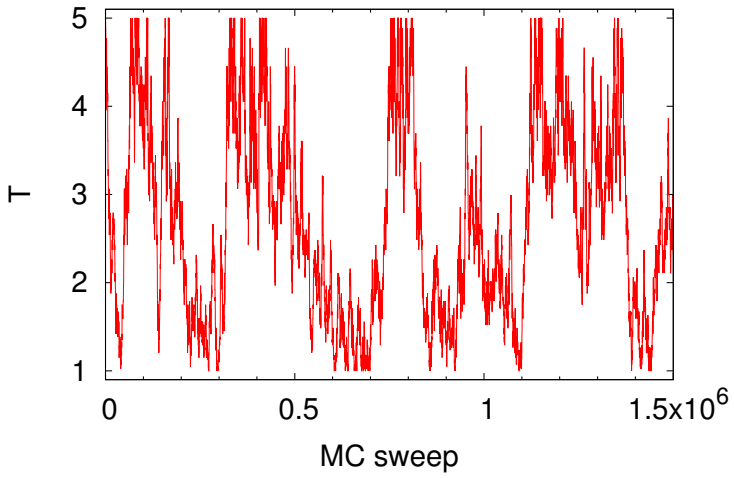

Figure 3.1: The history of temperature T. The linear lattice size L is 80.

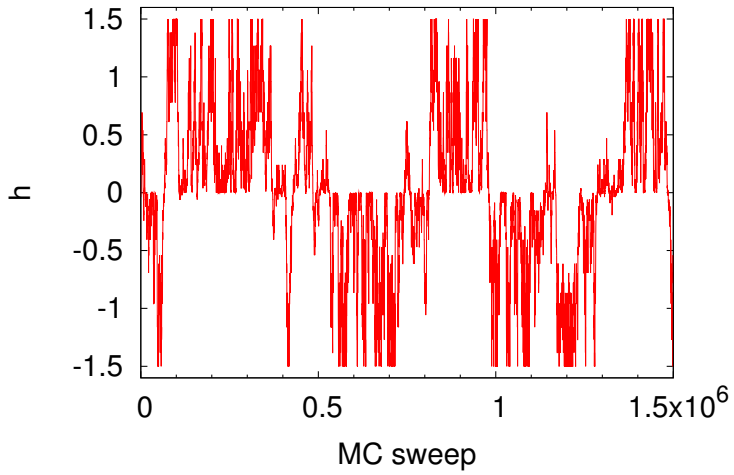

Figure 3.2: The history of external field h. The linear lattice size L is 80.

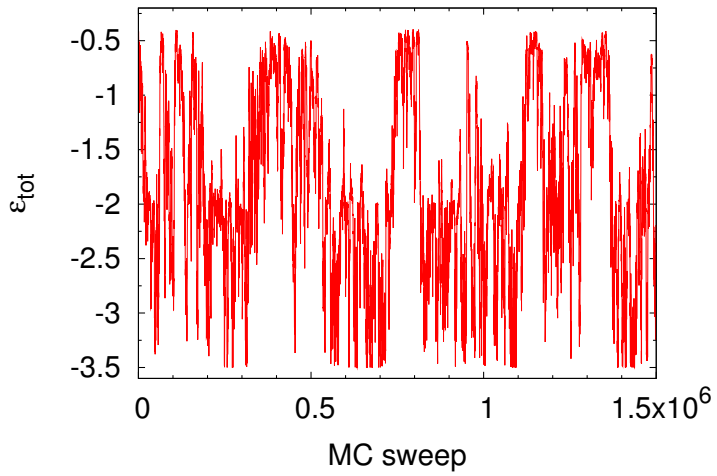

Figure 3.3: The history of total energy per spin, $\epsilon_{\rm tot}$. The linear lattice size L is 80.

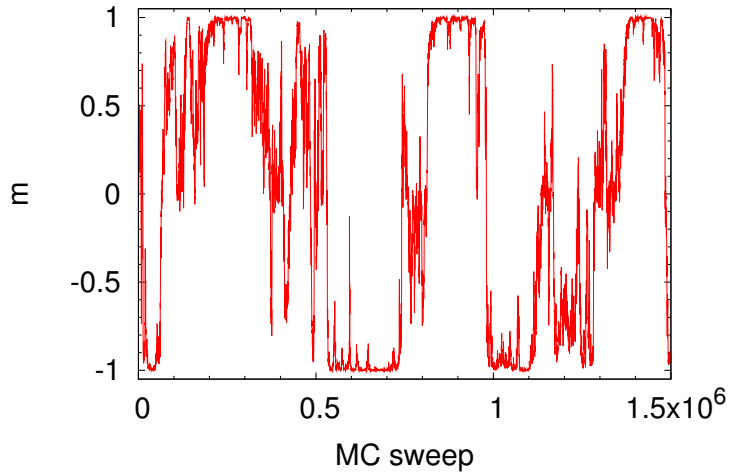

Figure 3.4: The history of the magnetization per spin, m ($\equiv M/L^2$). The linear lattice size L is 80.

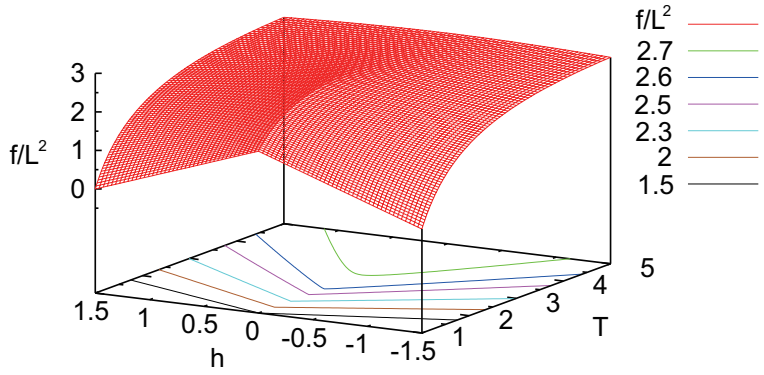

Figure 3.5: The free energy per spin f/L^2 and its contour curves as a function of T and h.The linear lattice size L is 80.

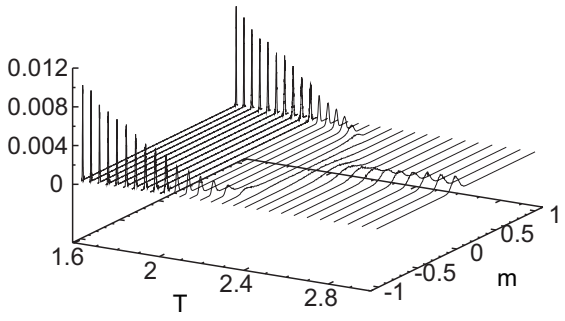

Figure 3.6: The distribution of m as a function of T for $h = 0$. The linear lattice size L is 80.

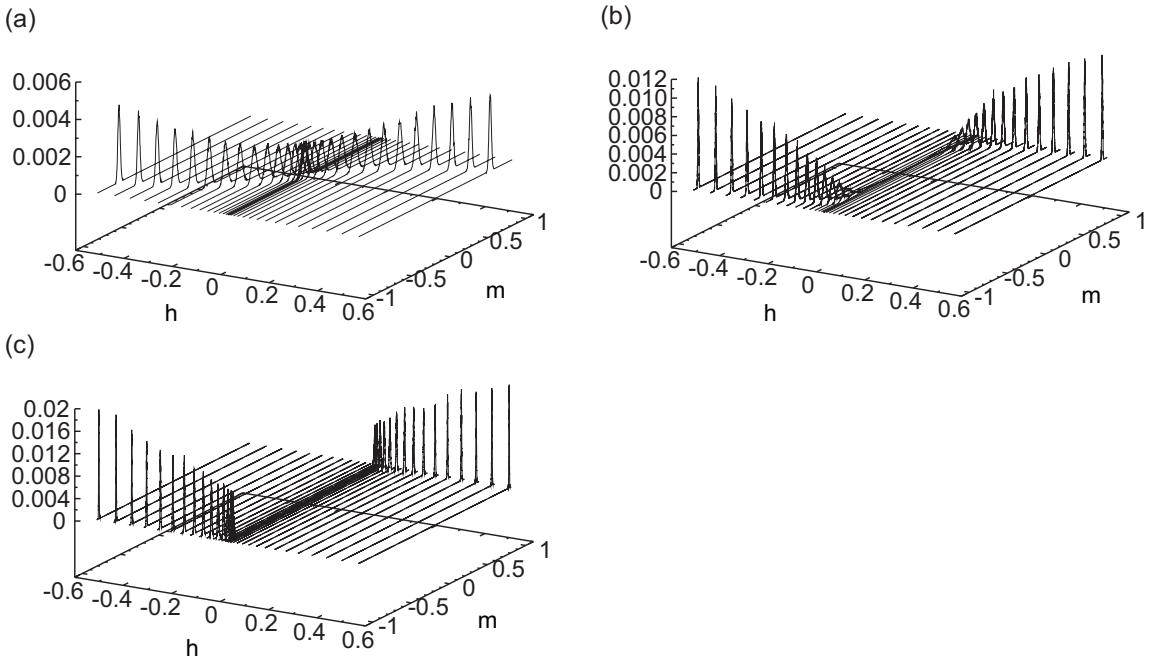

Figure 3.7: The distribution of m as a function of h when (a) $T = 3.21$, (b) $T = 2.316$ and (c) $T = 1.967$. The linear lattice size L is 80.

We also calculated the Binder cumulant [28] defined by

$$U(T,h,L) \equiv \frac{1}{2}\left(3 - \frac{\langle m^4 \rangle}{\langle m^2 \rangle^2}\right). \tag{3.29}$$

Figure 3.8 shows the Binder cumulant as a function of temperature. As is well-known, the graphs cross at one point at T_c. The error bars were obtained by the jackknife method [29, 30].

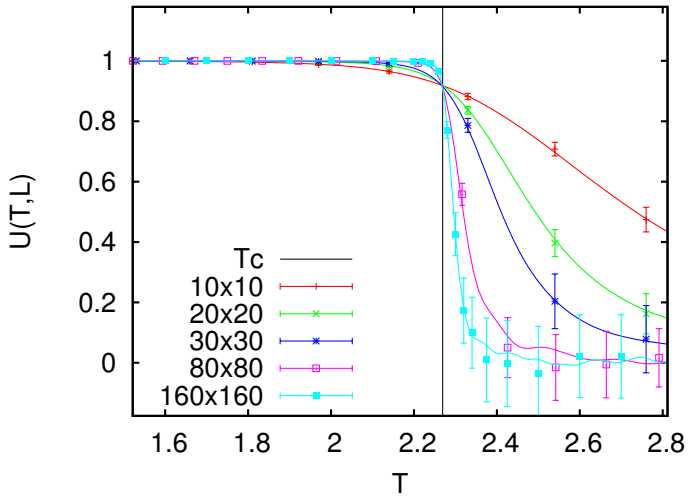

Figure 3.8: Binder cumulant U vs temperature.

Figure 3.9 shows the Binder cumulant as a function of temperature under different external fields. The graphs do not cross at one point in the presence of finite external field. The amount of errors is expected to be on the same level of Fig. 3.8 and the error bars are suppressed here to aid the eye.

3.3.2 Comparison of simulated tempering with simulated tempering and magnetizing

We compared the results of the STM method with those of the conventional ST method. Figures 3.10 and 3.11 show the magnetization as a function of tempera-

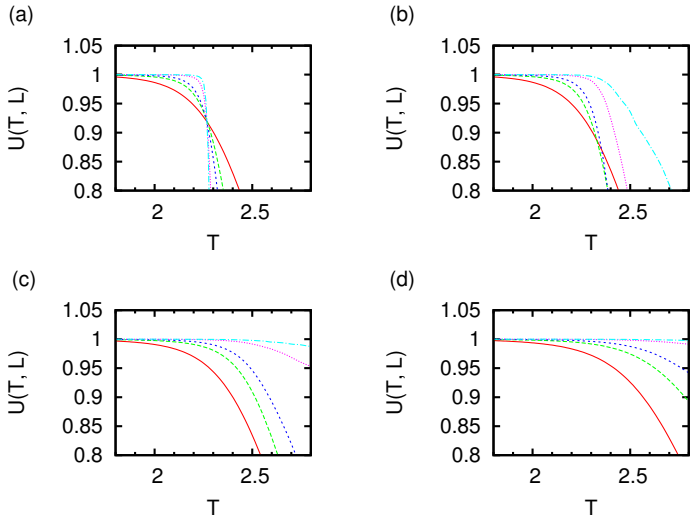

Figure 3.9: Binder cumulant U vs temperature under different external fields. (a) $h = 0$. (b) $h = 0.01$. (c) $h = 0.05$. (d) $h = 0.1$. Red solid, dashed green, short dashed dark blue, dotted purple, and chain light blue lines stand for $L = 10$, 20, 30, 80, and 160, respectively.

ture and external field, which was calculated using MBAR with the data obtained by the conventional ST and STM simulation, respectively. Figure 3.10 obtained by the conventional ST shows artifact jumps at a high temperature and a certain external field. This must have been caused by a failure of sampling some parts of states. On the other hand, the results by the STM simulations are smooth (see Fig. 3.11). Figure 3.12 shows the density of states obtained by conventional ST and STM simulations. This obviously illustrates that the area in which the energy is relatively high with somewhat strong magnetizations were not sampled by the conventional ST method. These results imply that the dimensional extension in the STM enlarged the sampled space.

Once one succeeds in estimating the free energy values, or ST and STM parameters $a(T_i)$ and $a(T_i, h_j)$, with sufficient accuracy, one can perform ST and STM simulations properly. However, the computational efforts in free energy calculations are still much larger for STM than for ST. Therefore, it is desirable to develop an even more efficient method for the STM free energy estimation than

the present one.

3.3.3 Simulated magnetizing

We study the compatibility of ST with the first-order phase transition along external field changes, by performing "Simulated Magnetizing" (SM) simulations, in which the temperature is fixed and the external field is updated by the Metropolis criteria. Figure 3.13 shows the external field as a function of MC sweep in the SM simulations below T_c. We performed SM simulations in a number of lattice sizes from 2×2 to 20×20. These graphs illustrate the fact that as the system size becomes larger, the difficulty in simulations grows. In fact it finally became impossible to observe the events in which the magnetization goes to the other side across the zero point (see Fig. 3.14(a)), while it was still possible above T_c (see Fig. 3.14(b)). These results imply that the full range random walk happens above T_c but not below T_c. Therefore, this result suggests that the random walk of temperature is crucial for the full range random walk of external field. The full range random walk of the external field happens in the STM simulation when the temperature was high above T_c. Note that the Ising model is equivalent to the lattice gas model [31]. Hence, what happened in STM simulations can be understood as that even though the phase transitions between gas and liquid do not directly occur, they do occur through the "super critical water region."

To explore this phenomenon more clearly, readers are referred to a supplementary material [32], which shows how the temperature and external field changed during the STM simulation.

3.3.4 How often temperature or external field should be updated?

A common question about this kind of simulation is how frequently the parameter-updating attempts should be made. We want to emphasize that as long as the detailed balance condition is satisfied the simulations should be correctly carried out.

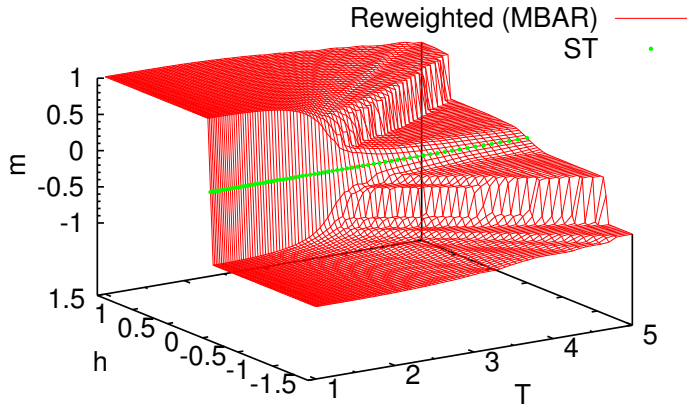

Figure 3.10: Reweighted data (red) and original data (green) obtained by the conventional ST. The linear lattice size L is 80.

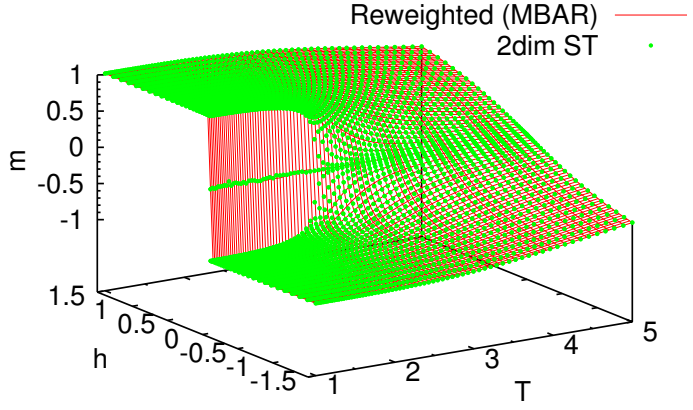

Figure 3.11: Reweighted data (red) and original data (green) obtained by the STM simulations. The linear lattice size L is 80.

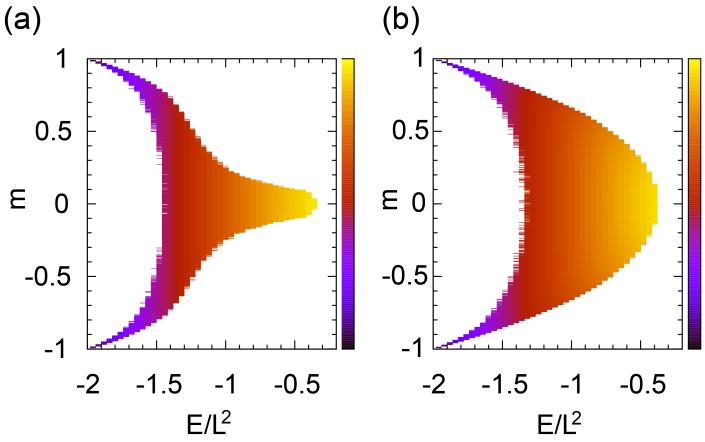

Figure 3.12: Calculated DOS obtained by WHAM with (a) ST and (b) STM data. The linear lattice size L is 80.

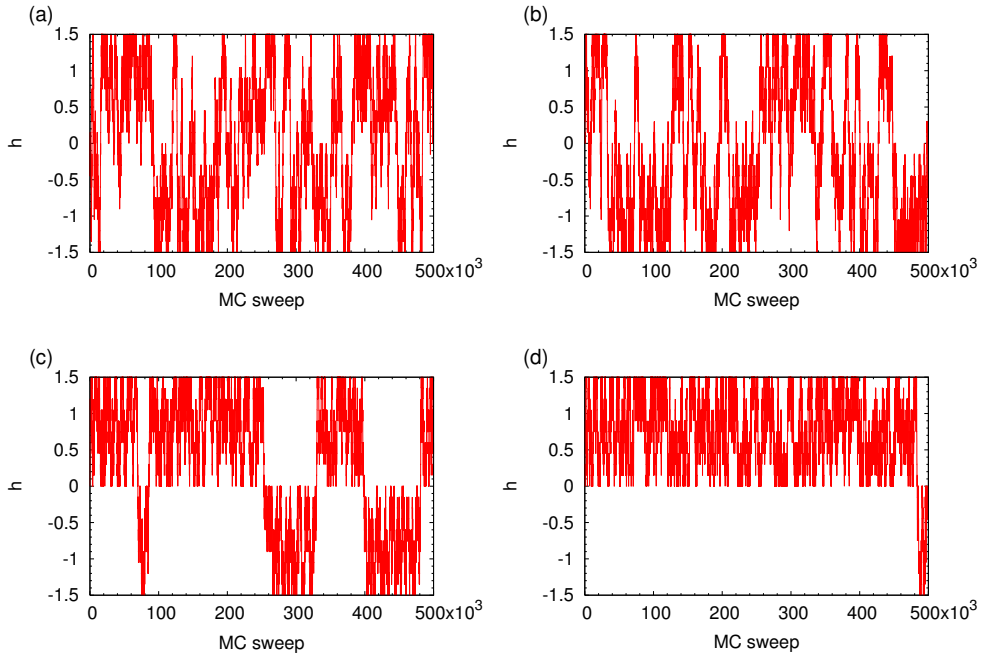

Figure 3.13: External field vs MC sweep in SM simulations under T_c ($T = 1.97$). The linear lattice size L is (a) 2, (b) 4, (c) 8, and (d) 10, respectively.

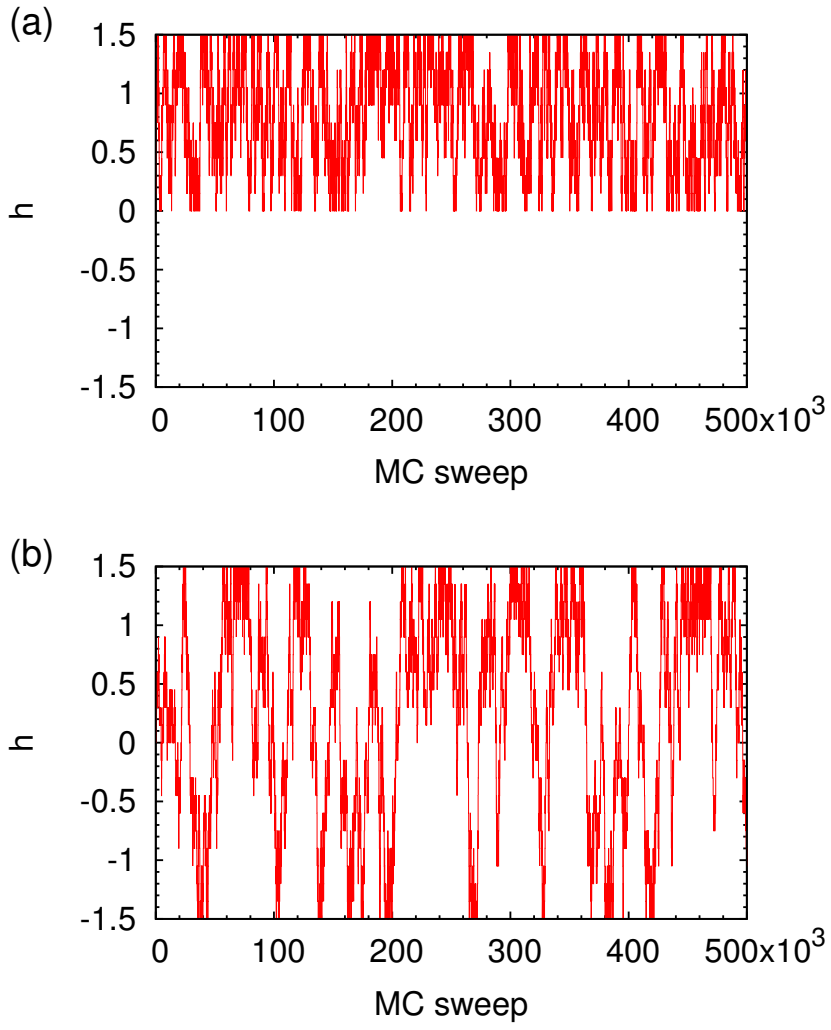

Figure 3.14: External field and MC sweep in the SM simulation (a) under T_c ($T = 1.97$) and (b) above T_c ($T = 3.88$). The linear lattice size L is 20.

We compared STM simulations performed with different parameter-updating frequencies. Figure 3.15 shows the results of the heat capacity as a function of temperature at $h = 0$, which were obtained by the STM method with different conditions. The conditions are one parameter-updating attempt every one, two, twenty, and a hundred MC sweeps. They show good agreement with each other. The error bars were obtained by the jackknife method [29, 30]. Note that the error bars tend to be larger as the parameter-updating frequency becomes less.

Figure 3.16 shows the magnetization as a function of temperature at $h = 0$. Data were obtained with several parameter-updating frequencies, such as one parameter-updating attempt every one, twenty, and a hundred MC sweeps. They also agree with each other. Note that because finite sizes are employed, the magnetization under T_c at $h = 0$ is also zero. With the lower parameter-updating frequency, the convergence was not so good and the error bars tend to be larger. The error bars were obtained by the jackknife method [29, 30]. These results suggest that the frequent parameter update does not make any artifacts and that it should be recommended.

Figure 3.17 shows the integrated correlation time of magnetization obtained at different parameter-updating frequencies. The height of data is expected to converge to the integrated correlation time between samples. This was calculated by using the jackknife method with different bin sizes [29, 30]. Data were stored every ten MC sweeps. Thus, the correlation time measured by MC sweep should be ten times larger. The error bars were obtained with the χ^2 distribution. These results suggest that the higher the parameter-updating frequency, the shorter the correlation time. Therefore, frequent parameter updates are preferred. Note that the observation that the frequent parameter updates are preferable is in accord with the statement that frequent replica-exchanging attempts are recommended [34, 35].

3.3.5 Observation of crossover

We study the crossover behavior of the phase transitions. We calculated the magnetization by MBAR around the critical point.

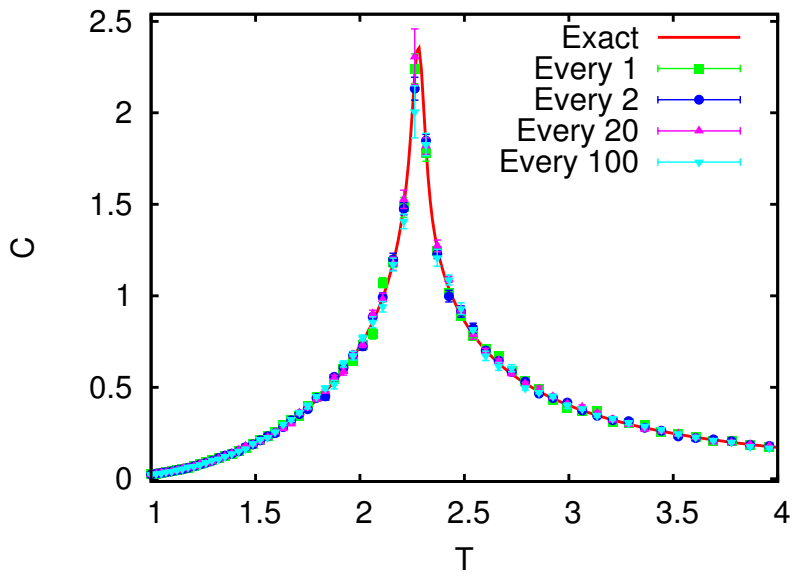

Figure 3.15: Heat capacity per spin, C, at $h = 0$. The linear lattice size L is 80. As the legends shown in the figure, green square, blue circle, purple triangle, and light-blue inverse-triangle represent that one parameter-updating attempt is made every one, two, twenty, and a hundred MC sweeps, respectively. The exact result (red solid line) was obtained by Berg's program [30] based on Ref. [33].

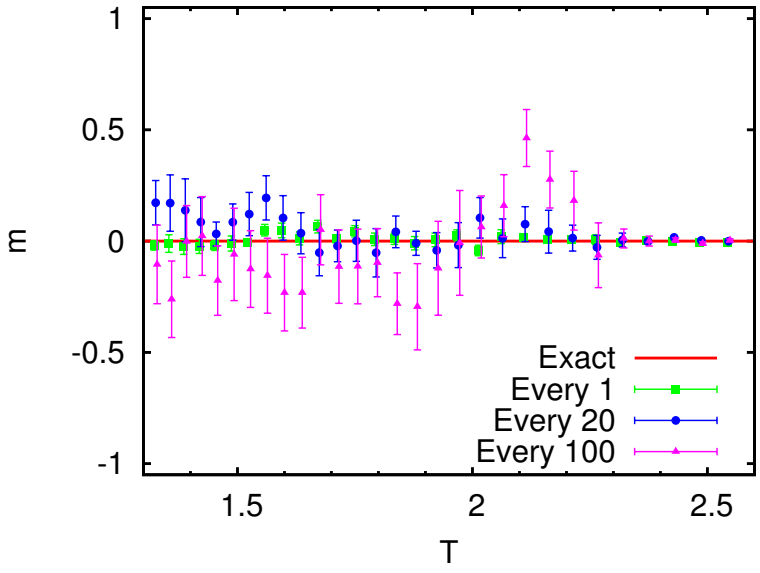

Figure 3.16: Magnetization per spin m when $h = 0$. As the legends shown in the picture, the green square, blue circle and purple triangle represent that one parameter-updating attempt is made every one, twenty, and a hundred MC sweeps, respectively. Some error bars were slightly shifted horizontally to aid the eye.

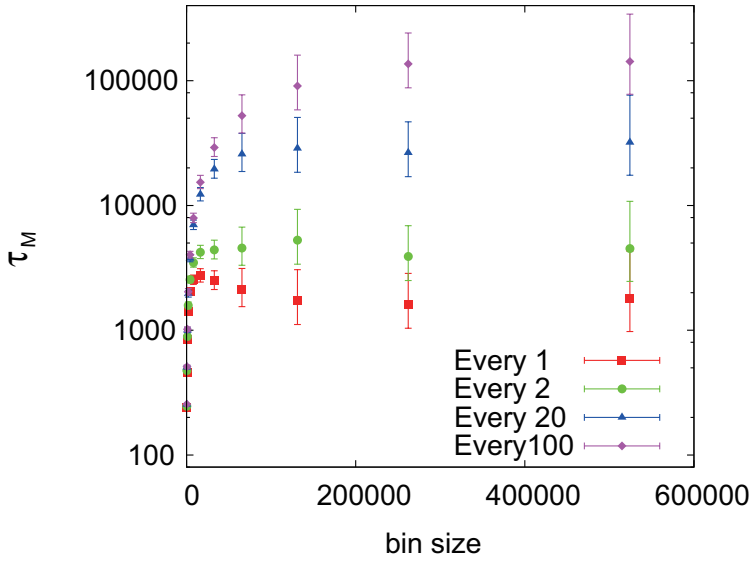

Figure 3.17: Correlation time analysis. Error bars show the 95% confident interval.

We employ the finite-size scaling approach, which is discussed in Ref. [36]. The scaling form of magnetization m with respect to temperature and external field is given by

$$mL^{\beta/\nu} = \Psi(L^{1/\nu}t, L^{(\gamma+\beta)/\nu}h)\,, \tag{3.30}$$

where $t = |T - T_c|/T_c$ and L is the linear size of lattice. The Greek letters ν and γ stand for critical exponents. In the two-dimensional Ising model, $\beta = 1/8$, $\delta = 15$, $\nu = 1$, and $\gamma = 7/4$.

Firstly we examine the scaling behavior of the magnetization. Figures 3.18 and 3.19 show the magnetization as functions of T and h, respectively, and we see that it obeys the critical behavior of $m \sim |T - T_c|^\beta$ and $m \sim |h|^{1/\delta}$, respectively. According to the scaling approach, when Lt or $L^{15/8}h$ is large enough, then the finite effect can be negligible. In this case, Figs. 3.18 and 3.19 imply that those conditions are given by $Lt > 0.2$ and $L^{15/8}h > 1.1$, respectively.

We now study the behavior under the conditions slightly different from the

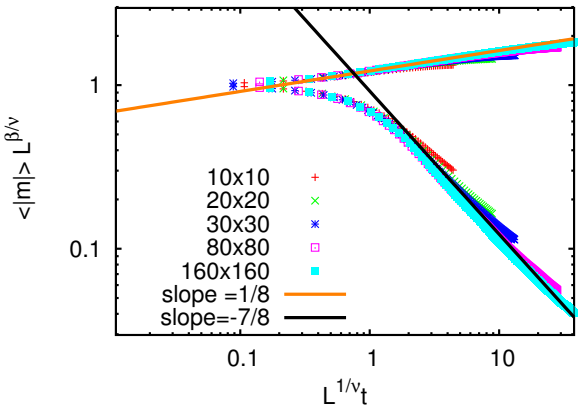

Figure 3.18: Scaled m when $h = 0$. The lines are the same as used in Ref. [36].

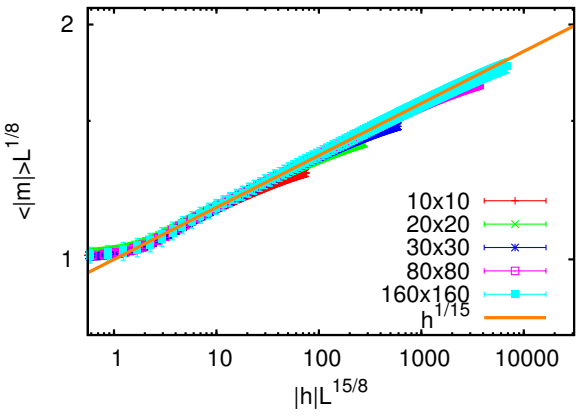

Figure 3.19: Scaled m at $T = T_c$.

critical point. Figure 3.20 shows the magnetization as a function of temperature near $h = 0$. As the external field was increased, the behavior was differentiated in the low temperature region. Even in the presence of weak external field, the magnetization obeys $t^{1/8}$ when the temperature was relatively high enough. However, with relatively strong external field, the scaling behavior disappears.

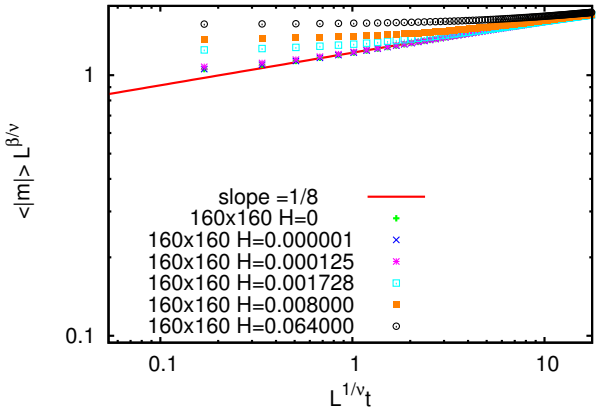

Figure 3.20: Scaled m near $h = 0$.

Figure 3.21 shows the magnetization as a function of external field near $T = T_c$. As the temperature was deviated from T_c, the behavior is differentiated in the weak external field region. Thus, even with slight difference from T_c, the magnetization obeys $h^{1/15}$ when the external field is strong enough.

Figure 3.22 illustrates the comprehensive behavior of $\langle|m|\rangle$ near the critical point. Note that this is a log scale plot. Near the h-axis $\langle|m|\rangle$ obeys $|h|^{1/15}$ and near the T-axis $\langle|m|\rangle$ obeys $|t|^{1/8}$.

Figure 3.23(a) and Figure 3.23(b) show the difference between $\langle|m|\rangle L^{1/8}$ and $1.22(Lt)^{1/8}$ and that between $\langle|m|\rangle L^{1/8}$ and $(L^{15/8}h)^{1/15}$, respectively. These data were obtained by the 160×160 lattice size simulations. Note that the factor 1.22 comes from the exact solution [37, 19]. According to the crossover scaling formalism [38], if $t^{-15/8}h$ is large enough, then the magnetization obeys $m \sim t^{1/8}$, and if $h^{-8/15}t$ is large enough ($t^{-15/8}h$ is small enough), then it obeys $m \sim h^{1/15}$. Figure 3.23(a) shows that if the finite-size effects are negligible ($Lt \gg 0.2$) and

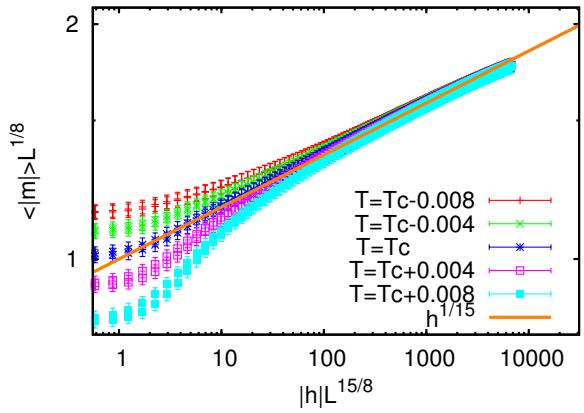

Figure 3.21: Scaled m near $T = T_c$.

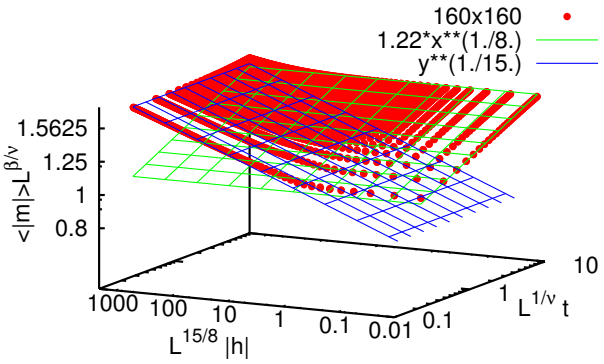

Figure 3.22: Scaled m about the critical point. The linear lattice size L is 160. We only display the results for $T < T_c$.

$t \gg 0.2h^{8/15}$ (i.e., $th^{-8/15}$ is large), then the critical behavior is $m \sim t^{1/8}$. Figure 3.23(b) shows that if finite-size effects are negligible ($L^{15/8}h \gg 0.3$) and $t \ll 0.2h^{8/15}$ (i.e., $t^{-15/8}h$ is large), then the critical behavior is $m \sim h^{1/15}$. Thus, Fig. 3.23 clearly shows that the line ($t = 0.2h^{8/15}$) gives the boarder of the two scaling regimes.

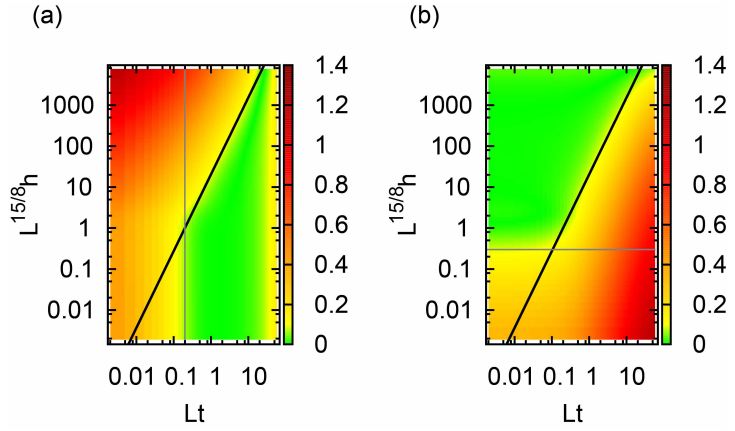

Figure 3.23: Difference between magnetization and its expected scaling behavior about the critical point. The linear lattice size L is 160. (a) $|mL^{1/8} - 1.22(Lt)^{1/8}|$ is illustrated. The black line is $t = 0.2h^{8/15}$. The vertical gray line is $Lt = 0.2$. (b) $|mL^{1/8} - (L^{15/8}h)^{1/15}|$ is illustrated. The black line is $t = 0.2h^{8/15}$. The horizontal gray line is $L^{15/8}h = 0.3$

References

[1] U. H. E. Hansmann and Y. Okamoto: in *Annual Reviews of Computational Physics VI*, edited by Dietrich Stauffer, (World Scientific, Singapore, 1999) pp. 129–157.

[2] A Mitsutake, Y Sugita, and Y Okamoto: *Biopolymers* **60**, 96–123 (2001).

[3] Yuji Sugita and Yuko Okamoto: in *Lecture Notes in Computational Science and Engineering*, edited by T. Schlick and H. H. (Gan Springer, 2002) pp. 304–332; `http://arxiv.org/abs/cond-mat/0102296`

[4] B. A. Berg and T. Neuhaus: *Physics Letters B* **267**, 249–253 (1991).

[5] B. A. Berg and T, Neuhaus: *Physical Review Letters* **68**, 9–12 (1992).

[6] A. P. Lyubartsev, A. A. Martsinovski, S. V. Shevkunov, and P. N. Vorontsov-Velyaminov: *The Journal of Chemical Physics* **96** 1776–1783 (1992).

[7] E. Marinari and G. Parisi: *Europhysics Letters (EPL)* **19**, 451–458 (1992).

[8] K. Hukushima and K. Nemoto: *Journal of the Physics Society Japan* **65**, 1604–1608 (1996).

[9] C. J. Geyer: in *Computing Science and Statistics, Proceedings of the 23rd Symposium on the Interface*, edited by E. M. Keramidas (Interface Foundation of North America, 1991) pp. 156–163.

[10] F. Wang and D. P. Landau: *Physical Review Letters* **86**, 2050–2053 (2001).

[11] F. Wang and D. P. Landau: *Physical Review E* **64**, 056101 (16 pages) (2001).

[12] A. Laio and M. Parrinello: *Proc. Natl. Acad. Sci. USA* **99**, 12562–12566 (2002).

[13] R. H. Swendsen and J.-S. Wang: *Physical Review Letters* **57**, 2607–2609 (1986).

[14] Y. Iba: *International Journal of Modern Physics C* **12**, 623–656 (2001).

[15] J. Kim and J. E. Straub: *The Journal of Chemical Physics* **133**, 154101 (12 pages) (2010).

[16] A. Mitsutake and Y. Okamoto: *Physical Review E* **79**, 047701 (4 pages) (2009).

[17] A. Mitsutake and Y. Okamoto: *The Journal of Chemical Physics* **130**, 214105 (14 pages) (2009).

[18] A. Mitsutake: *The Journal of Chemical Physics* **131**, 094105 (15 pages) (2009).

[19] D. S. Gaunt and C. Domb: *Journal of Physics C: Solid State Physics* **3**, 1442–1461 (1970).

[20] J. D. Chodera and M. R. Shirts: *The Journal of Chemical Physics* **135**, 194110 (15 pages) (2011).

[21] C. Zhang and J. Ma: *The Journal of Chemical Physics* **132**, 244101 (16 pages) (2010).

[22] M. Matsumoto and T. Nishimura: *ACM Transactions on Modeling and Computer Simulation (TOMACS)* **8**, 3–30 (1998).

[23] A. Mitsutake and Y. Okamoto: *Chemical Physics Letters* **332**, 131–138 (2000).

[24] A. Ferrenberg and R. Swendsen: *Physical Review Letters* **63**, 1195–1198 (1989).

[25] S. Kumar, J. M. Rosenberg, D. Bouzida, R. H. Swendsen, and P. A. Kollman. *Journal of Computational Chemistry* **13**, 1011–1021 (1992).

[26] M. R. Shirts and J. D. Chodera: *The Journal of Chemical Physics* **129**, 124105 (10 pages) (2008).

[27] A. Mitsutake, Y. Sugita, and Y. Okamoto: *The Journal of Chemical Physics* **118**, 6664 (12 pages) (2003).

[28] K. Binder: *Zeitschrift für Physik B Condensed Matter* **43**, 119–140 (1981).

[29] R. G. Miller: *Biometrika* **61**, 1–15, (1974).

[30] B. A Berg: *Markov Chain Monte Carlo Simulations and Their Statistical Analysis* (World Scientific, Singapore, 2004); http://www.worldscibooks.com/physics/5602.html

[31] T. D. Lee and C. N. Yang: *Physical Review*, **87**, 410–419 (1952).

[32] See Supplemental Material at http://www.tb.phys.nagoya-u.ac.jp/~tnagai/published/guide.html or http://link.aps.org/supplemental/10.1103/PhysRevE.86.056705 for looking into the behavior of T and h during the STM simulation.

[33] A. E. Ferdinand and M. E. Fisher: *Phys. Rev.* **185**, 832–846 (1969).

[34] D. J. Sindhikara, Y. Meng, and A. E. Roitberg: *The Journal of Chemical Physics* **128**, 024103 (10 pages) (2008).

[35] D. J. Sindhikara, D. J. Emerson, and A. E. Roitberg: *Journal of Chemical Theory and Computation* **6**, 2804–2808 (2010).

[36] D. P. Landau: *Physical Review B* **13**, 2997–3011 (1976).

[37] C. N. Yang: *Physical Review* **85**, 808–816 (1952).

[38] M. E. Fisher: *Reviews of Modern Physics* **46**, 597–616 (1974).

Chapter 4

Simulated Tempering and Magnetizing Simulations of a Potts Model

T. Nagai, Y. Okamoto, and W. Janke: "Application of simulated tempering and magnetizing to two-dimensional Potts model," *Journal of Statistical Mechanics: Theory and Experiment* **2013**, P02039 (21 pages) (2013); arXiv:1212.3084.

4.1 Introduction

Monte Carlo (MC) and molecular dynamics simulations have been demonstrated to be indispensable tools for studying the statistical properties of various physical systems in equilibrium. The quasi-ergodicity problem, however, where the system gets trapped in states of energy local-minimum, has often posed great difficulties. In order to overcome the difficulty, generalized-ensemble algorithms have been developed and applied to many problems in spin models and biomolecular systems (for reviews, see, e.g., Refs. [1, 2, 3]).

Well-known examples of generalized-ensemble algorithms are the multicanonical algorithm (MUCA) [4, 5], simulated tempering (ST) method [6, 7], and replica-exchange method (REM) [8, 9] (REM is also referred to as parallel tempering). Closely related to MUCA are the Wang-Landau method [10, 11] and metadynamics [12]. Also closely related to REM is the method in Ref. [13].

On the basis of the recent multi-dimensional generalizations of the generalized-ensemble algorithms [14, 15, 16], the "simulated tempering and magnetizing" (STM) method has been proposed and developed [17, 18]. In the Refs. [17, 18] the classical Ising model was studied, being introduced the external (magnetic) field as a second dynamical variable besides the temperature. The improvements over the conventional "one-dimensional" simulated tempering schemes was shown, such as better sampling efficiency and potential applicability to the first-order phase transition which cannot be dealt with by one-dimensional ST.

In the present work, we further investigate the STM method, applying it to the two-dimensional three-state Potts model [19, 20]. We see the scheme working in this complicated system. We also look into crossover behaviors according to lattice size L as well as T and h.

This chapter is organized as follows. In chapter 4.2 we review the STM method and give the details of our simulations. In chapter 4.3 we present the results. After checking the two-dimensional random walks, we compare ST and STM, and calculate various thermal quantities at many sets of parameter values.

4.2 Model and methods

4.2.1 Model

We study the two-dimensional three-state standard Potts model in external field with energy:

$$H = E - hM\,, \tag{4.1}$$

$$E = -\sum_{\langle i,j\rangle} \delta_{\sigma_i,\sigma_j}\,, \tag{4.2}$$

$$M = \sum_{i=1}^{N} \delta_{0,\sigma_i}\,, \tag{4.3}$$

where $N = L^2$ denotes total number of spins, δ is Kronecker delta function, σ_i a spin at the ith site, and h the external field. The spin σ_i takes on one of the three values 0, 1, or 2. The sum in Eq. (4.2) goes over all the nearest-neighbor pairs, with the spins σ_i arranged on the sites of square $L\times L$ lattice with periodic boundary conditions. Data were obtained by means of STM for lattice sizes ranging from 2×2 to 160×160 and additionally with conventional canonical simulations on 320×320 and 640×640 lattices. Note that because of correspondence between three-dimensional three-state Potts model and QCD theory, there are a number of studies in three-state Potts model, especially in three-dimensions [21, 22, 23, 24].

We recall that the three-state (standard) Potts model is equivalent to the three-state planer Potts or Z_3 model:

$$H = E - hM\,, \tag{4.4}$$

$$E = -\frac{2}{3}\sum_{\langle i,j\rangle} \cos\theta_{ij}\,, \tag{4.5}$$

$$M = \frac{2}{3}\sum_{i=1}^{N} \cos\theta_i\,, \tag{4.6}$$

where $\theta_{ij} = \theta_j - \theta_i$ and $\theta_i = \frac{2\pi}{3}\sigma_i$.

As one can see from Eqs. (4.1) and (4.3) [or Eqs. (4.4) and (4.6)], spin direc-

tion 0 is favored by the positive external field ($h > 0$). Accordingly, the negative external field ($h < 0$) disfavors spin direction 0. Thus, the system in presence of the negative external field is expected to behave as two-dimensional Ising model. In the limit $h \to -\infty$, the three-state Potts model is equivalent to the Ising model at the zero external field, because the unfavored states disappear from the partition function. Figure 4.1 illustrates the schematic picture of this relation.

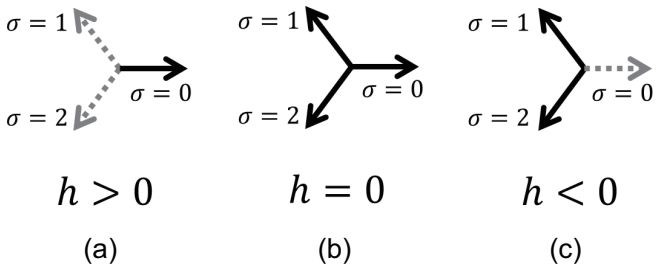

Figure 4.1: Schematic description of behavior of spins according to the external field. (a) spin 0 is favored with $h > 0$, i.e., spin 1 and spin 2 are disfavored. (b) all the three states are equivalent for $h = 0$. (c) spin 0 is disfavored with $h < 0$.

4.2.2 Simulation methods

In this section we briefly review the STM method [17, 18]. While the conventional ST method [6, 7] considers the temperature to be an additional dynamical variable besides spin degrees of freedom, the STM method employs the external field as a second additional dynamical variable besides temperature [17, 18]. This algorithm is thus based on the multi-dimensional extension of generalized-ensemble algorithms [14, 15, 16]. In other words, we consider

$$e^{-(E-hM)/T+a(T,h)} \tag{4.7}$$

as a joint probability for (x, T, h) $(\in X \otimes \{T_1, T_2, \ldots, T_{N_T}\} \otimes \{h_1, h_2, \ldots h_{N_h}\})$, where $a(T, h)$, x, and X are a parameter, the (microscopic) state, and the sampling space.

A suitable candidate for $a(T_i, h_j)$ may be found by looking into the probability of occupying each set of parameter values. It is given by

$$P(T_i, h_j) = \frac{\sum_{k=1}^{N_T}\sum_{l=1}^{N_h}\int dx\, \delta_{ik}\,\delta_{jl}\, e^{-\frac{E(x)-h_l M(x)}{T_k}+a(T_k,h_l)}}{\sum_{k=1}^{N_T}\sum_{l=1}^{N_h}\int dx\, e^{-\frac{E(x)-h_l M(x)}{T_k}+a(T_k,h_l)}} \tag{4.8}$$

$$= \frac{e^{-f(T_i,h_j)+a(T_i,h_j)}}{\sum_{k=1}^{N_T}\sum_{l=1}^{N_h} e^{-f(T_k,h_l)+a(T_k,h_l)}} \tag{4.9}$$

$$\propto e^{-f(T_i,h_j)+a(T_i,h_j)}, \tag{4.10}$$

where

$$e^{-f(T_i,h_j)} = \int dx\, e^{-(E-h_j M)/T_i}. \tag{4.11}$$

Thus, the dimensionless free energy $f(T_i, h_j)$ is a proper selection for $a(T_i, h_j)$ in order to generate a uniform distribution of the number of samples according to T and h. These free energy values can be estimated by a number of methods. For example, one can obtain such values from preliminary simulations and reweighting techniques.

Any thermal average $\langle A\rangle_{T_i,h_j}$ at given T_i ($\in \{T_1, T_2, \ldots, T_{N_T}\}$) and h_j ($\in \{h_1, h_2, \ldots, h_{N_h}\}$) can be obtained by the conditional expectation: $\langle A\rangle_{T_i,h_j} = \left\langle A|T_i, h_j\right\rangle_{\mathrm{ST}}$. Namely, we have

$$\langle A\rangle_{T_i,h_j} = \frac{1}{N_{T_i,h_j}}\sum_{k=1}^{N_{T_i,h_j}} A^k_{T_i,h_j}, \tag{4.12}$$

where N_{T_i,h_j} is the total number of samples at T_i and h_j, and $A^k_{T_i,h_j}$ represents the k-th sample at T_i and h_j.

The temperature T or external field h can be updated similarly to spin σ_i, because they are considered as dynamical variables. The Metropolis criterion for

updating T and h is given by

$$w(T_i, h_j \to T_{i'}, h_{j'}) = \min\left(1, \frac{P(T_{i'}, h_{j'})}{P(T_i, h_j)}\right) \tag{4.13}$$

$$= \min\left(1, \exp\left(-\left(\frac{1}{T_{i'}} - \frac{1}{T_i}\right)E + \left(\frac{h_{j'}}{T_{i'}} - \frac{h_j}{T_i}\right)M + a(T_{i'}, h_{j'}) - a(T_i, h_j)\right)\right). \tag{4.14}$$

Once an initial state is prepared, the STM simulations can be performed by repeating the following two steps. 1. We perform a conventional canonical simulation at fixed T_i and h_j for certain MC sweeps. 2. We update the temperature and/or external field by Eq. (4.14) with $a(T, h) = f(T, h)$.

In our implementation, after a fixed number of MC sweeps, either T or h was updated (the choice between T and h was made at random) by Eq. (4.14) to a neighboring value (the choice between two possible neighbors was also made at random). Here, one MC sweep consists of $L \times L$ single spin updates. The number of MC sweeps performed between parameter updates is here referred to as the parameter-updating period.

We remark that, as spins can be updated by a number of algorithms, other schemes of updating the parameters can be employed [25]. There also exists a temperature updating scheme for ST by Langevin algorithm [26].

Table 4.1 summarizes the conditions of the present STM simulations. According to the previous studies [18, 27, 28], we update the parameters frequently. That is, we employed very small parameter-updating periods.

We have also performed conventional simulations. Table 4.2 lists their details. The temperature was chosen by the extrapolation. We estimated the proper temperature by fitting the STM results to $T_{\max} - T_c \propto L^{-1/\nu}$, where $T_{\max}$ is the temperatures at which the observables take their maxima. The Greek letter ν denotes the correlation length critical exponent. We fit to the Potts case ($\nu = 5/6$) and to the Ising case ($\nu = 1$) the data without the external field and the data in the external field, respectively.

Table 4.1: Conditions of the two-dimensional ST simulations.

Lattice size L	5	10	20	40	80	160
Total MC sweeps	220915510	216277330	164000000	164000000	436050000	525000000
Parameter-updating period	1	1	1	1	1	1
T_1–T_{N_T}	0.1–3.5	0.1–3.5	0.3–3.2	0.3–3.2	0.5–2.0	0.5–2.0
h_1–h_{N_h}	-1.5–1.5	-1.5–1.5	-1.5–1.5	-1.5–1.5	-1.5–1.5	-1.0 – 0.025
N_T	20	20	40	40	76	95
N_h	21	21	41	41	5 1	30
N_{data} [a]	10	10	10	10	10	10

[a]The data were stored every N_{data} MC sweeps.

Table 4.2: Conditions of the regular simulations.

Lattice size L	320	640
Total MC sweeps [a]	4000000	4000000
T, h [b]	(0.995518, 0), (0.995995, 0), (0.996490, 0)	(0.994985, 0), (0.995209, 0), (0.995512, 0)
	(1.0752077, -0.5), (1.077044, -0.5), (1.078302, -0.5)	(1.075672, -0.5), (1.076181, -0.5), (1.076936, -0.5)
	(1.101447, -1.0), (1.102321, -1.0), (1.103380, -1.0)	(1.100386, -1.0), (1.101043, -1.0), (1.101811, -1.0)
N_{data} [c]	10	20

[a]the number sampled for each set of temperature and external field
[b]Three temperature values for each external field.
[c]The data were stored every N_{data} MC sweeps.

As for spin-updates, we employed the single spin update algorithm; we updated spins one by one with the heatbath algorithm. As for quasi-random-number generator, we used the Mersenne Twister [29].

4.2.3 Free energy calculations

The simulated tempering parameters, or free energies, in Eqs. (4.7) and (4.11) can be simply obtained by the reweighting techniques applied to the results of preliminary simulation runs [30, 16, 15, 14]. We used two reweighting methods for this free energy calculation. One method is the multiple-histogram reweighting method, or Weighted Histogram Analysis Method (WHAM) [31, 32] and the other is Multistate Bennett Acceptance Ratio estimator (MBAR) [33], which is based on WHAM.

The equations of WHAM algorithm applied to the system is as follows. For details, the reader is referred to Refs. [32, 15]. The density of states (DOS) $n(E, M)$ and free energy values $f(T_i, h_j)$ can be obtained from

$$n(E, M) = \frac{\sum_{T_i, h_j} n_{T_i, h_j}(E, M)}{\sum_{T_i, h_j} N_{T_i, h_j} \exp(f(T_i, h_j) - (E - h_j M)/T_i)}, \tag{4.15}$$

$$f(T_i, h_j) = -\ln \sum_{E, M} n(E, M) \exp(-(E - h_j M)/T_i), \tag{4.16}$$

where $n_{T_i, h_j}(E, M)$ is the histogram of E and M at T_i and h_j, and N_{T_i, h_j} is the total number of samples obtained at T_i and h_j. By solving these two equations self-consistently by iterations, we can obtain $n(E, M)$ and $f(T_i, h_j)$. The obtained $n(E, M)$ allows one to calculate any thermal average at arbitrary temperature and external field values. Note that $f(T_i, h_j)$ is determined up to a constant, which sets the zero point of free energy. Accordingly, $n(E, M)$ is determined up to a normalization constant.

The MBAR is based on the following equations. Namely, by combing Eqs.

(4.15) and (4.16), the free energy can be written as

$$f(T_i, h_j) = -\ln \sum_{n=1}^{N} \frac{\exp(-(E_n - h_j M_n)/T_i)}{\sum_{k=1}^{N_T} \sum_{l=1}^{N_h} N_{T_k,h_l} \exp(f(T_k, h_l) - (E_n - h_l M_n)/T_k)}, \tag{4.17}$$

where N, N_{T_k,h_l}, E_n, and M_n is the total number of data, the number of samples associated with T_k and h_l, energy of the n-th measurement, and magnetization of the n-th measurement, respectively. This equation should be solved self-consistently for $f(T_i, h_j)$. Note that, as in WHAM, $f(T_i, h_j)$ is determined up to a constant.

We repeat the preliminary STM simulations and free energy calculations until we finally obtain sufficiently accurate free energy values which let the system perform a random walk in the temperature and external field space during the STM simulation. We then perform final production runs.

Note that these two reweighting methods enable us to obtain not only dimensionless free energy values but also physical values at any temperature and at any external field. Such averages are given by

$$\langle A \rangle_{T,h} = \sum_{n=1}^{N} W_{na} A(x_n), \tag{4.18}$$

$$W_{na} = \frac{1}{\langle c_a \rangle} \frac{\exp(-(E_n - hM_n)/T)}{\sum_{k=1}^{N_T} \sum_{l=1}^{N_h} N_{T_k,h_l} \exp(f(T_k, h_l) - (E_n - h_l M_n)/T_k)}, \tag{4.19}$$

$$\langle c_a \rangle = \sum_{n=1}^{N} \frac{\exp(-(E_n - hM_n)/T)}{\sum_{k=1}^{N_T} \sum_{l=1}^{N_h} N_{T_k,h_l} \exp(f(T_k, h_l) - (E_n - h_l M_n)/T_k)}. \tag{4.20}$$

For details, the reader is referred to Refs. [33, 34].

We also used two other methods of free energy calculations. One is given as follows. By substituting $a(T, h)$ in Eq. (4.10) by the estimates for free energy

$\tilde{f}(T,h)$, we obtain

$$P(T,h) \propto e^{-f(T,h)+\tilde{f}(T,h)}. \tag{4.21}$$

We can write

$$f(T,h) = \tilde{f}(T,h) - \ln P(T,h) + \text{const.} \tag{4.22}$$

Here, $P(T,h)$ can be obtained as a histogram at each set of parameter values in a preliminary STM simulation. Thus, this equation enables one to refine the free energy much more easily than the reweighting methods, because the method does not require any iterations. This method does not work well, however, when $P(T_i,h_j)$ is too small (or $\tilde{f}(T_i,h_j)$ is too far away from true values) to obtain samples at (T_i,h_j), while the reweighting techniques still work.

The other method for the free energy calculations is a Wang-Landau-method-like scheme, where we subtract a fixed constant from the free energy value being sampled during preliminary simulations. To stand on the safe side, we did not use such data for reweighting techniques which, strictly speaking, requires equilibrium data as inputs. Note that this method also work with inaccurate free energy values. Thus, this method also works even when the free energy estimates are far away from sufficiently accurate values.

In the present work, we first used the reweighting methods and Wang-Landau-like scheme to obtain rough estimates of the free energy for the entire parameter space. We then used the combination of the reweighting methods and Eq. (4.22) for further refinements of the free energy.

4.3 Results and discussion

We first examine whether the STM simulations were carried out properly or not. Figures 4.2 and 4.3 show the time series of the temperature and the external field, respectively, for $L = 80$. In both plots we see block structures reflecting the first-order phase transition line at $h = 0$ in the Potts model (see Fig. 4.3) and the second-

order phase transition at the effective Ising transition temperature $T_c(h) \sim 1.1346$ for negative external field (see Fig. 4.2). Within these blocks, the temperature and external field realize random walks. The temperature and external field indeed realized random walks.

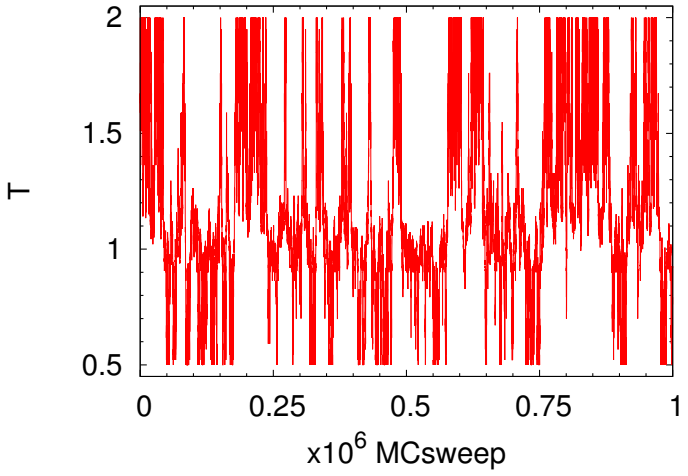

Figure 4.2: History of temperature T, for the linear lattice size $L = 80$.

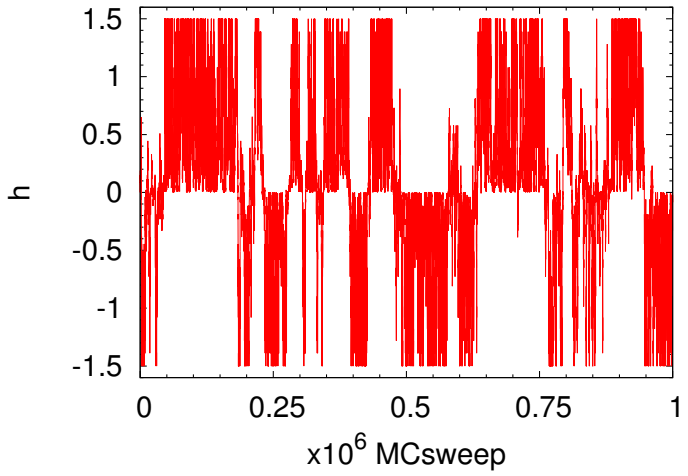

Figure 4.3: History of external field h, for the linear lattice size $L = 80$..

Figures 4.4 and 4.5 show energy and magnetization per spin, respectively, as functions of MC sweeps. They also perform random walks. Note that there exist expected correlations between the temperature and energy (see Figs. 4.2 and 4.4) and between the external field and magnetization (see Figs. 4.3 and 4.5). The same behavior was observed in simulation with other lattice sizes (data not shown).

Figure 4.6 shows the history of differently defined magnetization, which is given by

$$M_{\max} \equiv \left\{ \max_{j=0,1,2} \left[\sum_{i}^{L^2} \delta_{j,\sigma_i} \right] - \frac{L^2}{3} \right\} \times \frac{3}{2}. \tag{4.23}$$

Hereafter, we also use the following definition:

$$m \equiv \frac{M_{\max}}{L^2}. \tag{4.24}$$

In order to compare the results with ordinary ST simulations, we also performed an ST simulation with $L = 40$. The ST simulation was performed at the conditions similar to those of STM; namely, the same total number of MC sweeps, same temperature distribution, and so on, except that we set $h_0 = 0$.

With the data obtained, we performed the WHAM calculations to obtain the density of states (DOS). As shown in Fig. 4.7, the area sampled by STM is larger than that by ST. Thus, the STM method enables us to perform reweighting techniques in wider range.

We further closely looked into the difference in the sampled areas between two methods. Figure 4.8 illustrates how the sampled areas differ. The red regions were sampled by the STM method exclusively, the green regions by both methods, the blue region by the ST method only, and white regions by neither of them. Thus, at first sight, it seems that there are some areas in which the STM method is not good, and that the ST method is somehow more powerful than STM.

Figure 4.9 zooms in on a region where blue is dominant (mainly sampled by ST). There are many pigments (in red and green) which both methods sampled

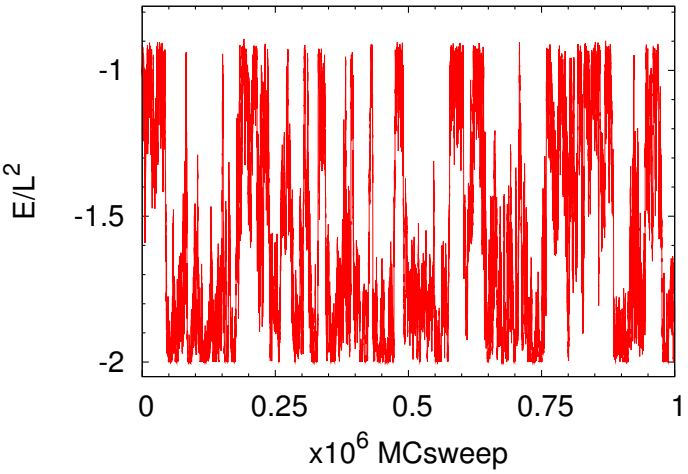

Figure 4.4: History of energy per spin, E/L^2, for the linear lattice size $L = 80$.

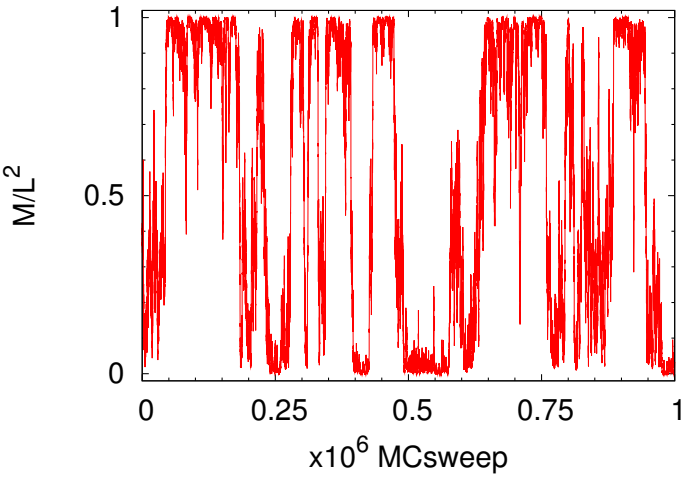

Figure 4.5: History of the magnetization per spin M/L^2, for the linear lattice size $L = 80$.

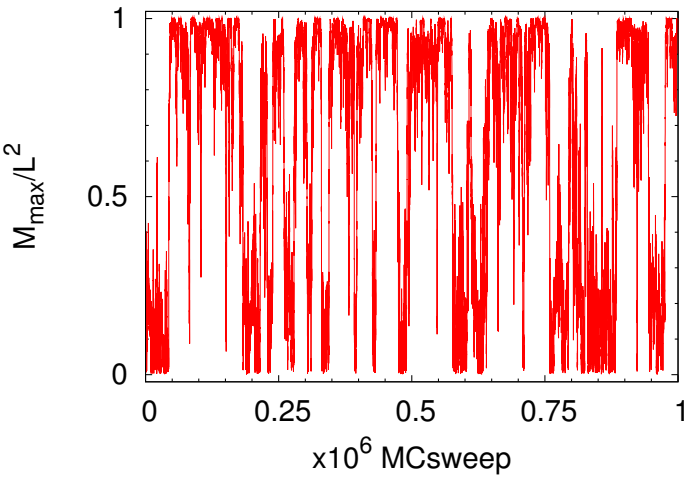

Figure 4.6: The history of $M_{\max}/L^2$ ($\equiv m$), for the linear lattice size $L = 80$.

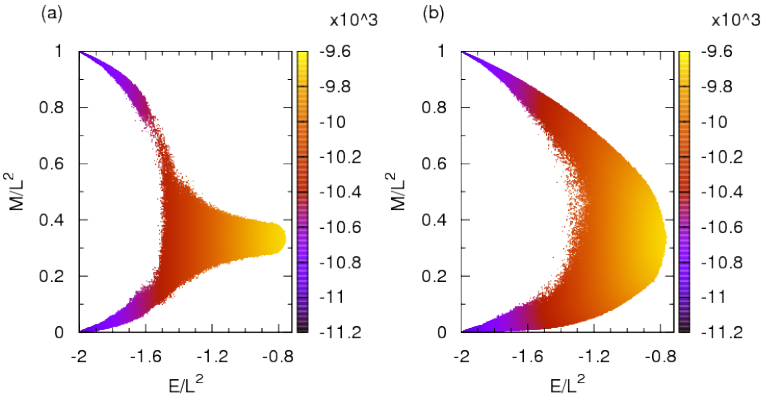

Figure 4.7: Calculated DOS obtained by WHAM with (a) ST and (b) ST data, for the linear lattice size $L = 80$.

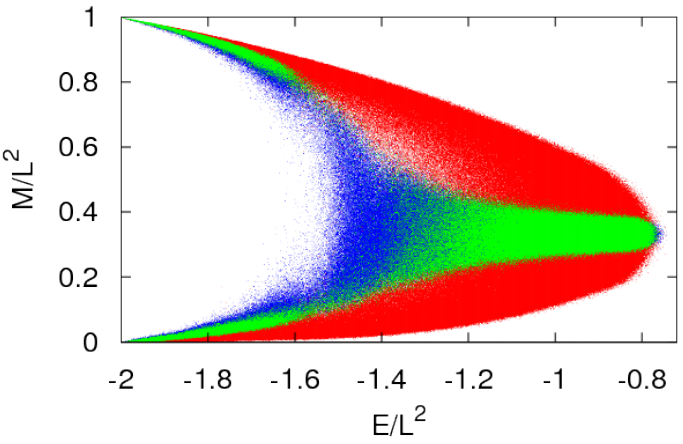

Figure 4.8: The difference in sampled points between ST and STM. The red area, green, blue, and white regions correspond to the area sampled by only STM, only by both of them, only by ST, and by neither of them, respectively ($L = 40$).

and which even only STM sampled. This shows that because the ST method has more samples at a smaller number of sets of parameter values, the part sampled is narrow but denser. However, the representative parts should be sampled properly by STM as well, although the sample density decreases.

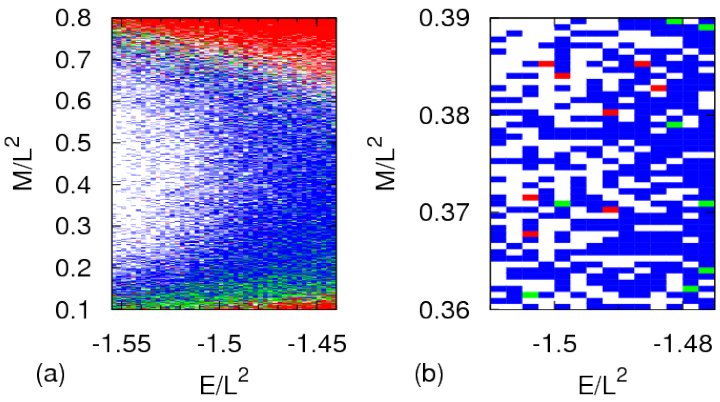

Figure 4.9: The zoom of Figure 4.8 with increasingly higher resolution. The difference in sampled points between ST and STM. The red area, green, blue, and white regions correspond to the area sampled by only STM, only by both of them, only by ST, and by neither of them, respectively.

To make it sure that the STM method also samples the relevant area enough, we then performed reweighting techniques along $h = 0$ with data obtained by ST and STM. Figrures 4.10 and 4.11 show the specific heat capacity C/L^2 and susceptibility χ/L^2 as a function of T along with $h = 0$, respectively. The red line and the green line correspond to the data obtained by STM and by ST, respectively. The error bars were obtained by the jackknife method [35, 36, 37]. We see no pronounced differences between the two methods. Thus, we confirm that both methods let one sample the representative parts along $h = 0$ and that the STM method enables one to obtain DOS at wider areas.

Because the STM method enables us to obtain the DOS in a wide range of sampling space, we can calculate the two-dimensional map of any thermal phys-

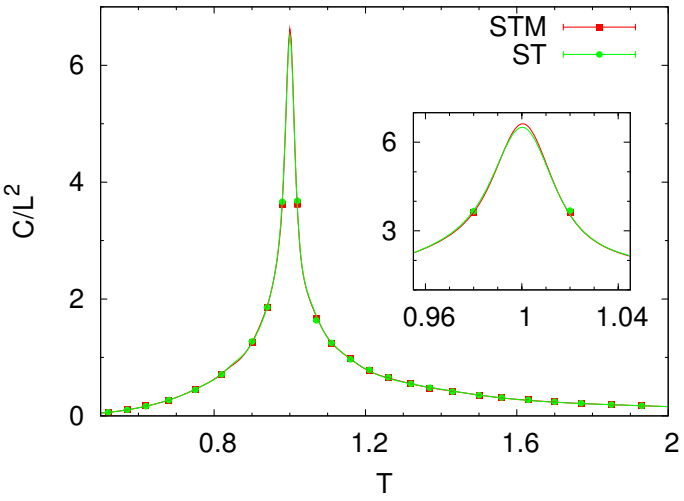

Figure 4.10: The heat capacity C/L^2 as a function of T, for $L = 40$. The inset shows the peak region with different abscissa and ordinate.

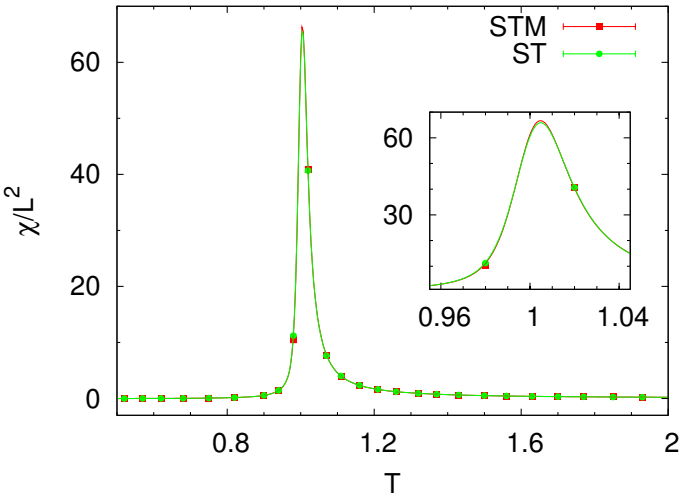

Figure 4.11: The susceptibility χ/L^2 as a function of T for $L = 40$. The inset shows the peak region with different abscissa and ordinate.

ical quantity. Figure 4.12 shows the specific heat capacity and susceptibility per spin as a function of T and h when $L = 80$. This implies that the phase transition temperature converges into the Ising case, as the external field increases. Related theoretical work is found in, e.g., Ref. [38].

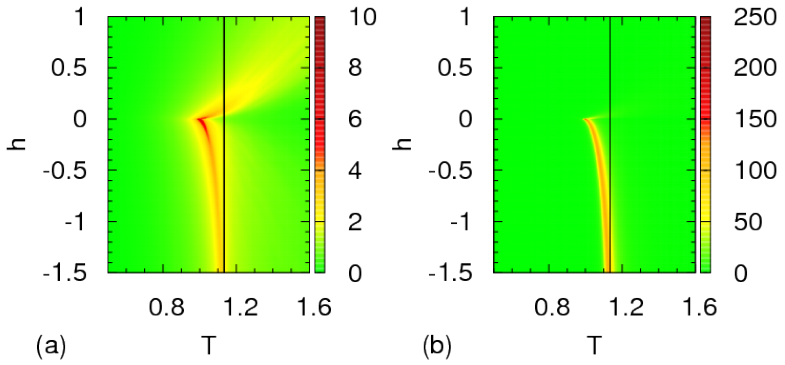

Figure 4.12: The map of C/L^2 and χ/L^2 as a function of T and h, for the linear lattice size $L = 80$. The black vertical line is $T = 1.1346$, which is the critical temperature of Ising model.

Figure 4.13 shows the specific heat as functions of temperature for some values of h and L. With positive external field, the phase transition disappears. However, because of finite-size effects, the abnormality, as measured by the diverging behavior, persists to some extent. With the smaller external field, the divergence behavior remains for larger L. Vice versa, with larger L, the more easily it can be shown that the diverging behavior disappears. This can be seen as a crossover between L and h.

Figure 4.14 shows the dimensionless free energy per spin as a function of temperature and external field, which was obtained by applying MBAR to the results of the production runs. Note that the partial differential of this free energy by h gives $\frac{\langle M \rangle}{TL^2}$. The shape at $h = 0$ suggests a jump of M below T_c, indicating

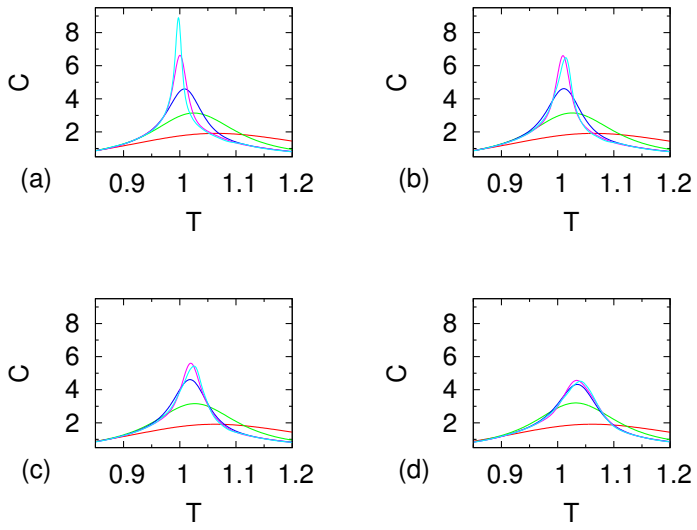

Figure 4.13: The specific heat C/L^2 as a function of T (a) $h = 0.0$, (b) $h = 0.005$, (c) $h = 0.01$ (d) $h = 0.02$. Red, green, blue, magenta, and cyan lines stands for $L = 5, 10, 20, 40$, and 80, respectively.

existence of the first-order phase transitions.

We study the crossover behavior of the phase transitions. We calculated the magnetization by MBAR around the critical point.

According to the crossover scaling formalism [39], if $t^{-14/9}h$ is small enough, then the magnetization obeys $m \sim t^{1/9}$, and if $h^{-9/14}t$ is small enough (i.e., $t^{-14/9}h$ is large enough), then it obeys $m \sim h^{1/14}$, where $t = \frac{T_c - T}{T_c}$. Figure 4.15(a) shows that if the finite-size effects are negligible ($L^{6/5}t \gg 0.1$) and $t \gg (h/6)^{9/14}$ (i.e., $t^{-14/9}h$ is small), then the critical behavior is $m \sim t^{1/9}$. Figure 4.15(b) shows that if finite-size effects are negligible ($L^{28/15}h \gg 0.1$) and $6t^{14/9} \ll h$ (i.e., $t^{-14/9}h$ is large), then the critical behavior is $m \sim h^{1/14}$. Thus, Fig. 4.15 clearly shows that the line ($h = 6t^{14/9}$) gives the slope of the boundary of the two scaling regimes.

We investigate the crossover behavior between the two models. With the negative external field, the model is expected to behave like the Ising model. Thus, as L increases the maximum values of $\frac{d\langle m\rangle}{d\beta}$, $\frac{d\ln\langle m\rangle}{d\beta}$, $\frac{d\ln\langle m^2\rangle}{d\beta}$, $\frac{d\ln\langle U_2\rangle}{d\beta}$, and $\frac{d\ln\langle U_4\rangle}{d\beta}$ change

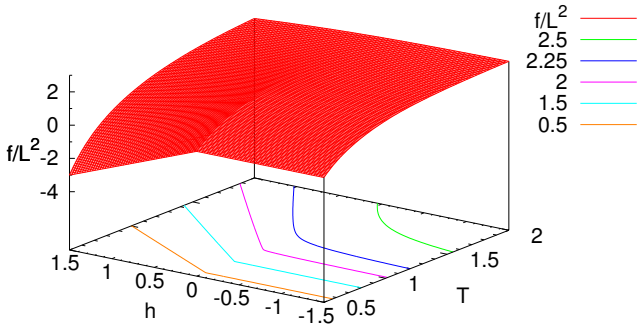

Figure 4.14: The free energy per spin f/L^2 and its contour curves as a function of T and h, for the linear lattice size $L = 80$.

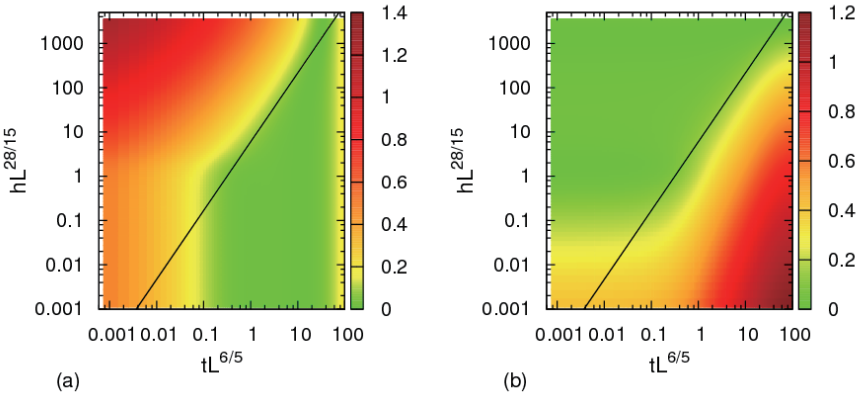

Figure 4.15: Difference between magnetization and its expected scaling behavior around the Potts critical point, for the linear lattice size $L = 80$. (a) $|mL^{2/15} - 1.2(L^{6/5}t)^{1/9}|$ is illustrated. The black line is $h = 6t^{14/9}$. (b) $|mL^{2/15} - (L^{28/15}h)^{1/14}|$ is illustrated. The black line is $h = 6t^{14/9}$.

their behaviors. Here, $U_2 = 1 - \frac{\langle m^2 \rangle}{3\langle m \rangle^2}$ and $U_4 1 - \frac{\langle m^4 \rangle}{3\langle m^2 \rangle^2}$ are the Binder cumulants [40]. Figures 4.16–4.20 show them. Note that $\frac{d\langle m \rangle}{d\beta}|_{\max}$, $\frac{d \ln\langle m \rangle}{d\beta}|_{\max}$, $\frac{d \ln\langle m^2 \rangle}{d\beta}|_{\max}$, $\frac{d \ln\langle U_2 \rangle}{d\beta}|_{\max}$, and $\frac{d \ln\langle U_4 \rangle}{d\beta}|_{\max}$ are expected to behave asymptotically as $L^{(1-\beta)/\nu}$, $L^{1/\nu}$, $L^{1/\nu}$, $L^{1/\nu}$, and $L^{1/\nu}$, respectively, as the lattice size L increases [37]. Those critical exponents in the two-dimensional Ising model and in the Potts model are given by $\nu = 1$ and $\beta = \frac{1}{8}$ and $\nu = \frac{5}{6}$ and $\beta = \frac{1}{9}$, respectively. We can observe that all quantities along $h = 0$ (red line with filled squares) follow the Potts case, and those with the external field at large L (green line with filled circles and blue line with filled triangles) follow the Ising case. Note that the two lines at $h = -0.5$ and $h = -1.0$ converge into almost the same line as L increases. On the other hand, the line at $h = -0.5$ (green line) is more deviated from the scaling behavior. This can be also understood as the crossover between L and h.

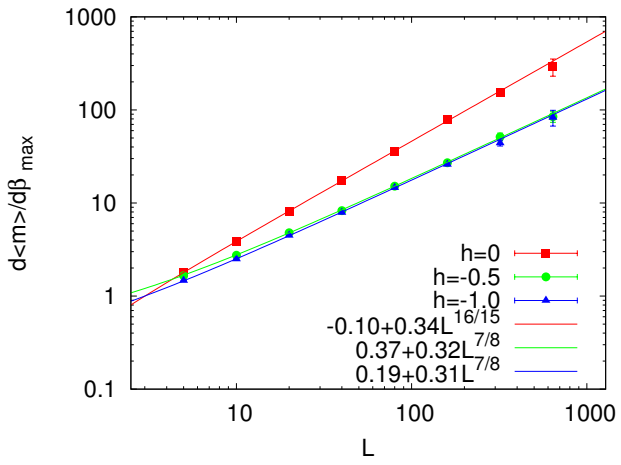

Figure 4.16: $\frac{d\langle m \rangle}{d\beta}|_{\max}$ as function of L.

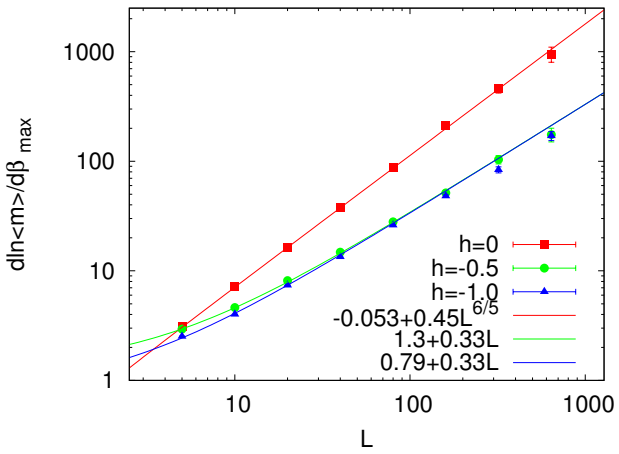

Figure 4.17: $\frac{d\ln\langle m\rangle}{d\beta}|_{\max}$ as function of L.

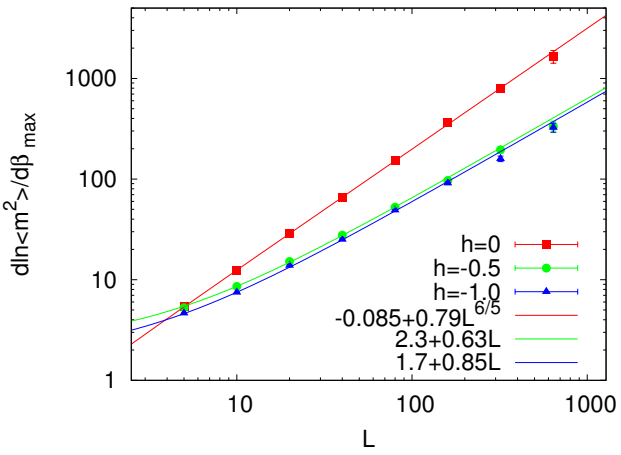

Figure 4.18: $\frac{d\ln\langle m^2\rangle}{d\beta}|_{\max}$ as function of L.

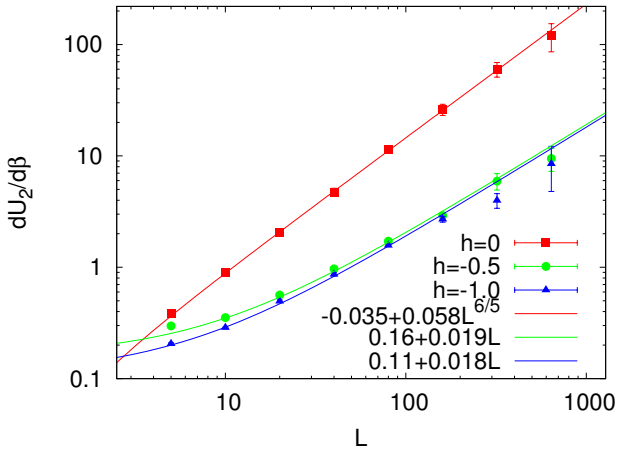

Figure 4.19: $\frac{d\ln\langle U_2\rangle}{d\beta}|_{\max}$ as function of L.

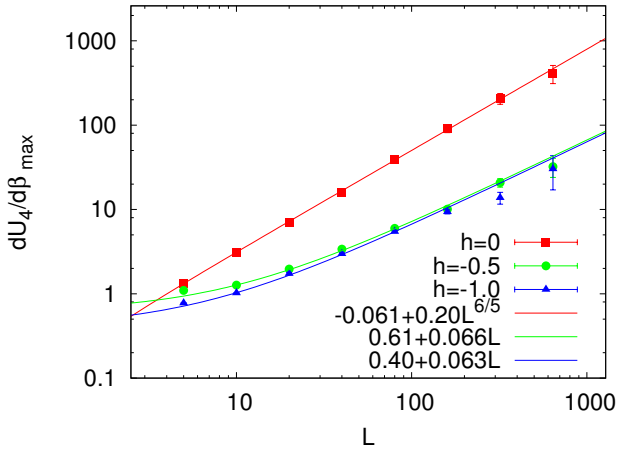

Figure 4.20: $\frac{d\ln\langle U_4\rangle}{d\beta}|_{\max}$ as function of L.

References

[1] W. Janke: *Physica A* **254**, 164 (1998).

[2] U. H. E. Hansmann and Y. Okamoto: in *Annual Reviews of Computational Physics VI* edited by D. Stauffer (World Scientific, Singapore, 1999) pp. 129–157.

[3] A Mitsutake, Y Sugita, and Y Okamoto: *Biopolymers* **60**, 96–123 (2001).

[4] B. A. Berg and T. Neuhaus: *Physics Letters B* **267**, 249–253 (1991).

[5] B. A. Berg and T. Neuhaus: *Physical Review Letters* **68**, 9–12 (1992).

[6] A. P. Lyubartsev, A. A. Martsinovski, S. V. Shevkunov, and P. N. Vorontsov-Velyaminov: *The Journal of Chemical Physics* **96**, 1776 (1992).

[7] E. Marinari and G. Parisi: *Europhysics Letters* **19**, 451–458 (1992).

[8] K. Hukushima and K Nemoto: *Journal of the Physics Society Japan* **65**, 1604–1608 (1996).

[9] C. J. Geyer: in *Computing Science and Statistics, Proceedings of the 23rd Symposium on the Interface*, edited by E. M. Keramidas (Interface Foundation of North America, 1991) pp. 156–163.

[10] F. Wang and D. P. Landau: *Physical Review Letters* **86**, 2050–2053 (2001).

[11] F. Wang and D. P. Landau: *Physical Review E* **64**, 056101 (16 pages) (2001).

[12] A. Laio and M. Parrinello: *Proc. Natl. Acad. Sci. USA* **99**, 12562–12566 (2002).

[13] R. H. Swendsen and J.-S. Wang: *Physical Review Letters* **57**, 2607–2609 (1986).

[14] A. Mitsutake and Y. Okamoto: *Physical Review E* **79**, 047701 (4 pages) (2009).

[15] A. Mitsutake and Y. Okamoto: *The Journal of Chemical Physics* **130**, 214105 (14 pages) (2009).

[16] A. Mitsutake: *The Journal of Chemical Physics* **131**, 094105 (15 pages) (2009).

[17] T Nagai and Y Okamoto: *Physics Procedia* **34**, 100–104 (2012).

[18] T. Nagai and Y. Okamoto: *Physical Review E* **86**, 056705 (12 pages) (2012).

[19] R. B. Potts: *Mathematical Proceedings of the Cambridge Philosophical Society* **48**, 106–109 (1952).

[20] F. Y. Wu: *Reviews of Modern Physics* **54**, 235–268 (1982).

[21] O. Philipsen. in *29th Johns Hopkins Workshop on Current Problems in Particle Theory: Strong Matter in the Heavens*, Vol. 1, p. 12, 2006.

[22] S. Kim, P. De Forcrand, S. Kratochvila, and T. Takaishi: arXiv preprint hep-lat/0510069 (2005).

[23] F. Karsch and S. Stickan: *Physics Letters B* **488**, 319–325 (2000).

[24] Y. D. Mercado, H. G Evertz, and C. Gattringer: *Computer Physics Communications* **183**, 1920–1927 (2012).

[25] J. D. Chodera and M. R. Shirts: *The Journal of Chemical Physics* **135**, 194110 (15 pages) (2011).

[26] C. Zhang and J. Ma: *The Journal of Chemical Physics* **132**, 244101 (16 pages) (2010).

[27] D. J. Sindhikara, Y. Meng, and A. E. Roitberg: *The Journal of Chemical Physics* **128**, 024103 (10 pages) (2008).

[28] D. J. Sindhikara, D. J. Emerson, and A. E Roitberg: *Journal of Chemical Theory and Computation* **6**, 2804–2808 (2010).

[29] M. Matsumoto and T. Nishimura: *ACM Transactions on Modeling and Computer Simulation (TOMACS)* **8**, 3–30 (1998).

[30] A. Mitsutake and Y. Okamoto: *Chemical Physics Letters* **332**, 131–138 (2000).

[31] A. Ferrenberg and R. Swendsen: *Physical Review Letters* **63**, 1195–1198 (1989).

[32] S. Kumar, J. M. Rosenberg, D. Bouzida, R. H. Swendsen, and P. A. Kollman: *Journal of Computational Chemistry* **13**, 1011–1021 (1992).

[33] M. R. Shirts and J. D. Chodera. *The Journal of Chemical Physics* **129**, 124105 (10 pages) (2008).

[34] A. Mitsutake, Y. Sugita, and Y. Okamoto: *The Journal of Chemical Physics* **118**, 6664 (12 pages) (2003).

[35] R. G. Miller: *Biometrika* **61**, 1–15, 1974.

[36] B. A. Berg: *Markov Chain Monte Carlo Simulations and Their Statistical Analysis* (World Scientific, Singapore, 2004); `http://www.worldscibooks.com/physics/5602.html`.

[37] W. Janke: *Lect. Notes Phys.* **739**, 79–140 (2008).

[38] G. Sun: *Zeitschrift fur Physik B Condensed Matter* **82**, 431–432 (1991).

[39] M. E. Fisher: *Reviews of Modern Physics* **46**, 597–616 (1974).

[40] K. Binder: *Zeitschrift für Physik B Condensed Matter* **43**, 119–140 (1981).

Chapter 5

Conclusions

In this thesis we explored the generalized-ensemble algorithms. We first carried out the REMD simulations and studied biological lipid bilayer systems, and we introduced a new ST method. We applied the method to Potts model as well as Ising model.

In Chapter 2 we performed a REMD simulation of a DPPC bilayer system in order to study the phase transitions. The bilayer underwent many phase transitions between gel and sol phases during the simulation. We believe that this is crucial to sample gel phases correctly. The reason is that, in the annealing simulations, systems can easily get trapped in local-minimum-energy states and cannot escape from the states because temperatures decrease only. On the other hand, REMD lets the system make a random walk in the temperature space so that the system can explore the conformational space more widely. It is worth noting that we could discuss well-equilibrated states in a wide range of temperature because the REMD method gives correct distributions at any temperature. This is not so easy by conventional methods.

We examined the temperature dependences of the enthalpy, heat capacity, thickness of bilayer, and area of bilayer. The phase-transition temperature itself was in agreement with the previous work [1] by Marrink *et al*.

We also examined the temperature dependence of many component energy terms. We found the average bond-length energy and the average LJ potential

energy between water molecules and DPPC have different behaviors from the other energy terms. These two terms favor the sol phase, as the system is cooled. On the other hand, the other terms favor the gel phase.

To investigate the conformational property, we examined the PMF maps and tilt angle distributions at four different temperatures. Conformations were classified into three states, namely, sol, untilted gel, and tilted gel states. The tilted gel state was observed for the first time with MARTINI2.0, while a previous work with MARTINI did not find this state.[1] Experiments support the existence of the tilted-gel state. This implies the importance of employing powerful conformational sampling techniques such as generalized-ensemble algorithms in simulations of bilayer systems.

It was experimentally found that some hybrid liposomes composed of 90 mol % phospholipids and 10 mol % polyoxyethylene dodecyl ether with no antitumor drugs can kill only cancer cells without affecting normal cells [2, 3]. In particular, three hybrid liposomes composed of phospholipids having the same hydrophilic head group but different hydrophobic alkyl chains were studied. It was found that the hybrid liposomes composed of phospholipids dilauroylphosphatidylcholine (DLPC), dimyristoylphosphatidylcholine (DMPC), and dipalmitoylphosphatidylchoine (DPPC) cause necrosis, apoptosis, and no changes, respectively [4]. Although both necrosis and apoptosis result in deaths of cells, necrosis is toxic and only apoptosis is a desired phenomenon for the organisms. The differences in these three phospholipids are just the lengths of the hydrophobic alkyl chains; DLPC, DMPC, and DPPC have 12, 14, and 16 carbon atoms after glycerol. The sol-gel phase transition temperatures T_c of the regular liposomes composed of DLPC, DMPC, and DPPC are 273 K, 296 K, and 313 K, respectively (those of hybrid liposomes are slightly lower than these pure liposome values) [5]. Hence, at the body temperature of 310 K, they are in sol phase much above T_c, in sol phase near T_c, and in gel phase, respectively. We simply conjecture that the differences of the effects of the hybrid liposomes above on the tumor cells are just the reflections of these phase differences. If this is true, we should observe, for instance, apoptosis, no effects, and no effects with hybrid liposomes composed of DLPC, DMPC, and DPPC, respectively, at the temperature of experiments around

290 K. Likewise, we expect that necrosis, necrosis, and aptopsis with hybrid liposomes composed of DLPC, DMPC, and DPPC, respectively, at the temperature of experiments around 330 K. These investigations with experiments and simulations at different temperatures are our future works.

In Chapter 3, we have introduced a two-dimensional simulated tempering in temperature and external field, which we refer to as Simulated Tempering and Magnetizing (STM). We applied it to the two-dimensional Ising model. During the simulations, two-dimensional random walks in temperature and external field were realized. The random walk covered a wide area of temperature and external field so that the STM simulations enabled us to study a wide area of phase diagram from a single simulation run.

Even though the first-order phase transitions along the external field change did not directly occur, the transitions happened through high temperature regions, or "super critical water regions." The dimensional extension allowed us to overcome the difficultly of the first-order phase transitions. Thus, this result suggests that the dimensional extension allows us to overcome the difficulty of crossing the first-order phase transition points with the ST method. The similarity between ST and REM implies that the dimensional extension of REM will also give this property (An example is shown for the case of a two-dimensional REM simulation in temperature and pressure in Ref. [6]). In this way we see that the method is more conveniently expanded.

We also performed STM simulations with several different parameter-updating frequencies. According to the convergence and sizes of error bars, the more frequent attempts should be the better choice. The calculated auto-correlation time also suggested that the frequent attempt is favorable.

We investigated the crossover behavior of phase transitions by calculating the magnetization per spin m around the critical point by the reweighting techniques. The results showed agreement with the previous theoretical studies. Thus, this supports the validity of the two-dimensional ST method, or STM.

With the data of the present work, we can calculate the two-dimensional density of states $n(E, M)$, so that we can determine the weight factor for the two-dimensional multicanonical simulations. Therefore, we can also perform the two-

dimensional multicanonical simulations. The STM method will be very useful for simulating spin-glass systems.

In Chapter 4, we further applied Simulated Tempering and Magnetizing (STM) [8, 7] to the two-dimensional three-state Potts model. During the simulations, two-dimensional random walks in temperature and external field were realized. In this way, the random walk covered a wide area of temperature and external field so that the STM simulations enabled us to study a wide area of phase diagram from production runs.

Because of the method's capability of dealing with a wider area of the sampling space (as seen in DOS), we can calculate thermal quantities at an enlarged range of the parameter space. We have succeeded in producing many typical features of the systems in presence of the external field.

We investigated the crossover behaviors of phase transitions by calculating the magnetization per spin around the critical point by the reweighting techniques. The results showed agreement with the previous theoretical studies. Thus, this supports the validity of the STM method.

With the data of the present work, we can calculate the two-dimensional density of states $n(E, M)$, so that we can determine the two-dimensional multicanonical weight factor. Therefore, we can also perform the two-dimensional multicanonical simulations. This is also our future work. We remark that the present methods are useful not only for spin systems but also for other complex systems with many degrees of freedom. Note that because this method does not require one to change the energy calculation, the method should be highly compatible with existing package programs.

References

[1] S. J. Marrink, H. J. Risselada, and A. E. Mark: *Chem. Phys. Lipids* **135**, 223–244 (2005) .

[2] K. Nakano, Y. Iwamoto, W. Takata, Y. Matsumoto and R. Ueoka: *Bioorg. Med. Chem. Lett.* **12**, 3251–3254 (2002) .

[3] Y. Matsumoto, Y. Iwamoto, T. Matsushita and R. Ueoka : *Int. J. Cancer* **115**, 377–382 (2005).

[4] H. Nagami, K. Nakano, H., Ichihara, Y. Matsumoto and R. Ueoka: *Bioorg. Med. Chem. Lett.* **16**, 782–785 (2006) .

[5] R. Ueoka, Y. Matsumoto, K. Goto, H. Ichihara, and Y. Komizu: *Curr. Pharm. Des.* **17**, 1709–1719 (2011).

[6] Y. Sugita and Y. Okamoto: in *Lecture Notes in Computational Science and Engineering*, edited by T. Schlick and H. H. Gan (Springer, Berlin, 2002) pp. 304–332; http://arxiv.org/abs/cond-mat/0102296.

[7] T. Nagai and Y. Okamoto: *Physical Review E* **86**, 056705 (12 pages) (2012).

[8] T. Nagai and Y. Okamoto: *Physics Procedia* **34**, 100–104 (2012).

Appendices

Appendix A

Errors of Correlated Data

In this Appendix, we look into the method of evaluation of errors [1, 2]. Our particular aim here is the analysis of autocorrelated data.

Without correlation, the error σ is evaluated by the common formula:

$$\sigma^2 = \frac{1}{N(N-1)} \sum_{i=1}^{N} \left(A_i - \hat{A}\right)^2 , \tag{A.1}$$

where N, A_i, and $\hat{A}$ are the total number of samples, the i-th sample, and the average of samples, respectively. However, this does not work well when there are correlations between samples. We particularly explore how to modify Eq. (A.1) in order to cope with autocorrelations.

A.1 Introduction

We assume that random variables A and B have the (finite) expected values ($\langle A \rangle$ and $\langle B \rangle$, respectively) and (finite) variances (σ_A^2 and σ_B^2, respectively). These are not usually known and to be estimated. Given the probability density of A, $f(A)$, the expected value is given by $\langle A \rangle = \int A f(A)\, dA$. Note that, in this section, brackets $\langle\rangle$ indicate the "theoretical" averages, which are determined independently of samples. As you should know, we can derive $\langle A + B \rangle = \langle A \rangle + \langle B \rangle$ and $\langle aA \rangle = a \langle A \rangle$ with constant a.

When there are no correlations between A and B, we have well-known formulae:

$$\sigma^2_{A+B} = \sigma^2_A + \sigma^2_B \tag{A.2}$$

$$\sigma^2_{aA} = a^2\sigma^2_A, \tag{A.3}$$

where σ^2_{A+B} and σ^2_{aA} are the variance of $A + B$ and aA, respectively. On the other hand, with correlation, the variance of $A + B$ is given by $\sigma^2_{A+B} = \sigma^2_A + \sigma^2_B + 2\mathrm{cov}(A, B)$, where $\mathrm{cov}(A, B) = \langle (A - \langle A\rangle)(B - \langle B\rangle)\rangle$.

Equation (A.1) is actually based on Eqs. (A.2) and (A.3), and therefore the independence between samples is assumed. This is why Equation (A.1) does not work with correlated data and we need a more careful treatment.

A.2 Errors of non-correlated samples

A.2.1 Basics

Let us first look into the analysis of non-correlated data. We suppose that we have N independent samples $(A_1, A_2, \ldots, A_N)$ from an identical distribution. The expected value and variance are given by

$$\langle A\rangle = \int A f(A)\, dA, \tag{A.4}$$

$$\sigma^2_A = \int (A - \langle A\rangle)^2 f(A)\, dA, \tag{A.5}$$

respectively. What we want to do is to estimate $\langle A\rangle$ and its error.

The expected value $\langle A\rangle$ can be estimated by the average $\hat{A}$:

$$\hat{A} = \frac{1}{N}\sum_{i=1}^{N} A_i\,. \tag{A.6}$$

Note that we distinguish the estimates from the true values by denoting the estimates and the true values as $\hat{A}$ and $\langle A\rangle$, respectively.

The average $\hat{A}$ is a "good" estimator for $\langle A \rangle$, because we have $\left\langle \hat{A} \right\rangle = \langle A \rangle$. The average of estimates goes to the true value. Thus, this is an unbiased estimate.

The error of the average is given by the standard deviation of the average. The variance of the average $\sigma^2_{\hat{A}}$ is given by

$$\sigma^2_{\hat{A}} = \frac{\sigma^2_A}{N}, \tag{A.7}$$

because we have, denoting $V(\bullet) \equiv \sigma^2_\bullet$ for the aid of eye,

$$\begin{aligned} \sigma^2_{\hat{A}} = V(\hat{A}) &= V((A_1 + A_2 + \cdots + A_N)/N) && \text{(A.8)} \\ &= 1/N^2 V(A_1 + A_2 + \cdots + A_N) && \text{(A.9)} \\ &= \frac{1}{N} V(A) = \frac{\sigma^2_A}{N}. && \text{(A.10)} \end{aligned}$$

Recall that A_1, A_2, ..., and A_N follows an independent identical distribution of which variance is $V(A) \equiv \sigma^2_A$. It should be worth to note that the average $\hat{A} = (A_1 + A_2 + \cdots + A_N)/N$ is considered as a new random variable.

Thus, if one knows the variance σ^2_A, one can obtain the variance of average $\sigma^2_{\hat{A}}$. However, this is generally not known *a priori*. Therefore, the question is how σ^2_A can be estimated. The estimator of σ^2_A, $\hat{\sigma}^2_A$ is given not by $\hat{\sigma}^2_A = \frac{1}{N}\sum_{i=1}^N (A_i - \hat{A})^2$ but by

$$\hat{\sigma}^2_A = \frac{1}{N-1}\sum_{i=1}^N (A_i - \hat{A})^2, \tag{A.11}$$

though there existing only a slight difference with large N.

Thus, the estimator for error $\hat{\sigma}_{\hat{A}}$ is given via the estimator for the variance of average $\hat{\sigma}^2_{\hat{A}}$:

$$\hat{\sigma}^2_{\hat{A}} = \frac{1}{N(N-1)}\sum_{i=1}^N (A_i - \hat{A})^2. \tag{A.12}$$

Especially, if N is large enough to use the central limit theorem, then we can

use the nature of the Gauss distribution. (For example $\pm 1.96\sigma$ gives the 95 % confidence interval.)

Table A.1 gives the summary of these quantities for the better availability of reference.

Table A.1: Summary for the quantities. The i-th sample is denoted by A_i.

Notation	Definition	Description
$\langle A \rangle$	$\int A f(A)\, dA$	Expected value of A
σ_A^2	$\int (A - \langle A \rangle)^2 \, f(A)\, dA$	Variance of A
$\hat{A}$	$\frac{1}{N} \sum A_i$	Average of samples (Estimator for expected value)
$\hat{\sigma}_A^2$	$\frac{1}{N-1} \sum \left(A_i - \hat{A}\right)^2$	Estimator for variance (of A)
$\sigma_{\hat{A}}^2$	$\frac{1}{N}\sigma_A^2$	Variance of average (the second power of error)
$\hat{\sigma}_{\hat{A}}^2$	$\frac{1}{N}\hat{\sigma}_A^2 = \frac{1}{N(N-1)} \sum \left(A_i - \hat{A}\right)^2$	Estimator for variance of average (Estimator for the second power of error)

A.2.2 Blocking/binning method in the case without correlations

We explore a blocking (or binning) method with samples without correlations. We introduce a new random variable: $A_{i/2}^{(2)} = (A_{i-1} + A_i)/2$, where $(i = 2, 4, 6 \ldots)$. Therefore, there are $N/2$ new blocks or bins. Because there are no correlations

between samples, the variance of $A^{(2)}$ is given by $\sigma^2_{A^{(2)}} = \sigma^2_A/2$. Note that

$$V\left(A^{(2)}\right) = V\left(\frac{1}{2}\left(A_1 + A_2\right)\right) \tag{A.13}$$

$$= \frac{1}{4}V\left(\left(A_1 + A_2\right)\right) \tag{A.14}$$

$$= \frac{1}{2}V\left(A\right) \tag{A.15}$$

As you see easily, the expected value is the same: $\left\langle A^{(2)}\right\rangle = \langle A\rangle$.

We shall look into the estimates for average and its error of this new variable. The estimate of $\left\langle A^{(2)}\right\rangle$, $\hat{A}^{(2)}$ is given by the average:

$$\hat{A}^{(2)} = \frac{1}{N/2}\sum_{i=1}^{N/2} A_i^{(2)} \tag{A.16}$$

$$= \frac{1}{N}\sum_{i=1}^{N} A_i. \tag{A.17}$$

Because $\frac{N}{2}$ bins exist, the variance of average of the new variable, $\sigma^2_{\hat{A}^{(2)}}$ is given by

$$\sigma^2_{\hat{A}^{(2)}} = \frac{\sigma^2_{A^{(2)}}}{N/2}. \tag{A.18}$$

The estimate of the variance of the new variables after one blocking transformation is given by

$$\hat{\sigma}^2_{A^{(2)}} = \frac{1}{N/2-1}\sum_{i=1}^{N/2}(A_i^{(2)} - \hat{A}^{(2)})^2. \tag{A.19}$$

Note that the sum is divided by $(N/2-1)$ not $N/2$. Hence, we arrive at

$$\hat{\sigma}^2_{\hat{A}^{(2)}} = \frac{1}{N/2(N/2-1)}\sum_{i=1}^{N/2}(A_i^{(2)} - \hat{A}^{(2)})^2. \tag{A.20}$$

We further look into the relation between $\sigma^2_{\hat{A}}$ and $\sigma^2_{\hat{A}^{(2)}}$. Using $\sigma^2_{A^{(2)}} = \sigma^2_A/2$, we have

$$\sigma^2_{\hat{A}^{(2)}} = \frac{\sigma^2_{A^{(2)}}}{N/2} \tag{A.21}$$

$$= \frac{\sigma^2_A/2}{N/2} \tag{A.22}$$

$$= \frac{\sigma^2_A}{N} \tag{A.23}$$

$$= \sigma^2_{\hat{A}}. \tag{A.24}$$

Thus, the error of average of $N/2$ samples (bins) of $\hat{A}^{(2)}$ is the same as the error of average of N samples of A. The blocking process does not change the average and its error of uncorrelated data. Note that we later discuss the repetition of this procedure.

A.2.3 Repeating of blocking

By repeating this procedure, we obtain a set of samples $A^{(n+1)}$. One of the sample $A^{(n+1)}_i$ is the average of 2^n samples of A. The number of samples $A^{(n+1)}$ is $N/2^n$. Let us remember that one blocking process does not change the average and its error (or the variance of average), as discussed in the preceding section. Therefore, the average and its error of such new samples obtained by repetition of blocking data are the same as those of the original samples in the non-correlated data analysis.

If n is large enough, $A^{(n+1)}$ is expected to follow a Gaussian distribution because of the central limit theorem. Thus, the average of $A^{(n+1)}$, $\hat{A}^{(n+1)}$ follows t-distribution with $N/2^n - 1$ degree of freedom. (t-distribution is a distribution of average of any number of samples from a Gaussian distribution.) The t-distribution can be regarded as a Gaussian distribution, when there are more than 16 [*1] to 30 [*2] samples.[*3]

[*1] Berg's book

[*2] http://www.aandt.co.jp/jpn/qc/basic/tbunpu.htm [in Japanese; accessed on 03.July 2012]

[*3] For instance the 95% CI of t-distribution with degree of freedom 20 is given by 2.09σ, while that of a Gaussian distribution is 1.96σ.

A.3 Errors of correlated data

We shall discuss the error of correlated data. We can eliminate the correlation between data of MC or MD simulations by blocking method introduced above.

We first show that the errors grow by blocking procedures when there is a positive correlation. The variance of average of new variable is given by the blocking procedure in the following manner:

$$\sigma^2_{\hat{A}^{(2)}} = V[(x_i + x_{i+1})/2] = 1/4V(x_i + x_{i+1}), \tag{A.25}$$

$$V(x_i + x_{i+1}) = 2V(x_i) + 2\mathrm{cov}(x_i, x_{i+1}), \tag{A.26}$$

where $\mathrm{cov}(x_i, x_{i+1}) = \langle (x_i - \langle x \rangle)(x_{i+1} - \langle x \rangle) \rangle$. We then obtain

$$\sigma^2_{\hat{A^{(2)}}} = \frac{\sigma^2_A}{2} + \frac{1}{2}\mathrm{cov}(x_i, x_{i+1}). \tag{A.27}$$

Thus, the samples after a blocking transformation has an extra term, which is half of the autocorrelation. Supposing the extremely strong correlation, we have $\mathrm{cov}(x_i, x_{i+1}) \approx V(x)$. Thus, the variance of $A^{(2)}$, $\sigma^2_{A^{(2)}}$ is given by $\sigma^2_{A^{(2)}} = \sigma^2_A$. The variance of average is given by the variance of new samples divided by $N/2$:

$$\sigma^2_{\hat{A}^{(2)}} = \frac{\sigma^2_{A^{(2)}}}{N/2} \tag{A.28}$$

$$= \frac{\sigma^2_A}{N/2} = 2\frac{\sigma^2_A}{N} \tag{A.29}$$

$$= 2\sigma^2_{\hat{A}}. \tag{A.30}$$

The variance of $\hat{A}^{(2)}$, $\sigma^2_{\hat{A}^{(2)}}$ is twice as the variance of $\hat{A}$, $\sigma^2_{\hat{A}}$ Thus, its standard deviation (error) becomes $\sqrt{2}$ times larger.

Obviously, as the correlation between samples decreases by repeating the blocking procedures, the change of error by one blocking procedure becomes smaller. It is supposed to stop finally (when $\mathrm{cov}(A^{(n)}_i, A^{(n)}_{i+1}) = 0$). Thus, blocking n-times and observing the stop of change, we can obtain uncorrelated data. Therefore, we obtain the errors taking account of correlations. In this way, we can

estimate errors by performing a sufficient number n times transformations:

$$\hat{\sigma}^2_{\hat{A}^{(n)}} = \frac{1}{N/2^n\,(N/2^n - 1)} \sum_{i=1}^{N/2^n} \left(A_i^{(n+1)} - \hat{A}^{(n+1)} \right). \tag{A.31}$$

A.4 Comment about interpretation of error bar

To interpret the error bars as a standard deviation of Gaussian distribution, we need the "sufficiently large number" of samples. It is because of the central limit theorem. The question is how many samples (bins) are enough to take this approximation. It can be answered by observing t-distributions, which give the distribution of the average of independent N samples from an identical Gaussian distribution. We can regard t-distribution as Gaussian distribution if we have more than 16 to 30 samples. Thus, if we have more than 16 bins/blocks, which has no correlations by applying n blocking, then the obtained error bar is considered as standard deviation of a Gaussian distribution. In other words, we want the deviation to converge before the bin number becomes less than 16. If the deviation converge later than this, the error bar should be treated as the deviation of t-distribution. If it does not converge, what we have is only the minimum level of error.

References

[1] H. Flyvbjerg and H. G. Petersen: *J. Chem. Phys.* **91**, 461 (6 pages) (1989).

[2] B. A. Berg, "Markov Chain Monte Carlo Simulations and Their Statistical Analysis" (World Scientific, Singapore 2004); http://www.worldscibooks.com/physics/5602.html .

Appendix B

Jackknife Method

B.1 Introduction

Suppose that we have N samples: $A_1, A_2, \ldots, A_N$. The average $\hat{A}$ ($=\frac{1}{N}\sum A_i$) is a good estimate of expectation of A because we have $\left\langle \hat{A} \right\rangle = \langle A \rangle$. In other words, the expected value of the estimate is given by the theoretical expectation. However, one has to pay attention when one estimates something given by non-linear function f of $\langle A \rangle$ [1, 2, 3]. A typical example is $\langle E \rangle^2$, which makes up the heat capacity. The bad way is $\hat{f} = \frac{1}{N}\sum f_i$, where $f_i = f(A_i)$. This is a bad estimator and $\hat{f}$ does not converge into $\langle f \rangle$. Precisely, we have to use

$$\hat{f} = f(\hat{A}). \tag{B.1}$$

One typical example is to calculate a specific heat ($\propto \left\langle E^2 \right\rangle - \langle E \rangle^2$), with samples of energy $E_1, E_2, \ldots, E_N$. To obtain latter term, we have to use

$$\hat{\langle E \rangle^2} = \left(\frac{1}{N} \sum E_i \right)^2, \tag{B.2}$$

not $\hat{\langle E \rangle^2} = \frac{1}{N}\sum E_i^2$. (If you do it wrong, the specific heat is estimated to be always zero; thus the bad estimator has typically a bias of order of $O(1)$.)

In this case the error of $\hat{f}$ can not be obtained, because we do not have f_i any

longer. Supposing error and non-linearity of f are small, you can use propagation formula: $\delta f = \frac{df}{dA}|_{A=\hat{A}}\ \delta A$. However, this is not always robust and recommendable.

B.2 Jackknife method

A robust method of estimating errors is the jackknife method [1, 2, 3]. The error by the jackknife method with N samples is given by

$$(\hat{\sigma}_f^J)^2 = \frac{N-1}{N}\sum_{i=1}^{N}\left(f_i^J - \hat{f}^J\right)^2, \tag{B.3}$$

where

$$f_i^J = f(A_i^J), \tag{B.4}$$

$$A_i^J = \frac{1}{N-1}\sum_{j=1, j\neq i}^{N} A_j, \tag{B.5}$$

$$\hat{f}^J = \frac{1}{N}\sum f_i^J. \tag{B.6}$$

In other words, A_i^J is an average of samples except the i-th sample. If $f(x) = x$, this form leads to the ordinary form, which gives the error of the average.

B.2.1 Dealing with correlation with jackknife method

In the jackknife method with blocking or binning, we first separate N samples into K bins containing n samples for each (Note that $K = N/n$). The k-th bin contains

the samples for $(k-1)n < i \leq kn$. We then have the following forms:

$$(\hat{\sigma}_f^J)^2 = \frac{K-1}{K}\sum_{k=1}^{K}(f_k^J - \hat{f}^J)^2, \tag{B.7}$$

$$f_k^J = f(A_k^J), \tag{B.8}$$

$$\hat{f}^J = \frac{1}{K}\sum f_i^J, \tag{B.9}$$

$$A_k^J = \frac{1}{N-n}\sum_{j=1, j\notin bin(k)}^{N} A_j. \tag{B.10}$$

Here, A_k^J is the average excluding the samples in the k-th bin.

If we observe the convergence of $(\hat{\sigma}_f^J)^2$, as increasing the number of samples in each bin (accordingly decreasing the number of bins), we then obtain the errors taking account of autocorrelations.

As is in A.3, $\hat{\sigma}_f^J$ becomes $\sqrt{2}$ times if there is strong correlations. By repeating binning, we can obtain the errors without correlations.

References

[1] R. G. Miller:*Biometrika* **61**, 1–15, (1974).

[2] H. Flyvbjerg and H. G. Petersen: *J. Chem. Phys.* **91**, 461 (6 pages) (1989).

[3] B. A. Berg, "Markov Chain Monte Carlo Simulations and Their Statistical Analysis" (World Scientific, Singapore, 2004); http://www.worldscibooks.com/physics/5602.html .

Appendix C

Relation Between Ordinary Blocking and Blocking with Jackknife Method

Here, we look into the relation between the ordinary blocking [1] and blocking with jackknife method [2]. If f is linear in jackknife method (f_i is unbiased), then the blocking form of jackknife method leads to the form of ordinary blocking. Supposing $f(x) = x$ for simplicity, we shall start with the form of jackknife method. We first have

$$(\hat{\sigma}_A^J)^2 = \frac{K-1}{K}\sum_{k=1}^{K}(A_k^J - \hat{A})^2, \tag{C.1}$$

$$\hat{A} = \hat{A}^J = \frac{1}{K}\sum A_i^J = \frac{1}{N}\sum A_i, \tag{C.2}$$

$$A_k^J = \frac{1}{N-n}\sum_{j=1, j\notin bin(k)}^{N} A_j. \tag{C.3}$$

We then calculate:

$$A_k^J - \hat{A} = \frac{1}{N-n} \sum_{j \notin bin(k)} A_j - \frac{1}{N} \sum_j A_j \tag{C.4}$$

$$= \frac{1}{N-n} \sum_j A_j - \frac{1}{N-n} \sum_{j \in bin(k)} A_j - \frac{1}{N} \sum_j A_j \tag{C.5}$$

$$= \left(\frac{1}{N-n} - \frac{1}{N} \right) \sum_j A_j - \frac{1}{N-n} \sum_{j \in bin(k)} A_j \tag{C.6}$$

$$= \frac{n}{N-n} \left(\frac{1}{N} \sum_j A_j - \frac{1}{n} \sum_{j \in bin(k)} A_j \right) \tag{C.7}$$

$$= \frac{n}{nK-n} \left(\frac{1}{N} \sum_j A_j - \frac{1}{n} \sum_{j \in bin(k)} A_j \right) \tag{C.8}$$

$$= \frac{1}{K-1} \left(\frac{1}{N} \sum_j A_j - \frac{1}{n} \sum_{j \in bin(k)} A_j \right). \tag{C.9}$$

Thus, we have

$$(\hat{\sigma}_A^J)^2 = \frac{K-1}{K} \sum_{k=1}^{K} (A_k^J - \hat{A})^2 \tag{C.10}$$

$$= \frac{K-1}{K} \sum_k \left(\frac{1}{K-1} \right)^2 \left(\frac{1}{N} \sum_j A_j - \frac{1}{n} \sum_{j \in bin(k)} A_j \right)^2 \tag{C.11}$$

$$= \frac{1}{K(K-1)} \sum_k \left(\hat{A} - \frac{1}{n} \sum_{j \in bin(k)} A_j \right)^2. \tag{C.12}$$

By denoting $K = N/2$ and $n = 2$, we have

$$(\hat{\sigma}_A^J)^2 = \frac{1}{(N/2-1)N/2} \sum_{k=1}^{N/2} (A_k^{(2)} - \hat{A})^2, \tag{C.13}$$

where $A_k^{(2)} = \frac{1}{2}(A_{2k-1} + A_{2k})$. Thus, the form is proven to be equivalent to Eq. (A.20).

References

[1] H. Flyvbjerg and H. G. Petersen: “Error estimates on averages of correlated data,” *J. Chem. Phys.* **91**, 461 (6 pages) (1989).

[2] B. A. Berg, “Markov Chain Monte Carlo Simulations and Their Statistical Analysis” (World Scientific, Singapore, 2004); http://www.worldscibooks.com/physics/5602.html .

Appendix D

Tips for Numerical Treatment for Summing up Large Numbers

The reweighting techniques often require one to deal with potentially very large numbers such as $\exp(f)$ and $n(E)$. Even though theoretically well-formulated, such calculations can be numerically halted because of overflows. One may have some trouble even with inputting them. We can usually avoid these numerical difficulties by using following algorithms. The trick is using logarithm.

The first algorithm is based on the following equality [1]. Supposing $A \geq B > 0$ for simplicity, we have

$$\log(A+B) = \log A + \log\left[1 + \frac{B}{A}\right], \tag{D.1}$$

$$= \log A + \log\left[1 + \exp(\log B - \log A)\right]. \tag{D.2}$$

Thus, $\log(A+B)$ can be numerically obtained without risk of overflows. Because $A \geq B$, $\exp(\log B - \log A)$ can only underflow. It happens only when $A \gg B$. In this case, we have $\log(A+B) \approx \log A$, so it is numerically safe. By recursively using this algorithm, one can obtain $\log(A_1 + A_2 + \cdots + A_n)$ only with $\log A_1, \log A_2, \ldots, \log A_n$. In the actual implementation, $\log A$ and $\log B$ should be substituted by $\max(\log A, \log B)$ and $\min(\log A, \log B)$.

Another algorithm is based on the following equality [2]. Supposing $A_1 \geq$

$A_2 \geq \cdots \geq A_n > 0$ for simplicity, we have

$$\log(A_1 + A_2 + \cdots + A_n) = \log A_1 + \log\left[1 + \frac{A_2}{A_1} + \frac{A_3}{A_1} + \cdots + \frac{A_n}{A_1}\right] \tag{D.3}$$

$$= \log A_1 + \log\left[1 + \exp(\log A_2 - \log A_1) + \cdots + \exp(\log A_n - \log A_1)\right]. \tag{D.4}$$

In this way, we can again calculate $\log(A_1 + A_2 + \cdots + A_n)$ from $\log A_1, \log A_2, \ldots, \log A_n$ with no overflows.

References

[1] B. A. Berg, “Markov Chain Monte Carlo Simulations and Their Statistical Analysis” (World Scientific, Singapore, 2004); http://www.worldscibooks.com/physics/5602.html .

[2] M. R. Shirts and J. D. Chodera: *The Journal of Chemical Physics* **129**, 124105 (10 pages) (2008).

Appendix E

Lattice Gas and Ising Model

The total energy of Ising model H on a square lattice can be converted into that of lattice gas in the following manner [1]:

$$H = -J \sum_{\langle i,j \rangle} \sigma_i \sigma_j - h \sum \sigma_i \tag{E.1}$$

$$= -J \sum_{\langle i,j \rangle} (2s_i - 1)(2s_j - 1) - h \sum (2s_i - 1)\,, \tag{E.2}$$

where $\sigma_i = \pm 1$ and $s_i = 1, 0$. If $\sigma_i = 1$, then $s_i = 1$ and vice versa. We then have

$$H = -4J \sum_{\langle i,j \rangle} s_i s_j + 2J \sum_{\langle i,j \rangle} \left(s_i + s_j \right) + J \sum_{\langle i,j \rangle} 1 - h \sum (2s_i - 1) \tag{E.3}$$

$$= -4J \sum_{\langle i,j \rangle} s_i s_j + 8Jn + 2JN - 2hn + hN \tag{E.4}$$

$$= -4J \sum_{\langle i,j \rangle} s_i s_j - (2h - 8J)n + (h - 2J)N\,, \tag{E.5}$$

where n and N are the number of occupied sites and the total number of sites, respectively. The first term corresponds to the attractive energy between particles of lattice gas. The second term corresponds to the chemical potential of lattice gas. The last term is a constant. Here, we define $\mu \equiv (2h - 8J)$ and $E_g \equiv -4J \sum_{\langle i,j \rangle} s_i s_j$.

Thus, free energy per spin f is given by

$$\exp(-\beta f N) = \sum_{\sigma_0=\pm1,\sigma_1=\pm1,\ldots,\sigma_N=\pm1} \exp(-\beta H) \tag{E.6}$$

$$= \sum_{s_0=1,0,s_1=1,0,\ldots,s_N=1,0} \exp[-\beta(E_g - \mu n)] \exp(-\beta(h - 2J)N) \tag{E.7}$$

$$= \Theta \exp(-\beta(h - 2J)N) \tag{E.8}$$

$$= \exp(\beta p N) \exp(-\beta(h - 2J)N)\,, \tag{E.9}$$

where p is pressure. Instead of V, N appears. The Greek letter Θ stands for the Grand partition function, where $\Theta = \sum_{s_0=1,0,s_1=1,0,\ldots,s_N=1,0} \exp[-\beta(E_g - \mu n)]$. The last two equations were obtained with grand canonical ensembles. Therefore, we obtain

$$-f = p - (h - 2J)\,, \tag{E.10}$$

$$p = h - f - 2J\,. \tag{E.11}$$

Thus, we conclude that the canonical ensemble of Ising model is equivalent to the μ-T ensemble of lattice gas model with the following correspondence:

$$p = h - f - 2J\,, \tag{E.12}$$

$$\mu = (2h - 8J)\,, \tag{E.13}$$

$$E_g = -4J \sum_{\langle i,j \rangle} s_i s_j. \tag{E.14}$$

References

[1] C. N. Yang: *Physical Review* **85**, 808–816 (1952).